Crystal growth of transition metal oxide thin films on two-dimensional layered hexagonal boron nitride and their device application

Shingo Genchi

MARCH 2023

Crystal growth of transition metal oxide thin films on two-dimensional layered hexagonal boron nitride and their device application

A dissertation submitted to

THE GRADUATE SCHOOL OF ENGINEERING SCIENCE

OSAKA UNIVERSITY

in partial fulfillment of the requirements for the degree of

DOCTOR OF PHILOSOPHY IN SCIENCE

By

Shingo Genchi

MARCH 2023

Abstract

Author: Shingo Genchi
Supervisor: Professor Hidekazu Tanaka

Transition metal oxide materials exhibiting metal–insulator or insulator–metal transition (MIT or IMT) accompanied with several orders of magnitude resistance changes have attracted attention for device application through growth of transition metal oxide thin films. Thus far, transition metal oxide thin films with good crystallinity showing MIT have been generally grown on single-crystal oxide substrates satisfying the structural lattice matching at the interface between substrates and thin films, such as Al_2O_3 and MgO. Therefore, the selection of the thin films and their growth substrates has been limited. For realizing the universal growth of transition metal oxide thin films, I focused on the use of two-dimensional layered hexagonal boron nitride (hBN) as a growth substrate since weak van der Waals interactions play a role in connecting each layer in hBN.

In this study, three kinds of transition metal oxide materials showing MIT with different lattice structures and lattice constants were selected as growth materials on hBN: VO_2 (vanadium dioxide), Fe_3O_4 (magnetite), and $NdNiO_3$ (neodymium nickelate). It was revealed that these thin films show clear MIT property accompanied with orders of magnitude resistance changes on hBN. The structural characterization also revealed that the growth of well-crystalized transition metal oxide thin films was realized on hBN, despite the expected existence of the lattice mismatch of 5 to 13%. These results suggest very weak lattice strain between the transition metal oxide films and hBN surface owing

to weak van der Waals interactions. I concluded that hBN could have a function of a universal growth substrate for various transition metal oxide thin films.

In addition, in particular for device application using VO_2 thin films, determination of the size of metallic domains, which govern the MIT property is essential. Temperature-dependent Raman spectroscopy and optical observation revealed that the metallic domain size of VO_2 thin films on hBN is ~500 nm, which is one order of magnitude larger than that of VO_2 thin films on Al_2O_3(0001), a common growth substrate of VO_2 thin films. Thus, it was found that VO_2/hBN microwires exhibit steep and step resistance changes reflecting the IMT in sub-micrometer individual metallic domains by changing temperature. This phenomenon originates from the confinement effect of the metallic domains even in micrometer scale.

Moreover, device application of VO_2 micro-structures on hBN was studied in electrical switching devices by application of bias voltage for inducing IMT of domains. The micro-structured VO_2/hBN exhibited step electric current increase by application of bias voltage owing to the formation of confined individual metallic domains, which was observed by simultaneous optical observation. These results open a way for domain engineering and contribute to creation of novel electrical switching devices, such as Mott transistors.

In this dissertation, the functionality of hBN as a universal growth substrate for various transition metal oxide thin films was discovered and the device application was demonstrated.

Contents

Chapter1

General Introduction

1.1 Transition metal oxide electronics

Transition metal oxide materials with strongly correlated electrons in spatially narrow 3d orbits exhibit unique physical properties. For instance, these materials exhibit metal–insulator transition (MIT) [1.1], colossal magnetic resistance [1.2, 1.3], ferroelectric [1.4, 1.5], high-temperature superconductivity [1.6, 1.7], and so forth unlike silicone (Si), which is a representative semiconducting electronic material in electronics today. Figure 1.1.1 shows some examples of transition metal oxides and the device application using transition metal oxide thin films.

VO_2 (vanadium dioxide) [1.8, 1.9], Fe_3O_4 (magnetite) [1.10], $NdNiO_3$ (neodymium nickelate) [1.11, 1.12] exhibit MIT. MIT in these materials have attracted much attention to be applicable to novel electronics since giant resistance, electric current, and magnetization change of several orders of magnitude can be induced from external stimuli. Thus, studies on creation of field effect transistors (Mott transistors) [1.13–1.16], electrical switching devices using Joule heating effect [1.17–1.19], smart windows [1.20, 1.21], magnetic switching devices [1.22, 1.23], memory devices [1.24] and so forth have been reported.

$La_{0.825}Sr_{0.175}MnO_3$ (LSMO) shows colossal magnetic resistance change and doping of Sr affects the magnetic status of LSMO [1.25, 1.26]. As Sr is doped, $La_{1-x}Sr_xMnO_3$ exhibits ferromagnetic property and it shows a temperature dependent resistance change, where the order of the resistance change is dependent on the magnetic field due to the difference in stabilization of the spin direction. These properties have been expected to be applicable to magnetic/electric devices and tunneling junctions [1.27, 1.28].

Perovskite-structured $SrTiO_3$ and $BaTiO_3$ show dielectric property and have been widely used in piezoelectric elements [1.29, 1.30] and multi-layer ceramic condensers [1.31].

Moreover, $YBa_2Cu_3O_7$ (YBCO) is a representative transition metal oxide material showing high-temperature superconductivity above 77 K. YBCO has been reported to be utilized in Josephson effect [1.32], superconducting electrode capacitor [1.33] and so forth. From the discovery of YBCO, much attention has been attracted to explore novel high-temperature superconductivity materials including cupper. Such unique physical property originates from strong Coulomb interactions among electrons. In other words, the control of the motion of electrons is the key to determine the material property in transition metal oxides. Based on these material properties, transition metal oxides have attracted much attention as “Beyond Si” materials to trigger electronics and spintronics in the next generation.

Recently, study on growth of transition metal oxide thin films, exploration of material properties for device application, and creation of electronics/spintronics devices using transition metal oxide thin films has been called “transition metal oxide electronics”.

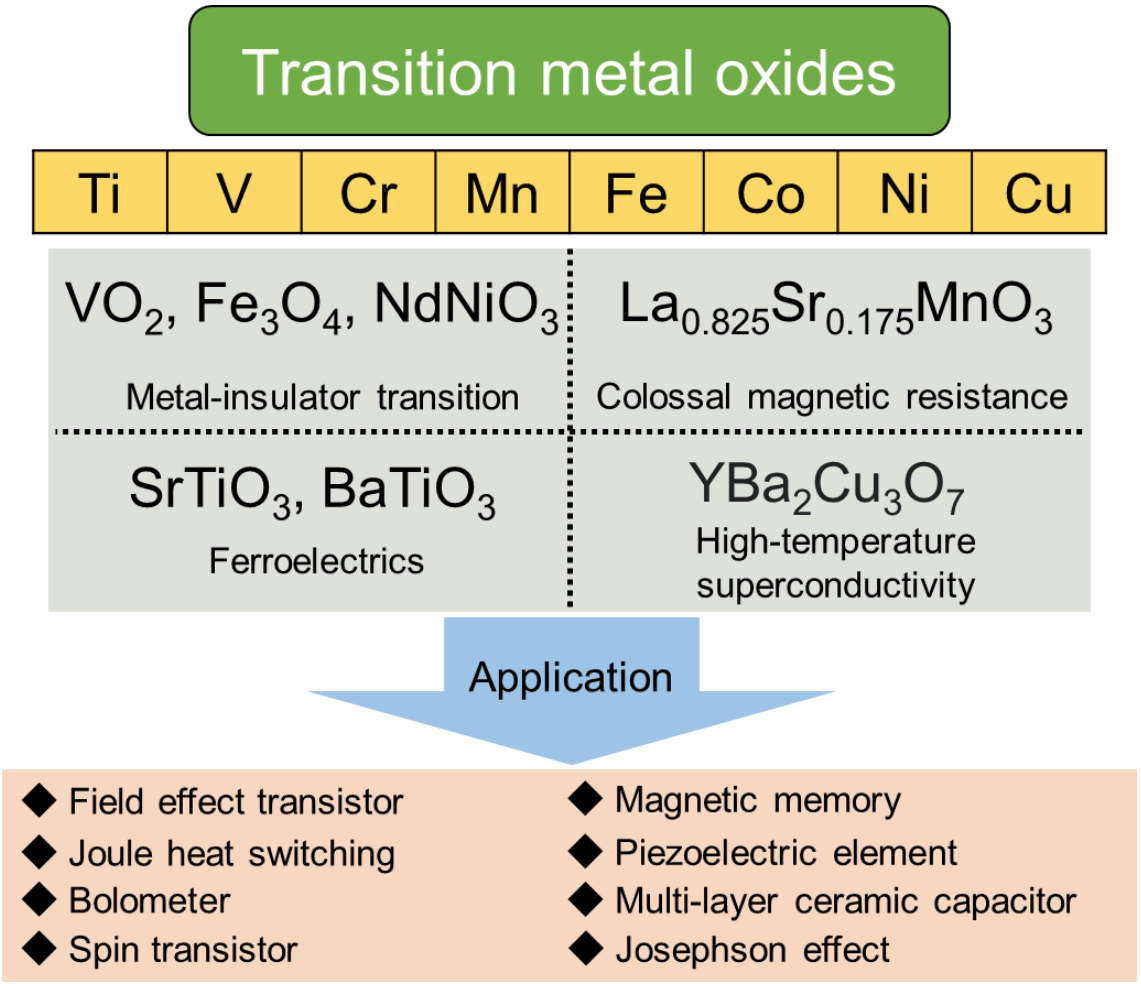

Figure 1.1.1 Transition metal oxide materials showing various properties and device application using transition metal oxide thin films.

1.2 Conventional growth of transition metal oxide thin films

For device application, establishment of the methods to grow high-quality thin films is essential. In addition to synthesis of single-crystal bulk transition metal oxides, various approach to grow thin films have been studied and established, such as sputtering deposition, pulsed laser deposition (PLD), molecular beam epitaxy, and so forth. With the progress in the synthesis of high-quality transition metal oxide thin films, novel material properties of transition metal oxide thin films and the device application have been explored. The high-quality well-crystalized transition metal oxide thin films exhibiting

MIT have been commonly grown on single-crystal oxide substrates, such as magnesium oxide (MgO) [1.34, 1.35], titanium dioxide (TiO_2) [1.36–1.38], sapphire (Al_2O_3) [1.38–1.40], $SrTiO_3$ [1.40, 1.41] and so force. Here takes an example of growth of VO_2 thin films for simple explanation. For obtaining high-quality thin films showing prominent MIT property, interfacial lattice mismatching should be reduced. In other words, it is required that thin films and substrates have closer atomic arrangement and lattice constants to each other. The interfacial matching of lattice structures and lattice constants plays a significant role in the MIT property. For instance, single-crystal epitaxial VO_2 thin films can be grown on TiO_2 substrates since VO_2 and TiO_2 have same rutile lattice structure [1.42]. Accompanied with the interfacial lattice matching, VO_2(001) thin films on TiO_2(001) substrates show steep resistance change, as shown in Fig. 1.2.1(a).

On the other hand, VO_2 thin films on Al_2O_3(0001) substrates are in-plane preferentially oriented polycrystalline since the lattice structures and lattice constants are considerably different [1.39]. Thus, gradual resistance changes are observed because of the bad crystallinity of VO_2 thin films, as shown in Fig. 1.2.1(b).

With these backgrounds, we can conclude that the restriction of the interfacial lattice matching hinders various growth of transition metal oxide thin films. Considering that transition metal oxide materials have a variety of lattice structures and lattice constants, the matching of substrates and thin films is limited. Thus, a universal substrate to grow various transition oxide thin films regardless of lattice structures and lattice constants is required. With the negligible effect of the interfacial lattice mismatching, a universal growth substrate can largely contribute to the novel synthesis of transition oxide materials.

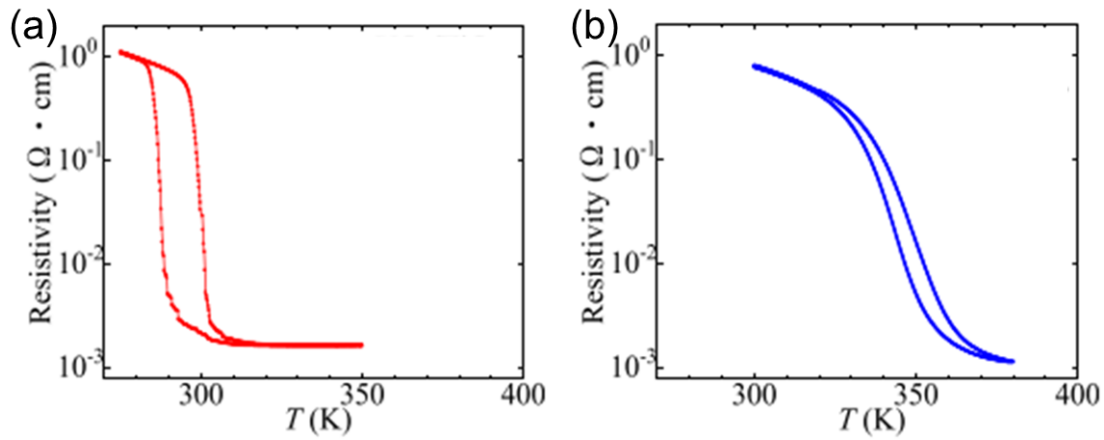

Fig. 1.2.1 (a) *R*–*T* curves of VO_2 thin films on TiO_2(001) substrates. (b) *R*–*T* curves of VO_2 thin films on Al_2O_3(0001) substrates [1.37].

1.3 Hexagonal boron nitride: a new growth substrate

As a candidate material of a universal growth substrate, I have focused on two-dimensional layered materials, where each layer is connected by van der Waals interaction [1.43]. These two-dimensional layered materials also exhibit attractive material properties, such as semimetal (graphene) [1.44, 1.45] and direct bandgap semiconductor (transition metal dichalcogenides: TMDC) [1.46], and so forth. Besides, two-dimensional layered materials have a possibility to reduce the lattice mismatch owing to weak van der Waals interactions. Therefore, I assumed that it is attractive to apply these materials to growth substrates of transition metal oxide thin films.

Among these two-dimensional layered materials, I particularly focused on the use of hexagonal boron nitride (hBN). Figure 1.3.1 shows the honeycomb lattice structure and the lattice constants of hBN. Each layer of hBN is connected by weak van der Waals interactions. Importantly, hBN keeps insulating property even thinned down to several nm thicknesses [1.47, 1.48] with the bandgap energy of ~ 6 eV [1.49, 1.50] and chemical stability when exposed to oxygen atmosphere at 723 K for hours [1.51, 1.52]. Taking into

account that generally transition metal oxide thin films are grown in an oxygen ambient and at a high temperature up to ~1000 K, hBN is expected to be a suitable material as a substrate to grow various transition oxide thin films. Moreover, the stacks of thin film/hBN may have a transferability onto arbitrary materials using a transfer technique [1.53]. In this study, single-crystal hBN synthesized under high pressure was utilized [1.54].

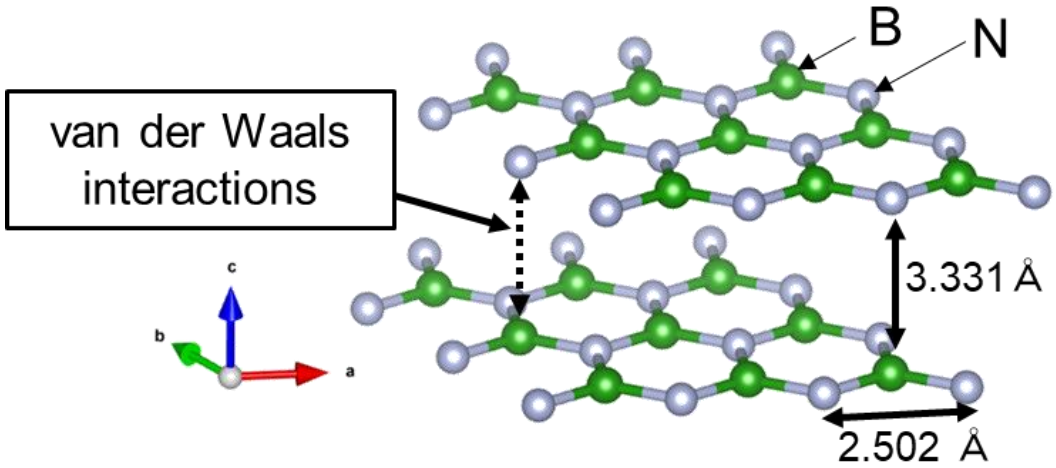

Fig. 1.3.1 Lattice structure and lattice constants of hBN. Green and gray circles indicate boron and nitride atoms, respectively. The black dotted arrow indicates van der Waals interactions.

Figures 1.3.2(a) and (b) show the schematic of the growth of transition metal oxide thin films on single-crystal oxide substrates and hBN, respectively. Conventionally, transition metal oxide thin films have been grown on single-crystal oxide thin films. Because of the strong ionic/covalent interactions at the interface, the lattice mismatch between a film and a substrate leads to the lattice strain effect. If the lattice strain is significant owing to the large lattice mismatch at the interface, degradation of crystallinity, i.e., formation of defects causes the poor MIT properties of the thin films. On the other hand, if the interface interaction between the thin film and the hBN is negligibly small

due to weak van der Waals interactions, various transition metal oxide thin films would be grown on hBN despite the existence of the lattice mismatch. Namely, the growth of transition metal oxide thin films could be promoted with a high degree of freedom beyond the restriction on the matching of the lattice structures and lattice constants of substrates and thin films.

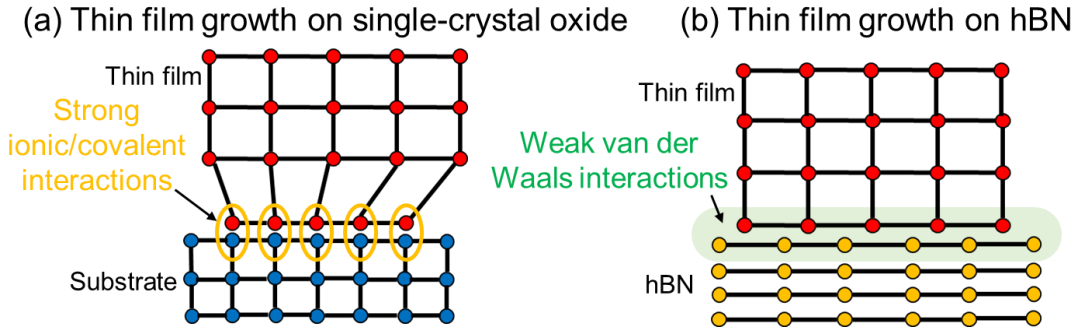

Figure 1.3.2 (a) Schematic of thin film growth on single-crystal oxide substrates. The yellow ovals indicate the interfacial connection with strong ionic and/or covalent interactions. (b) Schematic of thin film growth on hBN. The green region indicates the interfacial connection with weak van der interactions.

1.4 Scope of this study

In this dissertation, growth of VO_2 thin films on hBN was attempted as an example of high-quality thin films beyond the lattice mismatch between VO_2 and hBN. In addition, the applicability of hBN as a universal platform for growing various transition oxide materials was studied through the growth of Fe_3O_4 and $NdNiO_3$ with spinel and Perovskite structures, respectively. Through these studies, the universality of hBN as a growth substrate was demonstrated as shown in Fig. 1.4.1. Finally, as an aspect of device application, I demonstrated the functionality of VO_2 film grown on hBN with step electrical switching property.

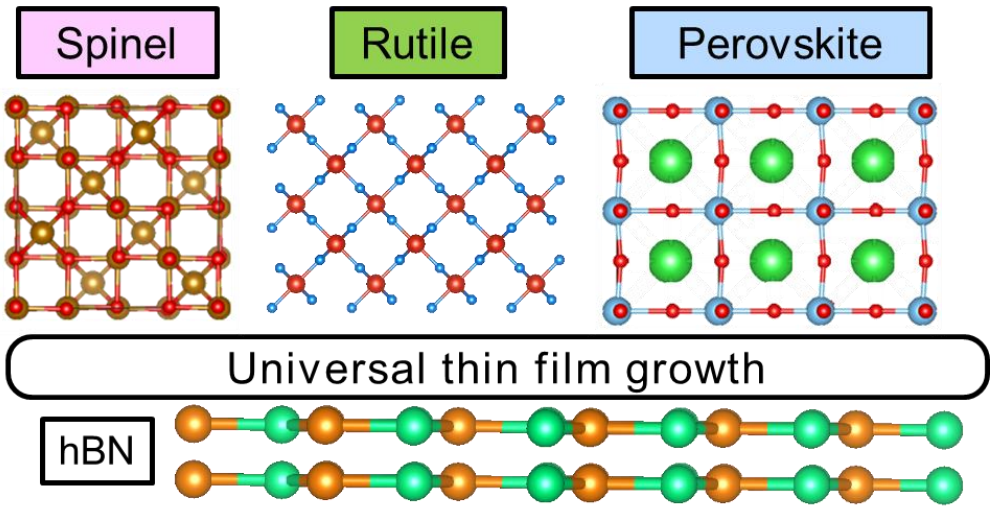

Figure 1.4.1 Schematic of universal growth of transition metal oxide thin films on hBN.

This thesis is divided into 7 chapters and Appendix. In Chapter1, the general introduction on the growth of transition metal oxide thin films and oxide electronics and the aim of this study were presented. In Chapter 2, experimental and analysis details of this study are indicated, such as pulsed laser deposition, photolithography, and so forth.

In Chapter 3, the growth of VO_2 thin films on hBN was attempted. The crystal structure and the MIT property of VO_2 thin films on hBN were characterized using Raman spectroscopy, atomic force microscopy, scanning transmittance electron microscopy, and electrical transport measurements. With the perspective of device application, transfer of VO_2/hBN stacks was demonstrated.

In Chapter 4, metallic domains, which determine the MIT property, were identified and their size was analyzed using Raman spectroscopy and an optical microscopy. Next, the device-size-dependent MIT property was measured for obtaining multi-level step-like resistance changes owing to the confined metallic domains.

In Chapter 5, in the perspective of application in electrical switching devices using Joule heating effect, electrical switching property was measured by fabrication of a micro-

structured VO_2/hBN sample with the size determined in Chapter 4 to obtain multi-level step-like resistance changes. The optical microscopy images reflecting the emergence of the metallic domains were obtained simultaneously using an optical microscopy during the electric current measurement, which revealed that individual metallic domains contribute to the step electrical switching property.

In Chapter 6, with the perspective of application in hBN as a universal growth substrate, growth of Fe_3O_4 and $NdNiO_3$ thin films with different lattice structures and lattice constants from those of VO_2 was attempted on hBN. With the MIT and structural characterization of these thin films, the applicability of hBN as a universal growth substrate was studied. Additionally, interpretation on the growth of transition metal oxide thin films on hBN was proposed from the experimental results.

In Chapter 7, general conclusion and future perspective are summarized. In Appendix, bubble-free transfer method, a new method to transfer thin film/hBN stacks with high efficiency in number and high alignment accuracy, was demonstrated. In addition, recently, high-quality hBN sheets have been successfully synthesized using chemical vapor deposition (CVD) in a large size. Using the CVD-hBN sheets, growth of VO_2 thin films on CVD-hBN sheets was attempted and the crystal structure was characterized through out-of-plane X-ray diffraction in addition to the measurement of the MIT property of VO_2/CVD-hBN.

1.5 References

[1.1] M. Imada, A. Fujimori, and Y. Tokura, Rev. Mod. Phys., **70**, 1039 (1998).

[1.2] Y. Tokura, Y. Tomioka, H. Kuwahara, A. Asamitsu, Y. Moritomo, and M. Kasai, J. Appl. Phys., **79**, 5288 (1996).

[1.3] Y. Moritomo, A. Asamitsu, H. Kuwahara, and Y. Tokura, Nature, **380**, 141 (1996).

[1.4] J. Moreau, C. Michel, R. Gerson, and W. James, J. Phys. Chem. Solids, **32**, 1315 (1971).

[1.5] M. N. Kamalasanan, N. Deepak Kumar, and S. Chandra, J. Appl. Phys., **74**, 5679–5686 (1993).

[1.6] J. G. Bednorz and K. A. Müller, Z. Phys. B, **64**, 189 (1986).

[1.7] C.-J. Kim and G.-W. Hong, Supercond. Sci. Technol., **12**, R27 (1999).

[1.8] F. J. Morin, Phys. Rev. Lett., **3**, 34 (1959).

[1.9] C. N. Berglund and H. J. Guggenheim, Phys. Rev., **185**, 1022 (1969).

[1.10] E. J. W. Verwey Nature, **144**, 327 (1939).

[1.11] X. Granados, J. Fontcuberta, X. Obradors, L. Mãnosa, and J. B. Torrance, Phys. Rev. B, **48**, 11666 (1993).

[1.12] G. Catalan, R. M. Bowman, and J. M. Gregg, Phys. Rev. B, **62**, 7892 (2000).

[1.13] Y. Zhou and S. Ramanathan, J. Appl. Phys., **111**, 084508 (2012).

[1.14] S. Sengupta, K. Wang, K. Liu, A. K. Bhat, S. Dhara, J. Wu, and M. M. Deshmukh, Appl. Phys. Lett., **99**, 062114 (2011).

[1.15] T. Wei, T. Kanki, M. Chikanari, T. Uemura, T. Sekitani, and H. Tanaka, Sci. Rep., **7**, 17215 (2017).

[1.16] T. Yajima, T. Nishimura, and A. Toriumi, Nat. Commun., **6**, 10104 (2015).

[1.17] D. Li, A. A. Sharma, D. K. Gala, N. Shukla, H. Paik, S. Datta, D. G. Schlom, J. A.

Bain, and M. Skowronski, ACS Appl. Mater. Interfaces, **8**, 12908 (2016).

[1.18] B. S. Mun, J. Yoon, K. S. Mo, K. Chen, N. Tamura, C. Dejoie, M. Kunz, Z. Liu, C. Park, K. Moon, and H. Ju, Appl. Phys. Lett., **103**, 061902 (2013).

[1.19] O. Murtagh, B. Walls, and I. V. Shvets, Appl. Phys. Lett., **117**, 063501 (2020).

[1.20] Z. Huang, S. Chen, C. Lv, Y. Huang, and J. Lai, Appl. Phys. Lett., **101**, 191905 (2012).

[1.21] J. Zhou, Y. Gao, Z. Zhang, H. Luo, C. Cao, Z. Chen, L. Dai, and X. Liu, Sci. Rep., **3**, 3029 (2013).

[1.22] T. Tsuchiya, K. Terabe, M. Ochi, T. Higuchi, M. Osada, Y. Yamashita, S. Ueda, and M. Aono, ACS Nano, **10**, 1655 (2016).

[1.23] M. S. Ansari, M. H. D. Othman, M. O. Ansari, S. Ansari, and H. Abdullah, Ceram. Int., **46**, 19302 (2020).

[1.24] C. Oh, S. Heo, H. M. Jang, and J. Son, Appl. Phys. Lett., **108**, 122106 (2016).

[1.25] Y. Tokura, A. Urushibara, Y. Moritomo, T. Arima, A. Asamitsu, G. Kido, and N. Furukawa, J. Phys. Soc. Jpn., **63**, 3931 (1994).

[1.26] A. Urushibara, Y. Moritomo, T. Arima, A. Asamitsu, G. Kido, and Y. Tokura, Phys. Rev. B, **51**, 14103 (1995).

[1.27] M. Cesaria, A. P. Caricato, G. Maruccio, and M. Martino, J. Phys. Conf. Ser. **292**, 012003 (2011).

[1.28] Z. Wen and D. Wu, Adv. Mater., **32**, 1904123 (2019).

[1.29] J. H. Haeni, P. Irvin, W. Chang, R. Uecker, P. Reiche, Y. L. Li, S. Choudhury, W. Tian, M. E. Hawley, B. Craigo, A. K. Tagantsev, X. Q. Pan, S. K. Streiffer, L. Q. Chen, S. W. Kirchoefer, J. Levy, and D. G. Schlom, Nature, **430**, 758 (2004).

[1.30] K. J. Choi, M. Biegalski, Y. L. Li, A. Sharan, J. Schubert, R. Uecker, P. Reiche, Y.

B. Chen, X. Q. Pan, V. Gopalan, L. Q. Chen, D. G. Schlom, C. B. Eom, Science, **306**, 1005 (2004).

[1.31] S.-H. Yoon, J.-S. Park, S.-H. Kim, and D.-Y. Kim, Appl. Phys. Lett., **103**, 042901 (2013).

[1.32] S.-J. Kim, Yu. I. Latyshev, and T. Yamashita, Supercond. Sci. Technol., **12**, 729 (1999).

[1.33] Y. He, Y. Wang, Y. Hu, W. Chen, and Z. Yan, Supercond. Sci. Technol., **32**, 015010 (2019).

[1.34] F. J. Wong, Y. Zhou, and S. Ramanathan, J. Cryst. Growth, **364**, 74 (2013).

[1.35] X. W. Li, A. Gupta, G. Xiao, and G. Q. Gong, J. Appl. Phys., **83**, 7049 (1998).

[1.36] Y. Muraoka, K. Saeki, R. Eguchi, T. Wakita, M. Hirai, T. Yokoya, and S. Shin, J. Appl. Phys., **109**, 043702 (2011).

[1.37] M. Chikanari, T. Kanki, T. Wei, and H. Tanaka, Appl. Phys. Lett., **113**, 053102 (2018).

[1.38] Y. Cui and S. Ramanathan, J. Vac. Sci. Technol., A **29**, 041502 (2011).

[1.39] J. Sang, T. Zheng, L. Xu, X. Zhou, S. Tian, J. Sun, X. Xu, J. Wang, S. Zhao, and Y. Liu, J. Alloys Compd., **876**, 160208 (2021).

[1.40] S. Tiwari, R. Prakash, R. J. Choudhary, and D. M. Phase, J. Phys. D: Appl. Phys., **40**, 4943 (2007).

[1.41] A. Srivastava, H. Rotella, S. Saha, B. Pal, G. Kalon, S. Mathew, M. Motapothula, M. Dykas, P. Yang, E. Okunishi, D. D. Sarma, and T. Venkatesan, APL Mater., **3**, 026101 (2015).

[1.42] H. Qiu, M. Yang, Y. Dong, H. Xu, B. Hong, Y. Gu, Y. Yang, C. Zou, Z. Luo, and C. Gao, New J. Phys., **17**, 113016 (2015).

[1.43] M.-Y. Li, C.-H. Chen, Y. Shi, and L.-J. Li, Mater. Today, **19**, 322 (2016).

[1.44] A. K. Geim and K. S. Novoselov, Nat. Mater., **6**, 183 (2007).

[1.45] E. P. Randviir, D. A. Brownson, and C. E. Banks, Mater. Today **17**, 426 (2014).

[1.46] M. Chhowalla, H. S. Shin, G. Eda, L.-J. Li, K. P. Loh, and H. Zhang, Nat. Chem., **5**, 263 (2013).

[1.47] L. Britnell, R. V. Gorbachev, R. Jalil, B. D. Belle, F. Schedin, M. I. Katsnelson, L. Eaves, S. V. Morozov, A. S. Mayorov, N. M. R. Peres, A. H. C. Neto, J. Leist, A. K. Geim, L. A. Ponomarenko, and K. S. Novoselov, Nano Lett., **12**, 1707 (2012).

[1.48] G. -H. Lee, Y. J. Yu, C. Lee, C. Dean, K. L. Shepard, P. Kim, and J. Hone, Appl. Phys. Lett., **99**, 243114 (2011).

[1.49] K. Watanabe, T. Taniguchi, and H. Kanda, Nat. Mater., **3**, 404 (2004).

[1.50] G. Cassabois, P. Valvin, and B. Gil, Nat. Photonics, **10**, 262 (2016).

[1.51] A. G. F. Garcia, M. Neumann, F. Amet, J. R. Williams, K. Watanabe, T. Taniguchi, and D. Goldhaber-Gordon, Nano Lett., **12**, 4449 (2012).

[1.52] L. H. Li, J. Cervenka, K. Watanabe, T. Taniguchi, and Y. Chen, ACS Nano, **8**, 1457 (2014).

[1.53] P. Zomer, M. Guimarães, J. Brant, N. Tombros, and B. Van Wees, Appl. Phys. Lett., **105**, 013101 (2014).

[1.54] T. Taniguchi and K. Watanabe, J. Cryst. Growth, **303**, 525 (2007).

Chapter 2

Experimental

2.1 Sample preparation

2.1.1 Pulsed laser deposition (PLD)

Fig. 2.1.1(a) shows the overall image of the pulsed laser deposition (PLD) system. Fig. 2.1.1(b) shows the cross-sectional schematic. PLD is a kind of physical vacuum deposition method and has been often used to grow oxide thin films with atomically controlled flat surfaces. The pulsed laser beam is focused on the target surface and laser ablation is locally induced in the vacuum chamber. The ablated atoms fly toward substrates and thin films are formed on the substrates through the crystallization. The ablated atoms form plasma called “plume”. This process is conducted under a high vacuum condition or the presence of a background gas such as oxygen. In addition, the temperature of substrates and the laser frequency should also be optimized for obtaining well-crystallized the thin films.

For keeping a high vacuum condition, a rotary pump and a turbo molecular pump are equipped in the PLD system. The base pressure of a PLD chamber is generally maintained to be 10^{-5}~10^{-4} Pa. In my study, an ArF excimer laser was utilized (λ = 193 nm). In my experiment, three types of the transition metal oxides were selected as a growth material: VO_2, Fe_3O_4, and $NdNiO_3$. These thin films were grown under the optimized growth condition.

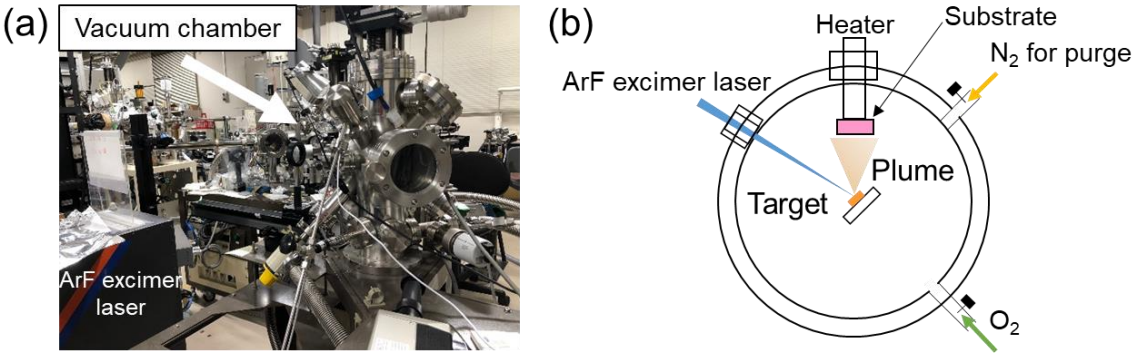

Figure 2.1.1 (a) Overall image of PLD system. (b) Schematic of PLD system.

2.1.2 Raman spectroscopy

Raman spectroscopy is one of the vibrational spectroscopic techniques, which can be used to obtain information on molecular vibrations and structure of a sample. This technique is performed by laser irradiation to a sample to generate the Raman scattering process. The Raman scattered light is detected with a CCD camera. The characteristic peaks in Raman Spectrum make it possible to identify substances including polymorphs and evaluate local crystallinity, stress profile and so forth in the sample. Fig. 2.1.2 shows the schematic mechanism of Raman scattering. When the light is scattered by matter, the process is mostly elastic (so called Rayleigh scattering) and there is no change in energy. However, sometimes the scattering involves an inelastic process and the scattered light has a different energy from that of the incident light. This inelastic scattering process is called Raman scattering or Raman effect. The Raman scattering can be classified in two types: Stokes Raman Scattering and Anti-Stokes Raman Scattering [2.1, 2.2]. The Stokes Raman scattering is a process in which an electron is excited from the ground state level to a virtual level by light and then, returns to a vibrational level. This process involves energy absorption by matter, and thus, the scattered light has lower energy (longer wavelength) than the incident light. In contrast, the Anti-Stokes Raman scattering is a process in which an electron is excited from a vibrational level to a virtual level and then falls to the ground level. This process involves an energy transfer from matter to a phonon. Thus, the scattered light has larger energy than that of the incident light.

In my experiment, a commercial solid-state laser Raman spectroscopy (Raman Touch, Nanophoton) was utilized to confirm the formation of the thin films on hBN. For VO_2 and Fe_3O_4 thin films, temperature-dependent Raman spectroscopy was conducted additionally to characterize the Raman shift owing to the structural lattice change due to

MIT. Figure 2.1.3 shows the overview of the experimental system. The temperature was controlled using a Peltier sample stage with liquid N_2 from 300 to 380 K for VO_2 thin films and 90 to 140 K for Fe_3O_4 thin films, respectively. Raman spectroscopy measurement for VO_2/hBN stacks after the transfer process was partly supported by Dr. Mahito Yamamoto (currently Associate Professor of Kansai University).

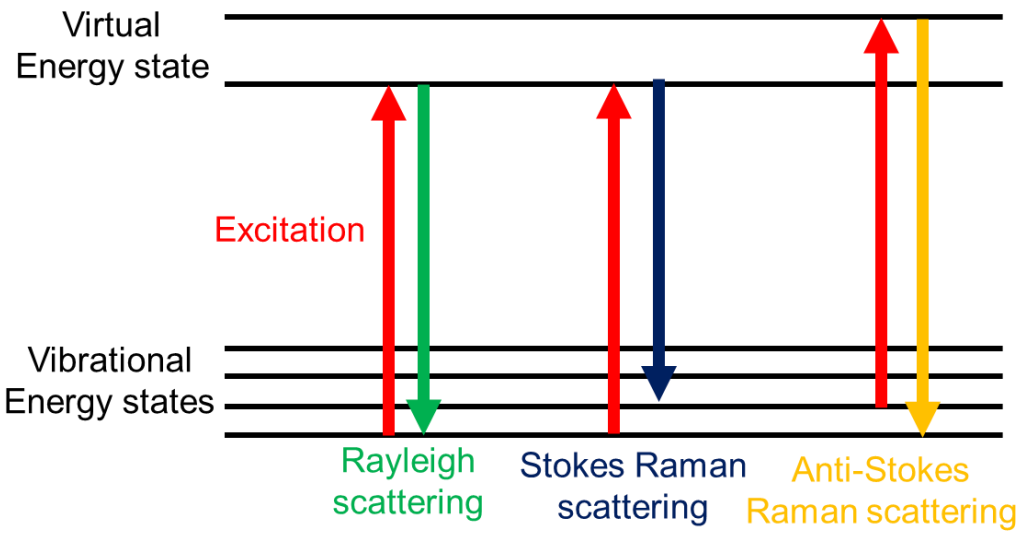

Figure 2.1.2 Schematic mechanism of Rayleigh scattering, Stokes Raman scattering and Anti-Stokes Raman scattering.

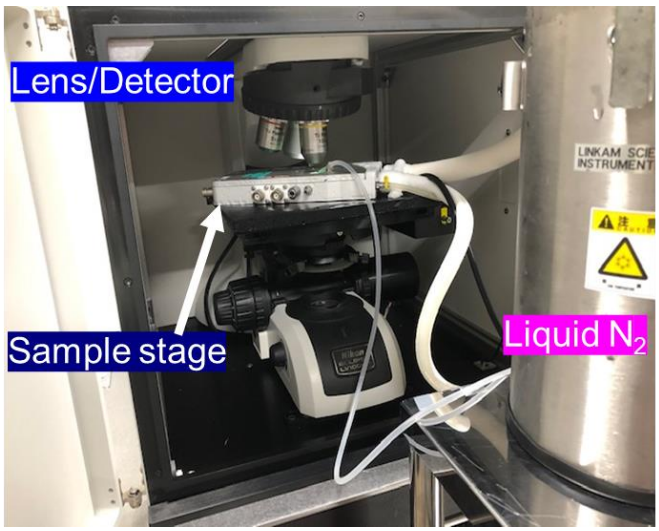

Figure 2.1.3 Overall view of the experimental system during temperature-dependent Raman spectroscopy measurement.

2.1.3 Atomic force microscopy

Atomic force microscope (AFM) is a tool to characterize the structure and surface morphology by using atomic force. Figure 2.1.4 shows the schematic of AFM. A small needle on a cantilever is scanned around a surface while feedback is applied to maintain the atomic force between the surface and the small needle. Laser light strikes the back of the cantilever and the position of the laser spot is adjusted so that the spot is in the center of the photodiode. Generally, atomic force consists of repulsive force and attractive force, which are proportional to -6^{th} and -12^{th} power of distance, respectively [2.3-2.5]. Thus, there exists an energetically stable point where repulsive and attractive force are equal. When the distance between the surface and the needle changes, feedback is applied to maintain the position of the laser spot of the reflected light. The *z* position change corresponds to the surface morphology and makes it possible to conduct mapping of the surface structure and morphology. This is called contact mode.

Another mode exists to characterize the surface morphology: tapping mode. The cantilever is oscillated at resonance frequency, making the amplitude maximum. When the distance between the cantilever and the surface changes, the amplitude and the frequency of the vibration also changes. As with contact mode, the mapping can be conducted while feedback is applied to a piezo device to maintain the amplitude and frequency of the vibration. The advantage of tapping mode is that the sample may not be damaged since the cantilever doesn't touch the surface of the sample. Nowadays, it is the mainstream to use tapping mode in AFM measurements.

In my research, the AFM measurement was conducted using AFM 5000/5300E (Hitachi High-Tech Corp.) at room temperature in an air ambient with Si cantilevers (SPA-300HV, Hitachi High-Tech Science).

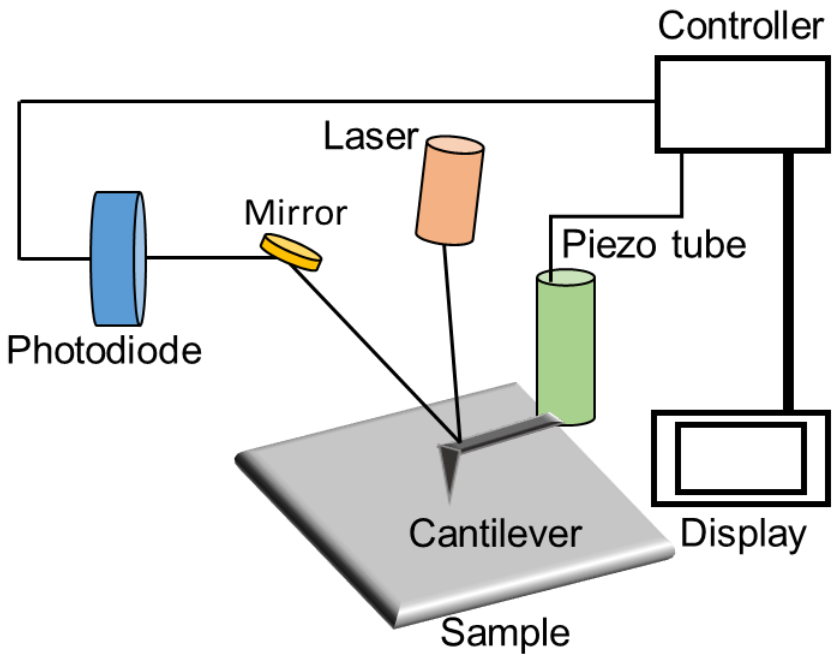

Figure 2.1.4 Schematic of AFM system.

2.1.4 Scanning transmittance electron microscopy

Scanning transmittance electron microscope (STEM) is utilized to obtain crystal lattice images with atomically-ordered high resolution. Figure 2.1.5 shows the schematic of STEM. The electrons irradiated to the sample magnifies the interference image when the electrons penetrate the sample, forming atomically resolved images. The electrons are scattered at higher angle as the atomic number of the element (Z) at the beam spot is larger [2.6]. Due to this characteristic, an image contrast, which is proportional to 2^{nd} power of Z, can be obtained by using loop-shaped detectors. This method is called HAADF (High-Angle Annular Dark Field) method. Bright field (BF) detectors and Electron Energy Loss Spectroscopy (EELS) detectors are equipped below the sample to obtain the phase contrast and the information on electronic structures, respectively. By the analysis of cross-sectional image of thin films by STEM, lattice defects like dislocation can be characterized in the atomic scale. STEM is nowadays an essential tool to obtain precise

information on the crystal structure and growth dynamics.

In my experiment, STEM was used to obtain the cross-sectional image of the interface between thin films and hBN. The STEM measurement for VO_2/hBN samples was conducted in Prof. Yasukazu Murakami group at Kyushu University, Fukuoka, Japan.

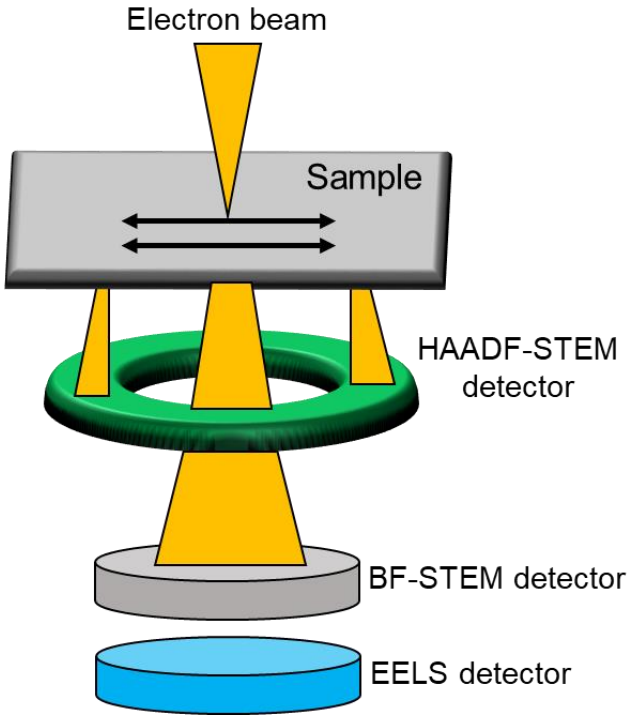

Figure 2.1.5 Schematic of STEM system composed of HAADF-STEM detector, BF-STEM detector, and EELS detector.

2.1.5 Photolithography

Photolithography is a good precision process of making patterns with light-sensitive photoresist covering on the sample surface. Figure 2.1.6 shows the schematic of the photolithography process. Arbitrary patterns can be designed through a drawing software, such as Vectorworks. The resolution limit is around 1–2 μm. In my experiment, a positive photoresist (AZ5206E, Merck) was spin-coated on the substrate in a proper sequence using a spin coater to spin-coat the photoresist homogeneously on the sample. Next, the sample was placed on a hot plate at 368 K for 3 minutes. Then, the sample was placed on

the lithography stage. The photoresist was exposed to ultraviolet (UV) light (λ = 365 nm) to change the characteristic of the photoresist to melt in developer. The sample was put into the developer after the exposure and rinsed with pure water to remove the developer. Through these processes, photoresist patterns were obtained.

In my experiment, photolithography was used for electrode deposition and etching to form microwires.

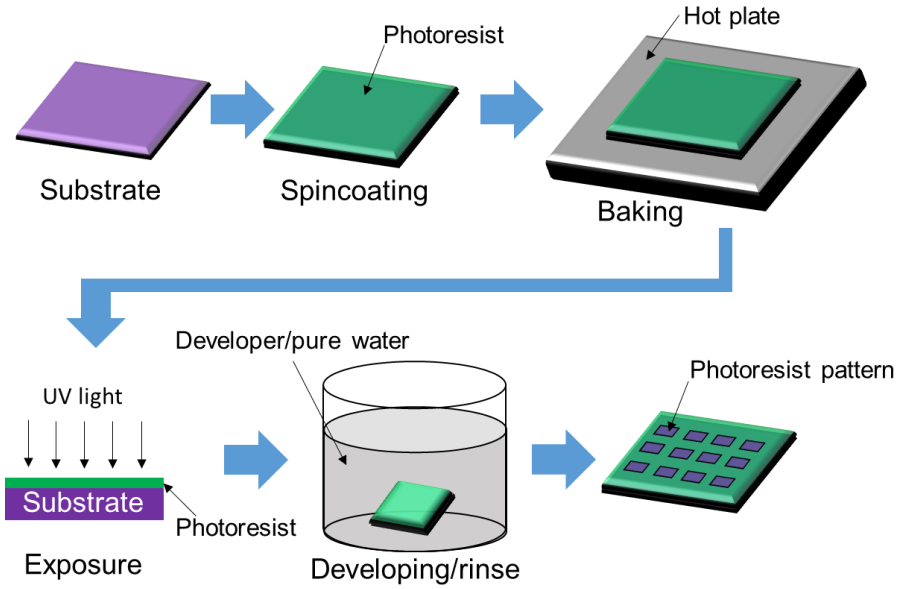

Figure 2.1.6 Schematic of photolithography process.

2.1.6 Radio frequency sputtering deposition

When certain atoms or ions with high energy of several hundreds of electron volt strike surfaces of solid target materials, some atoms are released from the surface of the target material, which causes momentum exchange. This phenomenon is called spattering. In general, sputtering deposition is utilized in an ambient of reactive ion gases, such as Ar and O_2. The reactive gases are ionized by applying bias voltage. The separated electrons and atoms play a role in the deposition system. Suppose direct bias is applied to the system and the electrons move to the target area. The negatively charged region in the

target material attracts positive ions and the momentum exchange occurs accompanied by strike of the ions. The target materials must be conductive using the direct current (DC) sputtering deposition. In contrast, the radio frequency (RF) sputtering has an advantage that even insulating materials can be utilized as target materials. Figure 2.1.7 shows the schematic of RT sputtering deposition system. When alternation voltage is applied to the sputtering system, the electrons can move faster than the charged atoms. This causes negative self-bias to the voltage status of plasma. Consequently, the target has a negative DC bias and can attract ions and cause momentum exchange accompanied with strike of the atoms. Since large-scaled thin films can be obtained using sputtering deposition, RF sputtering has been widely used for deposition of thin films, such as metals, oxides, and insulating materials today.

In my experiment, RF sputtering was utilized at room temperature for deposition of Pt and Cr electrodes for electric transport measurements at the partial Ar pressure of 1.0 Pa.

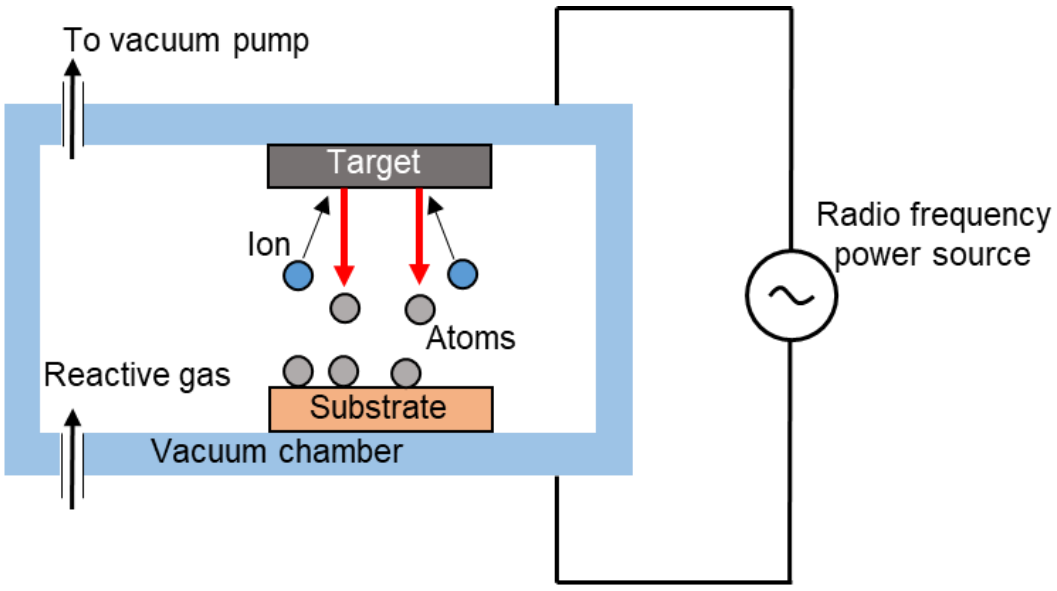

Figure 2.1.7 Schematic of RF sputtering deposition system.

2.2 Measurement

2.2.1 Electric transport measurement system

Fig. 2.2.1(a) shows the schematic of two-terminal measurement system for electric transport property of VO_2 thin films showing MIT slightly above room temperature. In this measurement system, source measure unit (2634A, Keithley) and variable-temperature-controlled stage with Peltier element (T95, Linkam) were used as a power source and a sample stage, respectively.

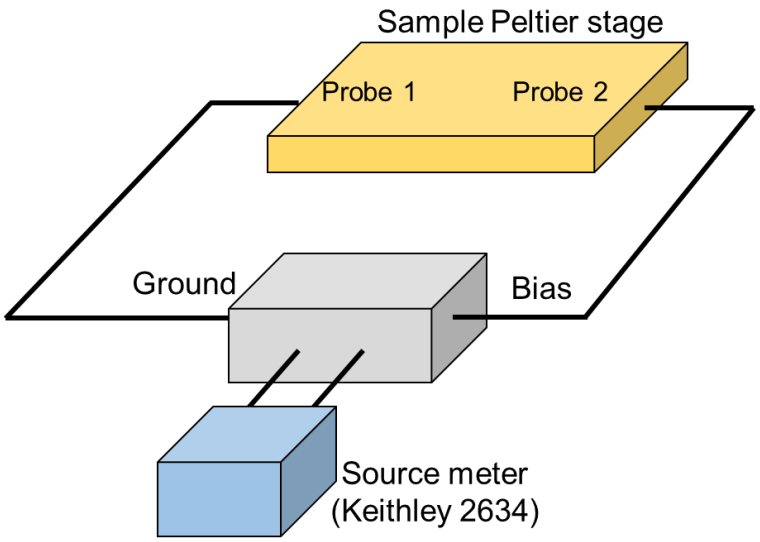

Fig. 2.2.1 Schematic of two-terminal electric transport measurement system

For *in situ* observation of the emergence of metallic domains in VO_2 thin films on hBN during MIT and simultaneous electric transport property (*I*–*V* characteristics) measurements, a measurement system was constructed with a movie camera, a source measurement unit (SMU: B2901A, Keysight), and an optical microscope (BX51M, Olympus). The measurement program was Easy Expert, Keysight. Figure 2.2.2(a) shows the overview of the experimental system. Figure 2.2.2(b) shows the magnified image of the sample stage. The measurement sample was placed on the sample stage in the optical microscope and the real-time observation was available. Note that the sample stage in the

optical microscope was able to heat the sample up to 423 K. Using the temperature-controllable sample stage, the emergence of the metallic domain was confirmed in addition to the *in situ* electrical switching measurement. Figure 2.2.2(c) shows the schematic of the measurement system. For this measurement, a VO_2/hBN sample was placed on a slide glass and electrically connected to SMU with BNC cables, Ag paste, and epoxy paste. This measurement was conducted in cooperation with Dr. Shu Nakaharai (Principal Researcher) of National Institute for Materials Science, Tsukuba, Japan.

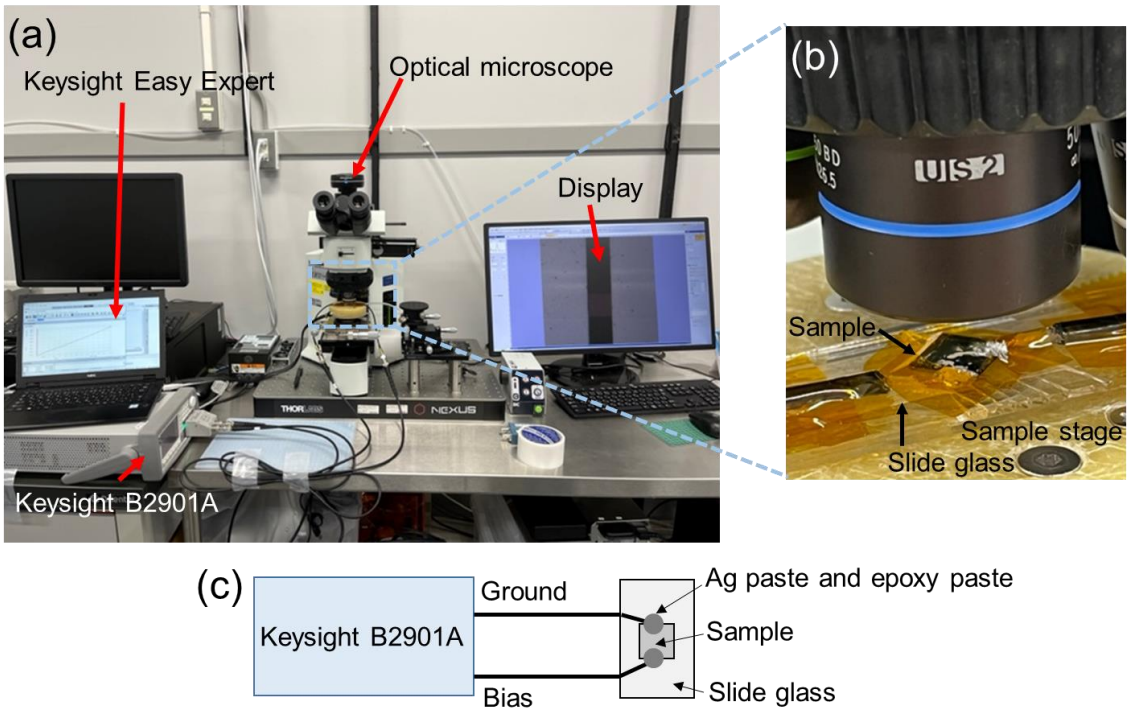

Fig. 2.2.2 (a) Overview of the measurement system for electrical switching and observation of the domain dynamics. (b) Magnified image of the variable-temperature sample stage, sample, and objective lens. (c) Schematic of the circuit of the measurement system.

2.2.2 Physical Property Measurement System (PPMS)

PPMS is the name of a commercial material property measurement system invented by Quantum Design, Inc. Using this system, various material properties, such as temperature-dependent and/or magnetic dependent resistance/current change can be investigated under a vacuum condition. The measurement temperature range is 4 to 400 K since liquid He is utilized in this measurement system. The magnetic field can be applied up to ~7 T at maximum.

Figure 2.2.3(a) shows a Fe_3O_4 sample placed on the sample stage for PPMS. Figure 2.2.3(b) shows the schematic of the PPMS system. In PPMS, magnets are equipped beside the sealed sample space for magnetic measurements. With the sample holder transferred to the bottom of the sealed sample space, temperature-dependent material properties can be measured. Since the measurement probe is sealed strictly, the material properties can be measured with high stability in temperature. In my experiment, PPMS is suitable for investigation of the MIT properties of Fe_3O_4 and $NdNiO_3$ thin films on hBN under low-temperature measurement regions.

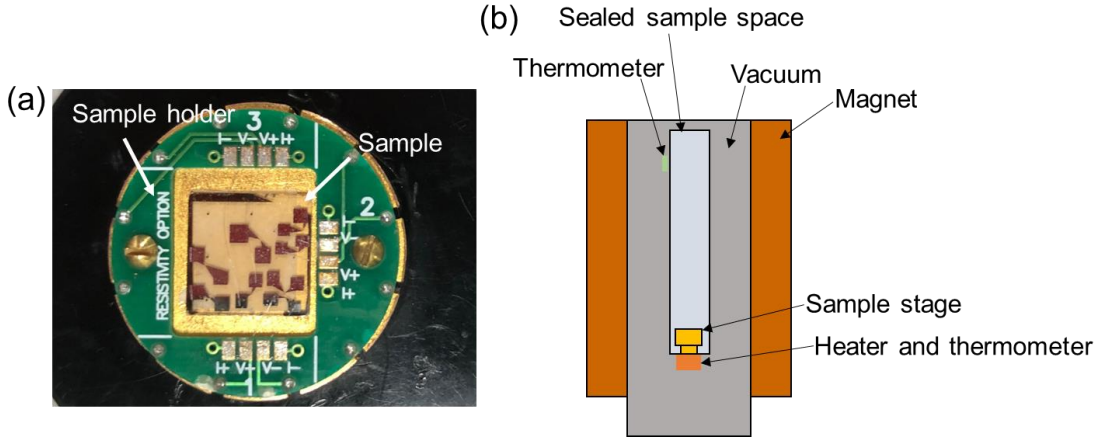

Figure 2.2.3 (a) Image of Fe_3O_4 samples placed on a sample holder for PPMS. (b) Cross-sectional schematic of PPMS.

2.3 Transfer of thin film/hBN stacks

Two-dimensional layered materials including hBN can be transferred onto arbitrary materials owing to weak van der Waals interactions. In my study, a transparent polymer was utilized for the transfer method [2.7]. Figure 2.3.1 shows the schematic of the transfer process. First, transparent PDMS polymer sheet (Gel-Pak film) was exposed to water vapor. The PDMS sheet with water layer on the surface was attached to the stack of thin film/hBN stacks while removing the bubbles formed between the PDMS sheet and thin film at room temperature. Subsequently, the PDMS sheet was peeled off gently to pick up the thin film/hBN stacks. The thin film/hBN stacks were dropped and transferred onto arbitrary materials. Using this transfer method, serious damage such as formation of cracks or wrinkles are avoided. For enhancing adhesive force between the thin film/hBN stacks and the substrate after the transfer process, the samples were baked for 373 K for 10 minutes. This transfer method was partly supported by Dr. Mahito Yamamoto (currently Associate Professor of Kansai University) and Associate Professor Ryo Nouchi of Osaka Metropolitan University.

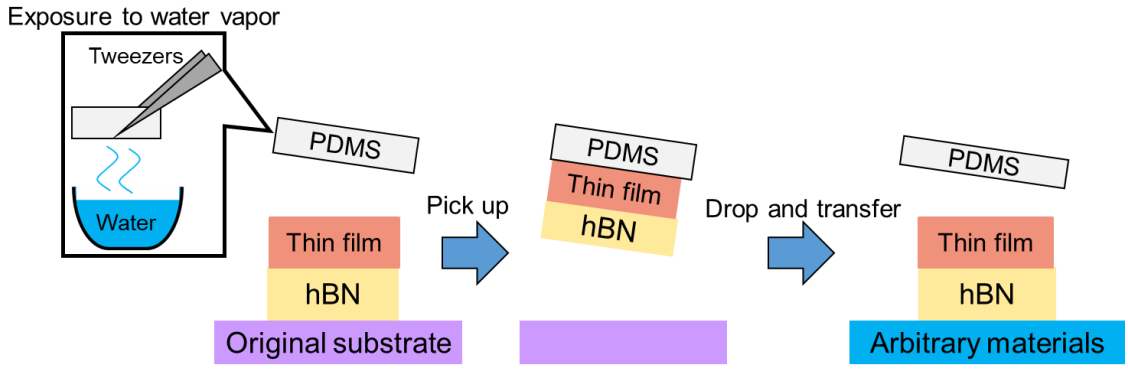

Fig. 2.3.1 Schematic of method for transferring thin film/hBN stacks

2.4 References

[2.1] C. L. Evans and X. S. Xie, Annu. Rev. Anal. Chem., **1**, 883 (2008).

[2.2] T. H. Kauffmann, N. Kokanyan, and M. D. Fontana, J. Raman Spectrosc., **50**, 418 (2019).

[2.3] S. A. C. Gould, K. Burke, and P. K. Hansma, Phys. Rev. B, **40**, 5363 (1989).

[2.4] J. Uppenbrink and J. David, J. Chem. Phys., **96**, 8520 (1992).

[2.5] H. Heinz, R. A. Vaia, B. L. Farmer, and R. R. Naik, J. Phys. Chem. C, **112**, 17281 (2008).

[2.6] Z. L. Wang and J. M. Cowley, Ultramicroscopy, **31**, 437 (1989).

[2.7] X. Ma, Q. Liu, D. Xu, Y. Zhu, S. Kim, Y. Cui, L. Zhong, and M. Liu, Nano Lett., **17**, 6961 (2017).

Chapter 3

Growth and characterization of VO_2 thin films on hBN with transferability

3.1 Introduction

VO_2 exhibits MIT accompanied with giant resistance change and is promising in device application in transition metal oxide electronics. VO_2 has a bandgap of ~0.6 eV and shows a resistance of 3–4 orders of magnitude owing to MIT accompanied with a structural phase transition between monoclinic M1 phase and Rutile phase slightly above room temperature (~340 K) [3.1, 3.2]. Figure 3.1.1(a) and (b) show the schematic of the structural MIT in VO_2 between the insulating monoclinic M1 phase and metallic rutile phase [3.3]. Figure 3.1.1 (c) show the band diagram of the monoclinic M1 phase and the rutile phase. Growth of VO_2 thin films for application in devices, such as transistors [3.4–3.7], sensors [3.8–3.11], smart windows [3.12, 3.13], electrical switching devices [3.14–3.16], and so force has been actively studied. Thus far, high-quality VO_2 thin films have been commonly grown on single oxide substrates, such as TiO_2 [3.17], Al_2O_3 [3.18], $SrTiO_3$ [3.19], and GaN [3.20]. However, the lattice matching plays a significant role in the MIT property in VO_2 thin films grown on these substrates. Studies on the growth of VO_2 thin films on two-dimensional materials, such as mica and graphene, have been reported for application in flexible devices [3.21, 3.22]. However, these materials are chemically unstable or negatively charged under the high-temperature oxygen ambient [3.23, 3.24]. Thus, considering the chemical stability of hBN, hBN is a proper material as a substrate. With hBN as the growth substrate, the relaxation of the lattice matching could be realized, leading to the universal growth of transition metal oxide thin films.

In this work, VO_2 thin films were grown on single-crystal hBN flakes exfoliated from bulk crystals and the surface and cross-sectional structure of the VO_2 thin films were investigated using AFM and STEM, respectively. Then, the MIT property was measured after fabrication of VO_2/hBN microwires two-terminal with electrodes. In addition, the

transfer of VO_2/hBN stacks was performed from the original substrate to arbitrary materials.

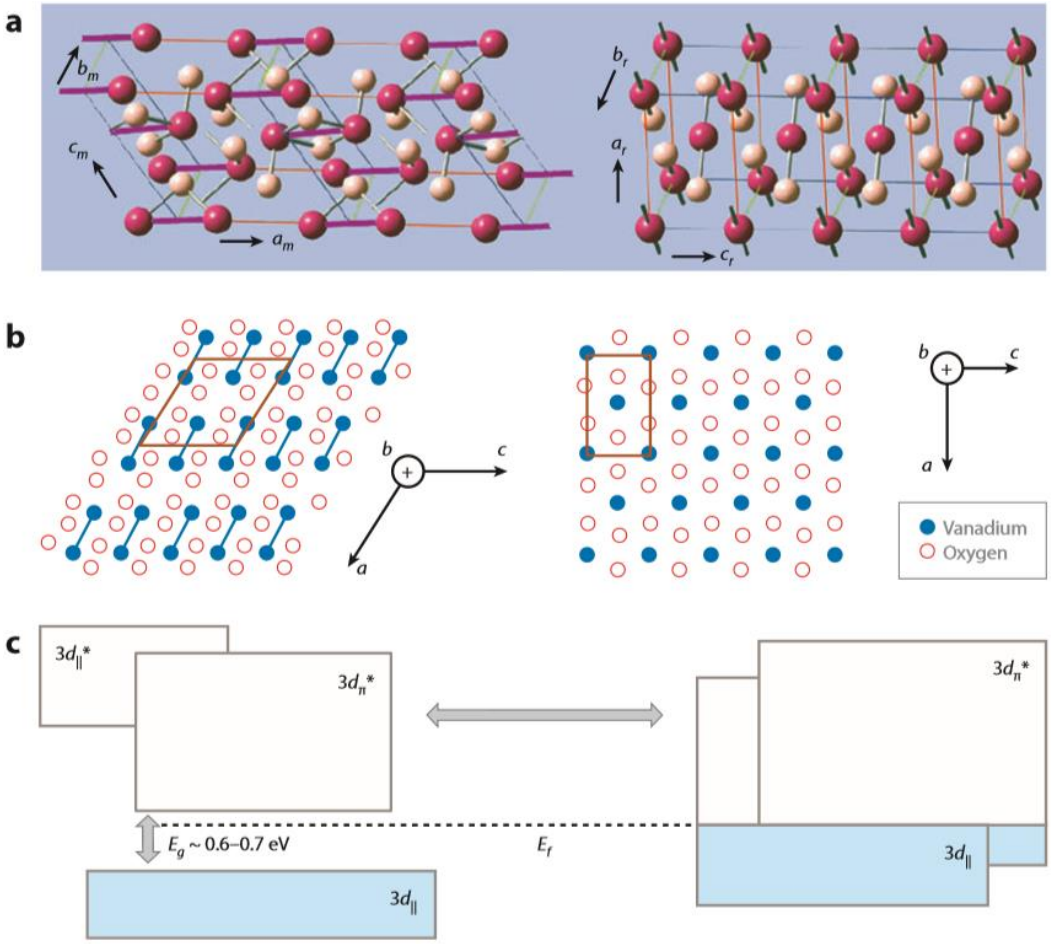

Figure 3.1.1 Structure and band diagram of VO_2. (a, b) Structure change of VO_2 from the monoclinic insulating phase (M1) to the tetragonal rutile metallic phase (R) during MIT. (c) Band structure change of VO_2 across the MIT. The left and right panels show the band structures for the insulating and metallic phases, respectively [3.3].

3.2 Sample preparation and experiments

Figure 3.2.1(a) shows the schematic of the transfer process of hBN flakes onto SiO_2 substrates and preparation of VO_2 thin films. The hBN flakes were mechanically exfoliated from bulk single crystal of hBN and transferred using the Scotch tape. Figure 3.2.1(b) shows the optical microscopy image of the single crystal of hBN on the Scotch tape. The hBN flakes were annealed in an oxygen atmosphere to remove adhesive residue for 3.5 h at 773 K. Figure 3.2.1(c) and (d) show the optical microscopy images of the hBN flakes before and after the growth of thin films, respectively. VO_2 thin films were grown by PLD method using ArF excimer laser (λ=193 nm) under the partial oxygen pressure and substrate temperature of 0.95 Pa and 723 K, respectively. The thicknesses of VO_2 thin films were ~50 nm.

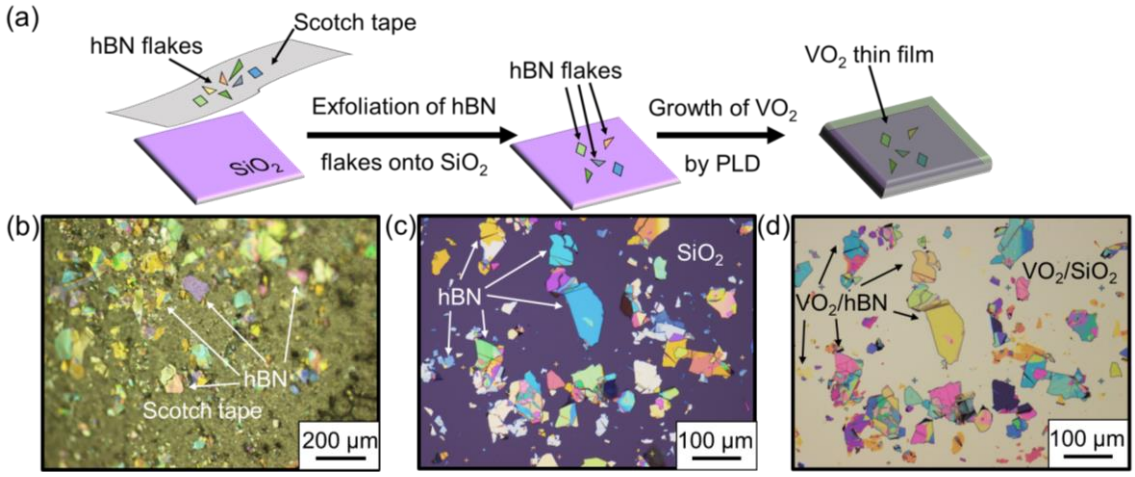

Figure 3.2.1 (a) Schematic of exfoliation and transfer of hBN flakes and growth of VO_2 thin films. (b) Single crystal of hBN on Scotch tape before exfoliation. (c) Optical microscopy image of hBN flakes after exfoliation and transfer. (d) Optical microscopy image of hBN flakes after growth of VO_2 thin films.

The confirmation of the growth of VO_2 thin films was conducted using a Raman system (Raman Touch, Nanophoton) at room temperature with a solid-state laser ($\lambda = 532$ nm). The Raman grating size was 1200 lines/mm. The laser spot size was ~1 μm. The laser power was set to be 1 mW. The surface structural characterization of VO_2 thin films was investigated using AFM5000/5300E (Hitachi High-Tech Corp.) in the dynamic focus mode. Next, identification of the growth orientation of the VO_2 thin films on hBN was conducted using HAADF-STEM. The HAADF-STEM measurements were conducted using a JEOL JEM-ARM200F ACCELARM operated at an acceleration voltage of 200 kV. The probe semi-angle was 18 mrad. The probe current was 9 pA. The angular detection range of the HAADF detector for the scattered electrons was 50–150 mrad.

Figures 3.3.2(a)–(c) show the microwire fabrication flow. After confirmation of the growth of VO_2 thin films on hBN by Raman spectroscopy, a pair of electrodes composed of Pt and Cr were deposited on the stacks of VO_2/hBN using photolithography and sputtering deposition. Then, VO_2/hBN stacks were etched and microwires were formed using photolithography and reactive-ion (RIE) etching under a mixture of O_2 and sulfur hexafluoride gases. The MIT property was measured using a variable temperature Peltier stage with a source meter (2614, Keithley) at 0.1 K step and a ramp/cooling rate of 10 K/min. The transfer of VO_2/hBN stacks was conducted using the transfer method indicated in Chapter 2.3.

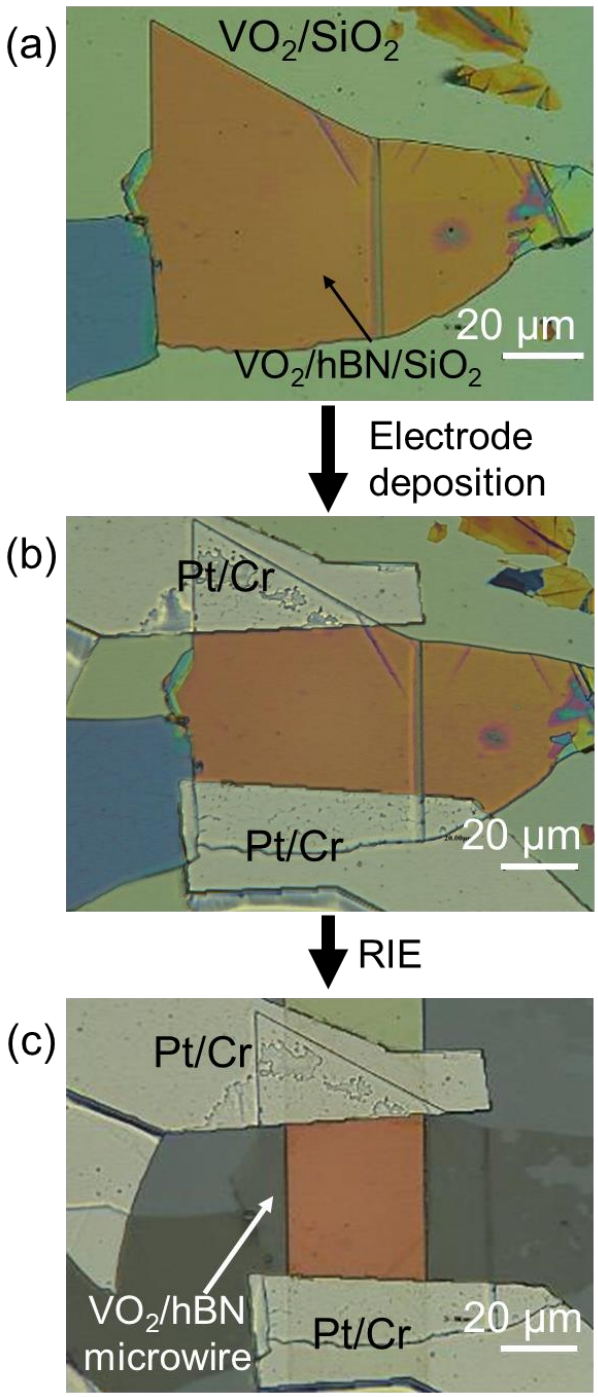

Figure 3.2.2 (a) Optical microscopy image of VO_2/hBN before fabrication of microwires. (b) the VO_2/hBN after electrode deposition with Pt and Cr. (c) the VO_2/hBN after RIE etching.

3.3 Characterization through Raman spectroscopy

Figure 3.3.1 shows Raman spectrum of the VO_2 thin film on hBN in Fig. 3.2.2(a) at room temperature. The Raman peaks observed at 520 and 1367 cm^{-1} were assigned to Si [3.25] and hBN [3.26], respectively. Prominent Raman peaks were observed at 193, 220, 390, 616 cm^{-1} and so forth were identified to be the Raman active A_g and B_g modes of monoclinic VO_2 [3.27, 3.28]. This result indicates the successful formation of VO_2 thin films on hBN.

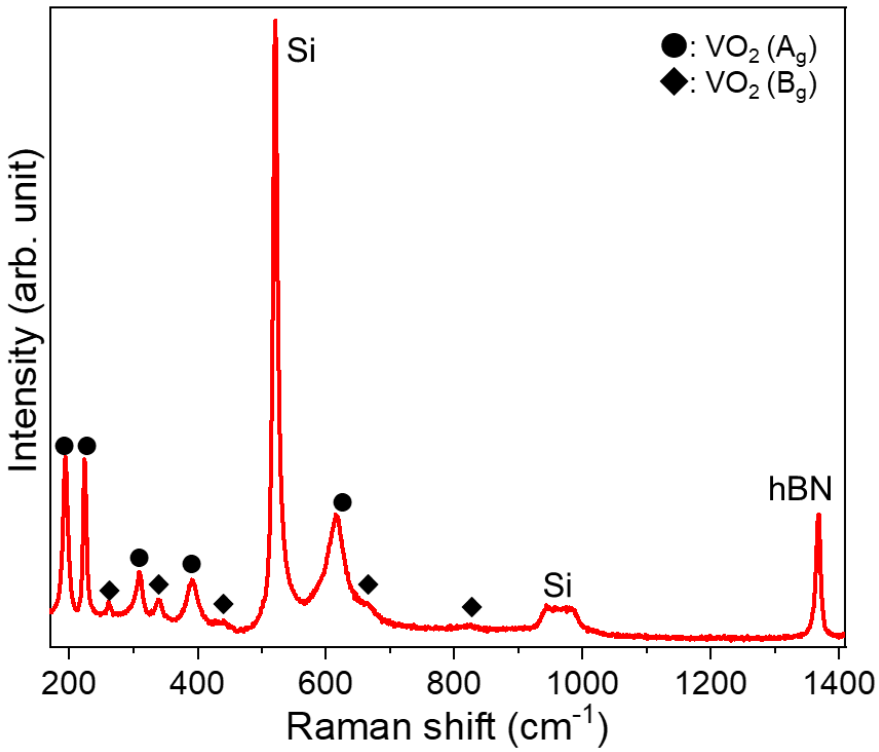

Figure 3.3.1 Raman spectrum of VO_2 thin film on hBN at room temperature.

3.4 Structural characterization of VO_2 thin films on hBN

The in-plane and out-of-plane structure of VO_2 thin films on hBN was characterized using AFM and STEM, respectively. Figures 3.4.1(a) and (b) show the surface morphology of VO_2 thin films on hBN obtained by AFM. It was found that VO_2 thin films have grain structures on the surface. Figure 3.4.2 shows the grain size distribution with

the fitting function. The mean value of the grain size distribution was characterized to be 289 ± 80 nm and up to sub-micrometer scale in length. Compared with VO_2 thin films grown on Al_2O_3, whose grain size of ~50 nm [3.29], the grain size of ~300 nm on the VO_2 thin film on hBN is one order of magnitude larger. The formation of large-sized grain structures implies the relaxation of the lattice strain owing to the weak van der Waals interactions. In addition, the formation of the grain structures indicates that the VO_2 thin films on hBN are polycrystalline.

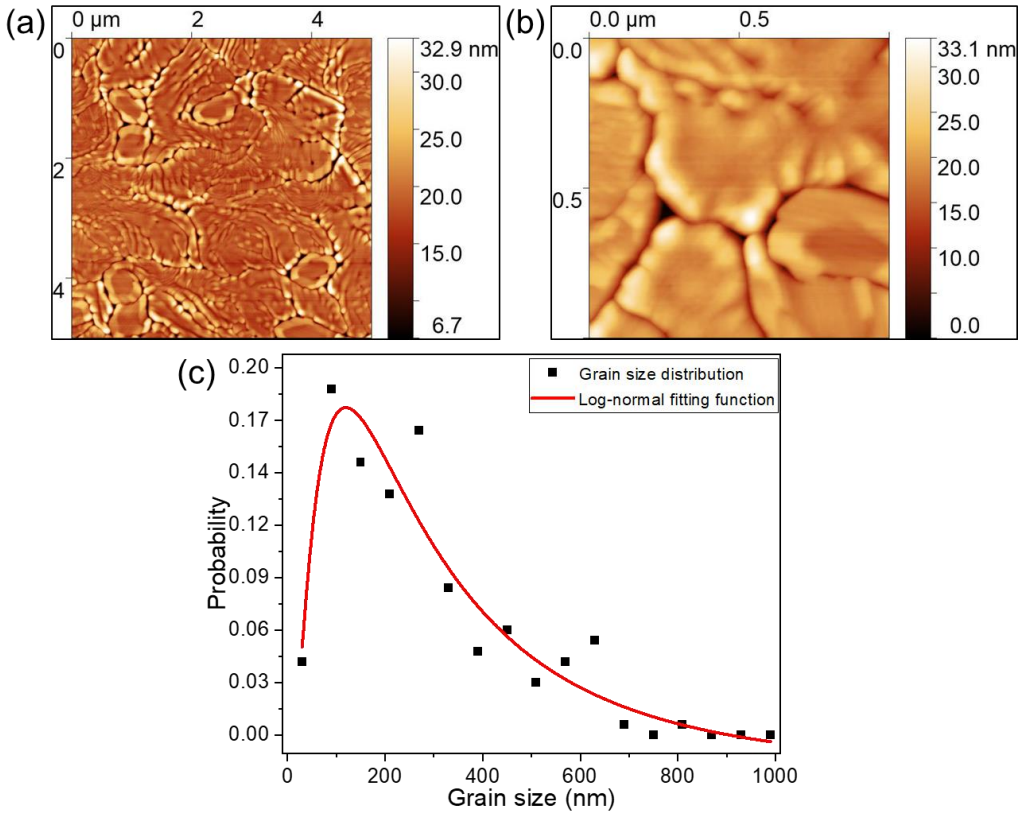

Figure 3.4.1 (a) AFM image of VO_2 thin film on hBN. (b) Magnified AFM image of VO_2 thin film on hBN. (c) Grain size distribution (black plots) and logarithmic-normal fitting function (red curve).

Figure 3.4.2(a) shows the cross-sectional STEM image including the interface of the VO_2 thin film and hBN. Clear lattice arrangement of hBN was observed as shown in the inset of Fig. 3.4.2(a). In addition, parallel atomic arrangement of VO_2 lattices was clearly observed in the red square region in Fig. 3.4.2(a). Figure 3.4.2(b) shows the magnified STEM image of the VO_2 lattices. It was discovered that the lattices of VO_2 were arranged with periodicity and the distance between each crystal plane was 0.325 nm along the perpendicular direction and 0.167 nm along the diagonal direction, respectively. Figure 3.4.2(c) shows the fast Fourier transformation (FFT) image of the VO_2 lattices in Fig. 3.4.2(b). It was found that the FFT spots correspond to the projection of $(1\bar{1}3)$ plane of the rutile phase in the reciprocal space. Importantly, VO_2 thin films were found to be oriented along [110] direction in the rutile phase to hBN (001) plane. It has been reported through First-principle calculations that rutile-VO_2(110) plane is the most energetically favorable among VO_2 planes in rutile phase [3.30].

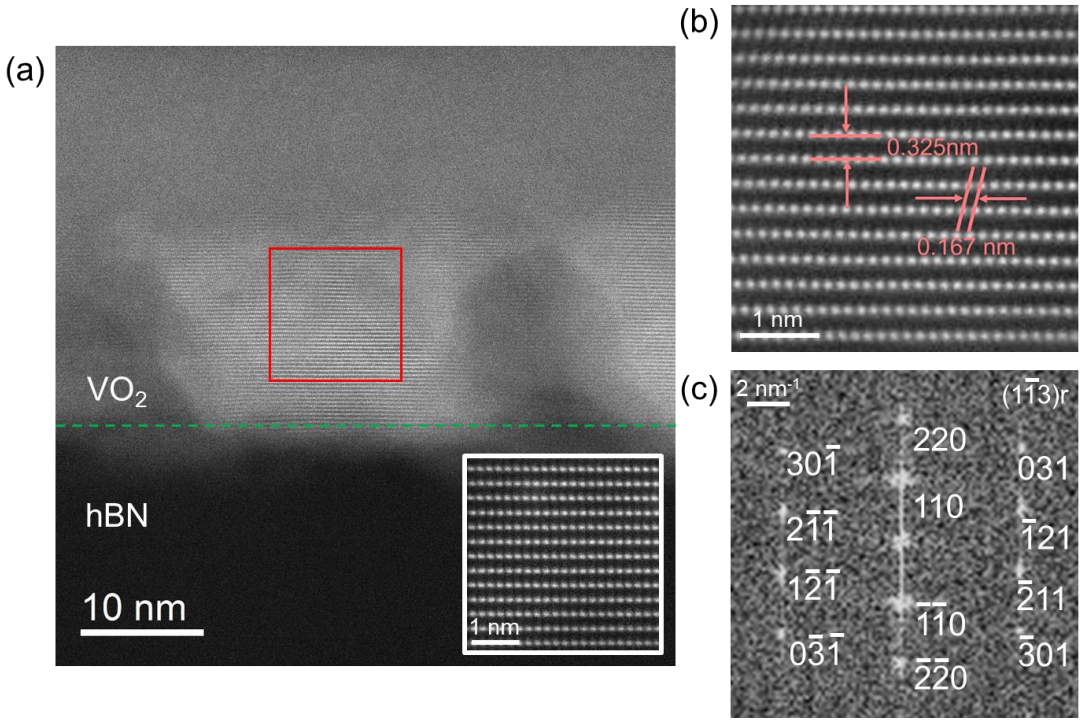

Figure 3.4.2 (a) Cross-sectional STEM image of VO_2 thin film and hBN including the interface. The upper and upper regions are VO_2 and hBN, respectively. The white inset indicates the atomically-resolved STEM image of hBN. The red square region is the area, where atomically-oriented VO_2 lattices were observed. (b) Atomically-resolved STEM image of VO_2 in the red square area in (a). (c) FFT image of the VO_2 projected along $[1\bar{1}3]$ direction of rutile-VO_2.

Here, the lattice mismatch between planes of VO_2 and hBN(001) is discussed in detail. The lattice mismatch is defined as $\frac{|a_{sub}-a_{film}|}{a_{sub}} \times 100$ along rutile-VO_2[110] and rutile-VO_2[001] directions. Figure 3.4.3 indicates the schematic of the lattice arrangement of rutile-VO_2 on hBN(001). The lattice mismatch between rutile-VO_2(110) and hBN(001) was calculated to be 12% and 14% along rutile-$VO_2[1\bar{1}0]$ and rutile-VO_2[001] directions, respectively. Here, the total lattice mismatch between rutile-VO_2(110) and hBN(001) was estimated to be the geometric mean value, 13%. Using this estimation method for the lattice mismatch, the rutile-VO_2(010) plane have smaller lattice mismatch, in total 9%

than the rutile-VO_2(110) plane. Generally, growth of transition metal oxide thin films occurs with small lattice mismatch due to energetic restriction. However, the growth of VO_2 planes on hBN(001) was realized with the energetically favorable planes of rutile-VO_2 despite the existence of larger lattice mismatch. This should originate from the weak connection force at the interface with van der Waals interactions.

The competition between the energy of van der Waals interactions and the surface energy of rutile-VO_2 plane is discussed. The surface energy of rutile-VO_2(110) plane calculated by theoretical calculation is 0.29 J/m^2 [3.30]. The order of van der Waals interactions is 1.0×10^4 J/mol [3.31]. When 1 m^2-sized square is covered with atoms with the size of 1 Å, the total number of the atoms are $10^{10} \times 10^{10} = 10^{20}$. This is equal to 1.67×10^{-4} mol. Thus, the energetic order of van der Waals interactions in 1 m^2 is equal to $1.0 \times 10^4 \times 1.67 \times 10^{-4} = 1.67$ J/m^2. This value is comparable to the surface energy of VO_2(110) plane. Considering that energy of van der Waals interactions is two orders of magnitude weaker than that of covalent or ionic force [3.31], growth of VO_2 thin films on hBN is estimated to be governed by minimization of surface energy ignoring interface interaction, whereas that on single-crystal oxide substrates are governed by lattice matching owing to strong ionic/covalent force. Therefore, growth unique mechanism of VO_2 thin films on hBN can be explained by weak van der Waals interactions and surface energy.

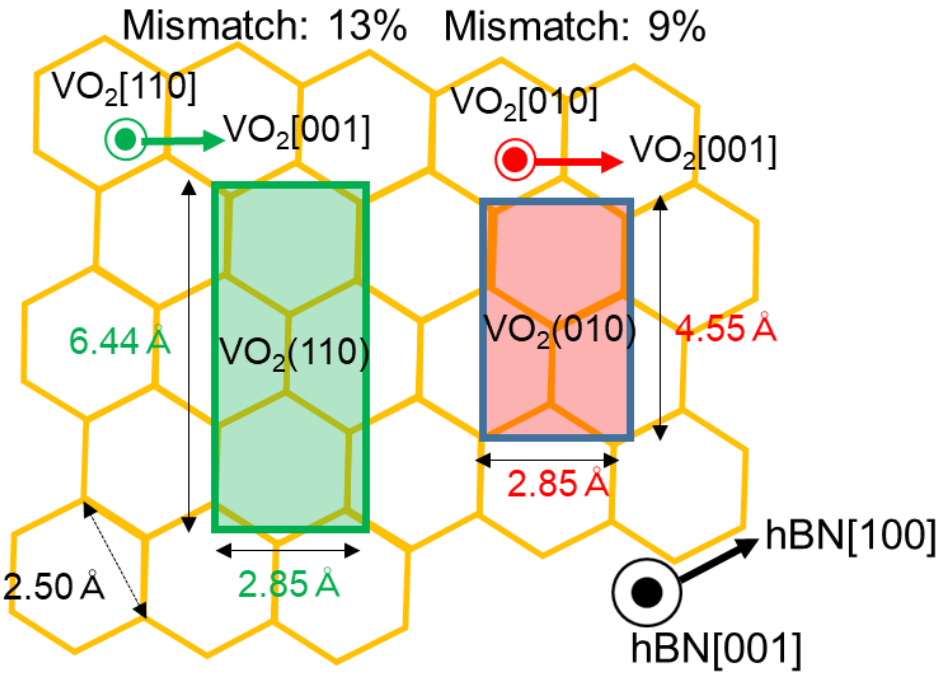

Figure 3.4.3 Schematic of in-plane lattice arrangement of rutile-VO_2(110) and rutile-VO_2(010) on hBN(001).

3.5 Characterization of MIT property in VO_2/hBN

Figure 3.5.1 shows the temperature-dependent resistance curves (*R*–*T* curves) of the VO_2/hBN microwire shown in Fig. 3.2.2 (c). A resistance change of three orders of magnitude was observed with the transition temperature of approximately 340 K, which is same as the transition temperature of a bulk crystal of VO_2 [3.1, 3.2]. Combined with the indication of the relaxation of lattice strain in Chapter 3.4, it is reasonable that the transition temperature was same as that of a bulk VO_2 crystal. The order of magnitude of the resistance change owing to MIT is comparable to that grown on TiO_2 and Al_2O_3 substrates [3.17, 3.18], which guarantees high-quality VO_2 thin films. In addition, it is notable that a significant resistivitance jump was observed during MIT in the VO_2/hBN microwire. Generally, the electric conduction in the VO_2 is governed by the manners of percolative conduction pass [3.32], where spatial elements called metallic domains play

an important role [3.33]. When the number of the metallic domains is reduced, resistance changes showing resistance jumps are observed [3.34]. For example, VO_2 nanowires on Al_2O_3(0001) substrates exhibit step-like resistance changes since tens of nanometer-sized domains were confined [3.34] in the nanowire, whereas the VO_2 thin films show gradual resistance change [3.34]. Thus, the resistance jump in the VO_2/hBN microwire implies that confinement effect of the metallic domains in the micrometer scale.

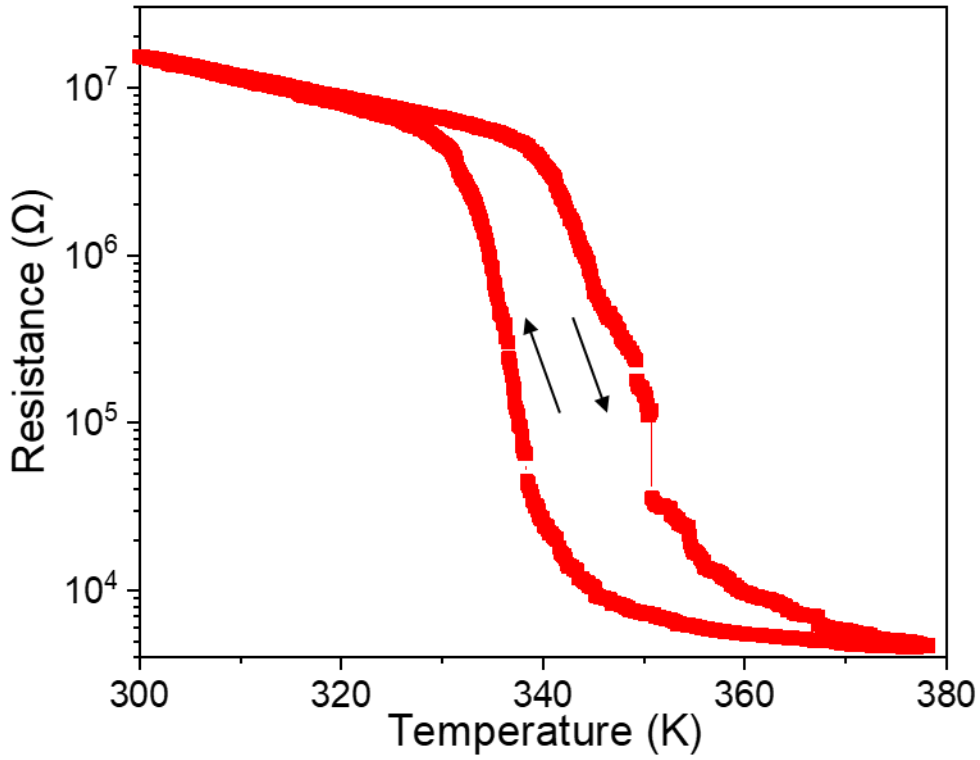

Figure 3.5.1 *R–T* curves of the VO_2/hBN microwire accompanied with a prominent MIT.

3.6 Transfer of VO_2/hBN stacks

Owing to the transferability of hBN, the stacks of VO_2/hBN are expected to be applicable to transferable and flexible devices. Here, the transfer of the VO_2/hBN stacks was attempted using transparent polymer after exposure to water vapor [3.35]. Figures 3.6.1(a)–(c) show the optical microscopy images of the VO_2/hBN stacks after the transfer process. Interestingly, the stacks of VO_2/hBN were successfully transferred onto arbitrary materials: glass, Au, and paper, where VO_2 thin films cannot be grown directly. Raman spectroscopy was measured to confirm the existence of VO_2 thin films on hBN after transfer process. Raman peaks attributable to A_g and B_g modes of VO_2 were clearly observed in all the transferred VO_2/hBN stacks [3.27, 3.28]. The peaks except VO_2 and hBN were assigned as those of glass and paper in Fig. 3.6.1(d) and (f), respectively [3.36, 3.37].

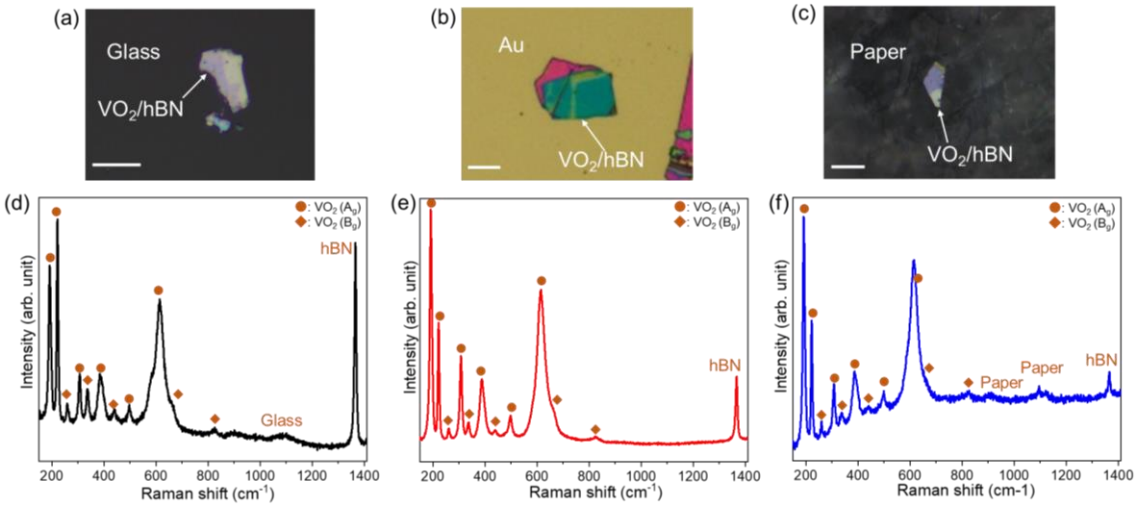

Figure 3.6.1 Optical microscopy images of VO_2/hBN stacks transferred onto (a) glass, (b) Au, and (c) paper. The scale bars are 10 μm. Raman spectra of the VO_2/hBN stacks after transfer onto (d) glass, (e) Au, and (f) paper. The prominent Raman peaks attributable to Ag and Bg modes were indicated with circles and squares. The Raman peaks of hBN is indicated with brown letters.

The MIT property of the transferred VO_2/hBN stack was also measured after deposition of a pair of electrodes. Figure 3.6.2(a) shows the optical microscopy image of the transferred VO_2/hBN stack onto a SiO_2 substrate. Figure 3.6.2(b) shows the *R*–*T* curves of the transferred VO_2/hBN stack (Fig. 3.6.2(a)). A resistance change of 3 orders of magnitude was observed with the transition temperature of approximately 340 K. This result shows that the MIT property VO_2/hBN stack hardly changes before and after the transfer process. The stable properties of the VO_2/hBN stacks can open a way for various device application using transferability, such as smart windows, paper electronics and so forth.

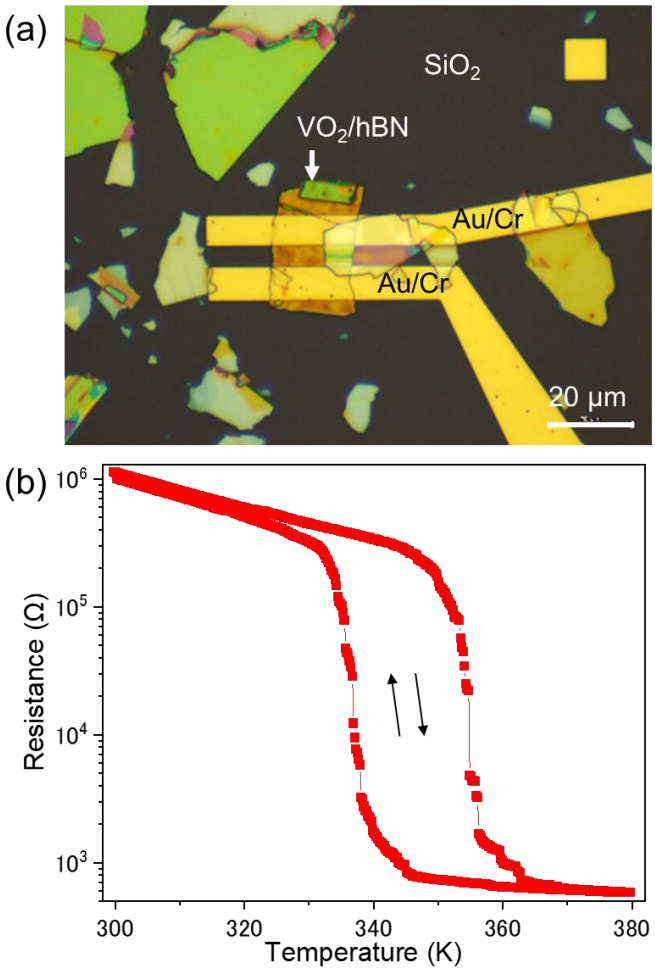

Figure 3.6.2 (a) Optical microscopy image of transferred VO_2/hBN stacks with Au/Cr electrodes. (b) *R*–*T* curves of the transferred VO_2/hBN stacks.

3.7 Conclusion

In this study, the growth of VO_2 thin films on single-crystal hBN flakes exfoliated from bulk crystals was demonstrated. The VO_2 thin films on hBN were observed to have grain structures with the mean size of several hundred nanometers. The rutile-VO_2(110) plane was observed to grow on hBN(001). The rutile-VO_2(110) plane is predicted to be the most energetically stable by the theoretical calculation. The formation of large-sized grain structures and the growth of the energetically favorable planes indicates the relaxation of the interfacial lattice matching owing to weak van der Waals interactions. VO_2 thin films on hBN undergo MIT at approximately 340 K, with a resistance change of nearly three orders of magnitude. The resistance change, which is comparable to those of VO_2 films grown on common substrates shows preparation of high-quality VO_2 thin films on hBN. Therefore, hBN has a potential of a growth substrate beyond the lattice mismatch. The transferability of VO_2/hBN stacks is one of the advantages for various application.

3.8 References

[3.1] F. J. Morin, Phys. Rev. Lett., **3**, 34 (1959).

[3.2] C. N. Berglund and H. J. Guggenheim, Phys. Rev., **185**, 1022 (1969).

[3.3] Z. Yang, C. H. Ko, and S. Ramanathan, Annu. Rev. Mater. Res., **41**, 337 (2011).

[3.4] K. Liu, D. Fu, J. Cao, J. Suh, K. X. Wang, C. Cheng, D. F. Ogletree, H. Guo, S. Sengupta, A. Khan, C. W. Yeung, S. Salahuddin, M. M. Deshmukh, and J. Wu, Nano Lett., **12**, 6272 (2012).

[3.5] M. A. Belyaev, V. V. Putrolaynen, A. A. Velichko, and G. B. Stefanovich, Jpn. J. Appl. Phys., **53**, 111102 (2014).

[3.6] T. Wei, T. Kanki, K. Fujiwara, M. Chikanari, and H. Tanaka, Appl. Phys. Lett., **108**, 053503 (2016).

[3.7] H.-T. Kim, B.-G. Chae, D.-H. Youn, S.-L. Maeng, G. Kim, K.-Y. Kang, and Y.-S. Lim, New J. Phys., **6**, 52 (2004).

[3.8] E. Strelcov, Y. Lilach, and A. Kolmakov, Nano Lett., **9**, 2322 (2009).

[3.9] B. Hu, Y. Ding, W. Chen, D. Kulkarni, Y. Shen, V. V. Tsukruk, and Z. L. Wang, Adv. Mater., **22**, 5134 (2010).

[3.10] J. W. Byon, M.-B. Kim, M. H. Kim, S. Y. Kim, S. H. Lee, B. C. Lee, and J. M. Baik, J. Phys. Chem. C, **116**, 226 (2012).

[3.11] F. Liao, Z. Zhu, Z. Yan, G. Yao, Z. Huang, M. Gao, T. Pan, Y. Zhang, Q. Li and X. Feng, and Y. Lin, J. Breath Res., **11**, 036002 (2017).

[3.12] S. Chen, Z. Wang, H. Ren, Y. Chen, W. Yan, C. Wang, B. Li, J. Jiang, C. Zou, Sci. Adv. **5**, eaav6815 (2019).

[3.13] R. Li, S. Ji, Y. Li, Y. Gao, H. Luo, and P. Jin, Mater. Lett., **110**, 241 (2013).

[3.14] G. Stefanovich, A. Pergament, and D. Stefanovich, J. Phys.: Condens. Matter, **12**,

8837 (2000).

[3.15] P. P. Boriskov, A. A. Velichko, A. L. Pergament, G. B. Stefanovich, and D. G. Stefanovich, Tech. Phys. Lett., **28**, 406 (2002).

[3.16] A. Crunteanu, J. Givernaud, J. Leroy, D. Mardivirin, C. Champeaux, J.-C. Orlianges, A. Catherinot, and P. Blondy, Sci. Technol. Adv. Mater., **11**, 065002 (2010).

[3.17] T. Kanki, K. Kawatani, H. Takami, and H. Tanaka, Appl. Phys. Lett., **101**, 243118 (2012).

[3.18] H. Takami, K. Kawatani, T. Kamki, and H. Tanaka, Jpn. J. Appl. Phys. Part 1, **50**, 055804 (2011).

[3.19] A. Chen, Z. Bi, W. Zhang, J. Jian, Q. Jia, and H. Wang, Appl. Phys. Lett., **104**, 071909 (2014).

[3.20] Y. Zhou and S. Ramanathan, J. Appl. Phys., **112**, 074114 (2012).

[3.21] H. Kim, Y. Kim, K.S. Kim, H. Y. Jeong, A.-R. Jang, S.H. Han, D.H. Yoon, K.S. Suh, H.S. Shin, T.Y. Kim, W.S. Yang, ACS Nano, **7**, 5769 (2013).

[3.22] J. Yan, W. Huang, Y. Zhang, X. Liu, M. Tu, Phys. Status Solidi A, **205**, 2409 (2008).

[3.23] E. Starodub, N. C. Bartelt, and K. F. McCarty, J. Phys. Chem. C, **114**, 5134 (2010).

[3.24] H. K. Christenson and N. H. Thomson, Surf. Sci. Rep., **71**, 367 (2016).

[3.25] J. H. Parker, Jr., D. W. Feldman, and M. Ashkin, Phys. Rev., **155**, 712 (1967).

[3.26] R. Geick, C. H. Perry, and G. Rupprecht, Phys. Rev., **146**, 543 (1966).

[3.27] K. Okimura, N. H. Azhan, T. Hajiri, S.-I. Kimura, M. Zaghrioui, and J. Sakai, J. Appl. Phys., **115**, 153501 (2014).

[3.28] M. Pan, J. Liu, H. Zhong, S. Wang, Z.-F. Li, X. Chen, and W. Lu, J. Cryst. Growth, **268**, 178 (2004).

[3.29] J. Sang, T. Zheng, L. Xu, X. Zhou, S. Tian, J. Sun, X. Xu, J. Wang, S. Zhao, and Y.

Liu, J. Alloys Compd., **876**, 160208 (2021).

[3.30] T. A. Mellan and R. Grau-Crespo, J. Chem. Phys., **137**, 154706 (2012).

[3.31] Y. Liu, Y. Huang, and X. F. Duan, Nature, **567**, 323 (2019).

[3.32] J. Rozen, R. Lopez, R. F. Haglund, Jr., and L. C. Feldman, Appl. Phys. Lett., **88**, 081902 (2006).

[3.33] M. M. Qazilbash, M. Brehm, G. O. Andreev, A. Frenzel, P.-C. Ho, B.-G. Chae, B.-J. Kim, S. J. Yun, H.-T. Kim, A. V. Balatsky, O. G. Shpyrko, M. B. Maple, F. Keilmann, and D. N. Basov, Phys. Rev. B, **79**, 075107 (2009).

[3.34] H. Takami, T. Kanki, and H. Tanaka, Appl. Phys. Lett., **104**, 023104 (2014).

[3.35] X. Ma, Q. Liu, D. Xu, Y. Zhu, S. Kim, Y. Cui, L. Zhong, and M. Liu, Nano Lett., **17**, 6961 (2017).

[3.36] A. K. Yadav and P. Singh, RSC Adv., **5**, 67583 (2015).

[3.37] U. P. Agarwal, S. A. Ralph, C. Baez, and R. S. Reiner, Cellulose, **28**, 9069 (2021).

Chapter 4

Characterization of size-dependent MIT property in VO_2/hBN microwires

4.1 Introduction

As reported in Chapter 3, the VO_2 thin films grown on hBN show prominent MIT, meaning the high potential for functionalities of high-quality VO_2 thin films on hBN. When we consider the device application using VO_2 thin films on hBN, the determination of the size of a special element called metallic domain is essential. It is known that the MIT property in VO_2 is generally governed by the emergence of the metallic domains [4.1, 4.2]. Generally, the size of metallic domains is sensitive to the quality of VO_2 thin films, namely, dependent on the substrate materials. For example, Figure 4.1.1 show the electronic phase separation phenomena, where metallic domains of a VO_2 thin film grown on $Al_2O_3(\bar{1}012)$ substrate were observed by scanning near-field infrared microscopy (SNIM) [4.1]. The insulator and metallic domains coexist through the MIT process, where the metallic domain size of VO_2 thin films grown on $Al_2O_3(0001)$ substrates is reported to be 50−70 nm [4.3]. The electric transport properties of the VO_2 thin films are dominated by the competition of the metal and insulator domains. Thus, when the sample sizes are comparable to that of individual metallic domains, steep single- or multilevel step resistance changes are observed [4.3]. To obtain multi-level step-like resistance changes, nanowires have been fabricated to reduce the number of metallic domains for obtaining steep resistance changes owing to MIT.

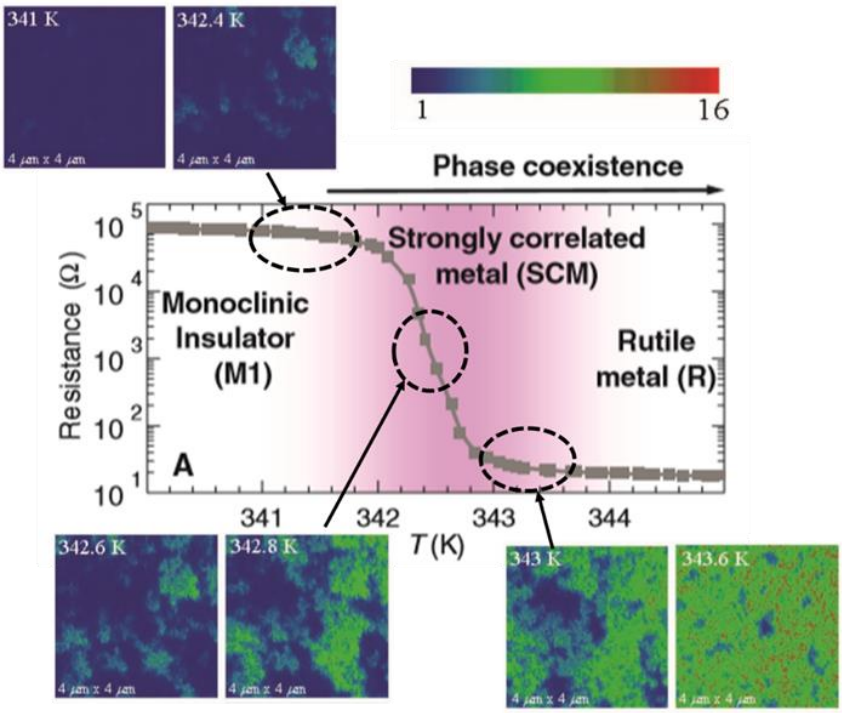

Figure 4.1.1 Electronic phase separation during metal-insulator transition in VO_2 thin films on Al_2O_3(0001) observed by SNIM [4.1].

On the other hand, in the VO_2 thin films on TiO_2 substrates, a single-step resistance change changing by one order of magnitude in microwires has been reported [4.4, 4.5] owing to the micro-sized domains. In detail, the VO_2 thin films on TiO_2 substrates have two types of metallic domains: micro-sized domains and nano-sized domains as shown in Figure 4.1.2. The size of metallic domains is restricted by cracks formed on the surface and their sizes are dependent on the film thicknesses and/or crystal qualities [4.4–4.6]. The nano-sized metallic domains have been observed through Kelvin probe force microscopy [4.7, 4.8] and they are regarded as the original element to induce MIT. Based on these backgrounds, it is important to determine the metallic domain size and it is necessary that the device size is small, on the order of the metallic domain size to obtain a steep and large resistance change since it can be a critical factor for enhancing the performance of the device using the MIT of VO_2 thin films.

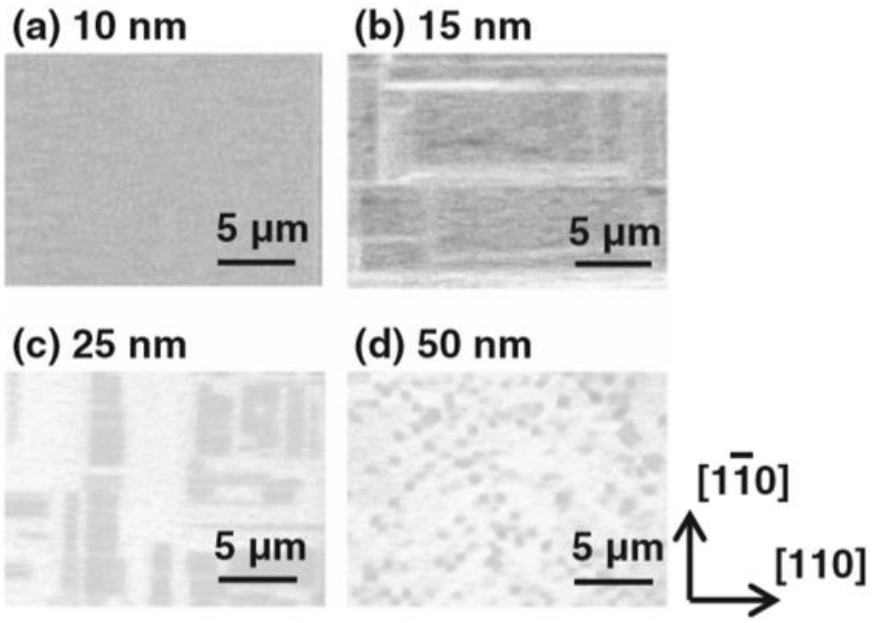

Figure 4.1.2 Optical microscopy images of VO_2 thin films on TiO_2 (001) substrate during MIT with thicknesses of (a) 10 nm, (b) 15nm, (c) 25nm, and (d) 50nm. Dark region is metal and the other region is insulator [4.6].

In this chapter, the emergence of the metallic domains in VO_2 thin films on hBN was observed and the metallic domain size was determined to be ~500 nm on average in length and up to sub-micrometer scale from optical microscopy images. Furthermore, the device-size-dependent MIT property of VO_2 thin films grown on hBN was investigated by electric transport measurements using microwires. The multi-level step-like resistance changes were prominently observed when the width and the length were small enough to be comparable to the metallic domain size, ~2 μm. Notably, the giant single-step resistivity change changing by two orders owing to the confined metallic domains was observed.

4.2 Sample preparation and experiments

The hBN flakes were mechanically exfoliated from bulk hBN single crystals and transferred onto SiO_2/Si substrates, and the flakes were annealed in an oxygen atmosphere to remove the adhesive residue. Pulsed laser deposition (PLD) was utilized to grow VO_2 thin films with sintered V_2O_5 as a target and an excimer laser (193 nm). The partial oxygen pressure was 0.95 Pa and the substrate temperature was 723 K. The thickness of the VO_2 thin film was 80 nm. The crystallinity of the VO_2 thin films grown on hBN was characterized by temperature-dependent Raman spectroscopy (Raman touch, Nano photon) with a solid-state laser (532 nm). The laser spot size was ~1 μm and the grating was 1200 lines/mm. Temperature-dependent *in situ* Raman spectroscopy was conducted at 300 K, 342 K, and 380 K on a temperature-controllable stage to identify the metallic domains. Next, temperature-dependent optical microscopy images were obtained to determine the metallic domain size. The metallic domain size was defined as the full width at half maximum of fitting Gaussian curves in the line profile of the color contrast. The cover ratio of the metallic domains over the observed area was calculated by binarization of the optical microscopy images.

For electric transport measurements, a pair of electrodes were deposited by photolithography and sputtering deposition on VO_2/hBN flakes, and subsequently, VO_2/hBN microwires were fabricated by photolithography and reactive ion etching under a mixture of O_2 and sulfur hexafluoride gases. The temperature-dependent resistivity of VO_2/hBN microwires was measured in air ambient on a thermally conductive Peltier stage in 0.1 K steps at a ramping/cooling rate of 1.5 K/min. To obtain the resistivity–temperature (*R–T*) curves with device size dependence, three microwires with different widths and lengths were fabricated as shown in Table 4.2.1. Although the VO_2/hBN

microwires were fabricated from VO_2/hBN flakes different from that used for Raman spectroscopy measurement, they were prepared under the same experimental condition. Note that wire (2) was fabricated by etching from wire (1) to reduce the width of the microwire.

Table 4.2.1. Sizes of VO_2/hBN microwires

	Length (L)	Width (W)
Wire (1)	23.5 μm	12.7 μm
Wire (2)	23.5 μm	2.6 μm
Wire (3)	1.1 μm	2.6 μm

4.3 Characterization of metallic domains through Raman spectroscopy

Figure 4.3.1(a) shows the optical microscopy image of the target VO_2/hBN flake on the SiO_2/Si substrate, confirming the homogeneous formation of the thin film. Figure 4.3.1(b) shows the Raman spectra of the VO_2 thin film grown on hBN at 300 K and 380 K. Clear Raman peaks observed at 193, 223, 391, and 615 cm^{-1} and so forth were attributable to Raman active Ag and Bg modes of VO_2 of the insulating monoclinic M1 phase [4.9, 4.10] in addition to the Raman peaks of Si at 520 cm^{-1} [4.11] and hBN at 1367 cm^{-1} [4.12], respectively at 300 K. The Raman peaks of VO_2 of the M1 phase disappeared at 380 K, implying that the VO_2 thin film grown on hBN underwent MIT accompanied by the structural change from the M1 phase to the rutile phase.

Figure 4.3.2(a) shows a magnified monochrome optical microscopy image of the VO_2/hBN flake at 342 K during MIT. In this image, an inhomogeneous geometry composed of a gray region and black dots whose size was on the order of hundreds of nanometers was observed. Figure 4.3.2(b) shows the Raman spectra of the VO_2 thin film

grown on hBN at 342 K. In the gray region, the Raman peaks attributable to the M1 phase were observed. On the other hand, the Raman spectra at a black dot exhibited no Raman peaks attributable to the M1 phase, similarly observed for the VO_2 thin film at 380 K. As shown in Fig. 4.3.2(c), in a minority, Raman peaks observed at 200 cm^{-1} and 642 cm^{-1} were assigned as the monoclinic M2 phase [4.10] in addition to the Raman peaks attributable to the M1 phase Although the M2 phase was not able to be optically distinguished by the color contrast, these results suggest that the gray region and the black dots correspond to the insulator phase and the metallic phase, respectively.

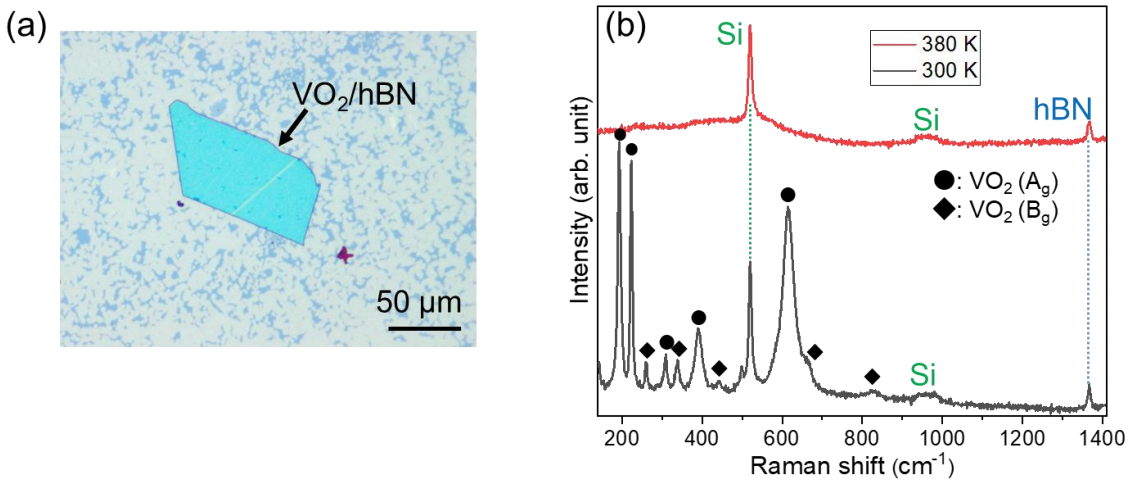

Figure 4.3.1 (a) Optical microscopy image of the target VO_2/hBN stack. (b) Raman spectra of the VO_2/hBN at 300 K (black line) and 380 K (red line).

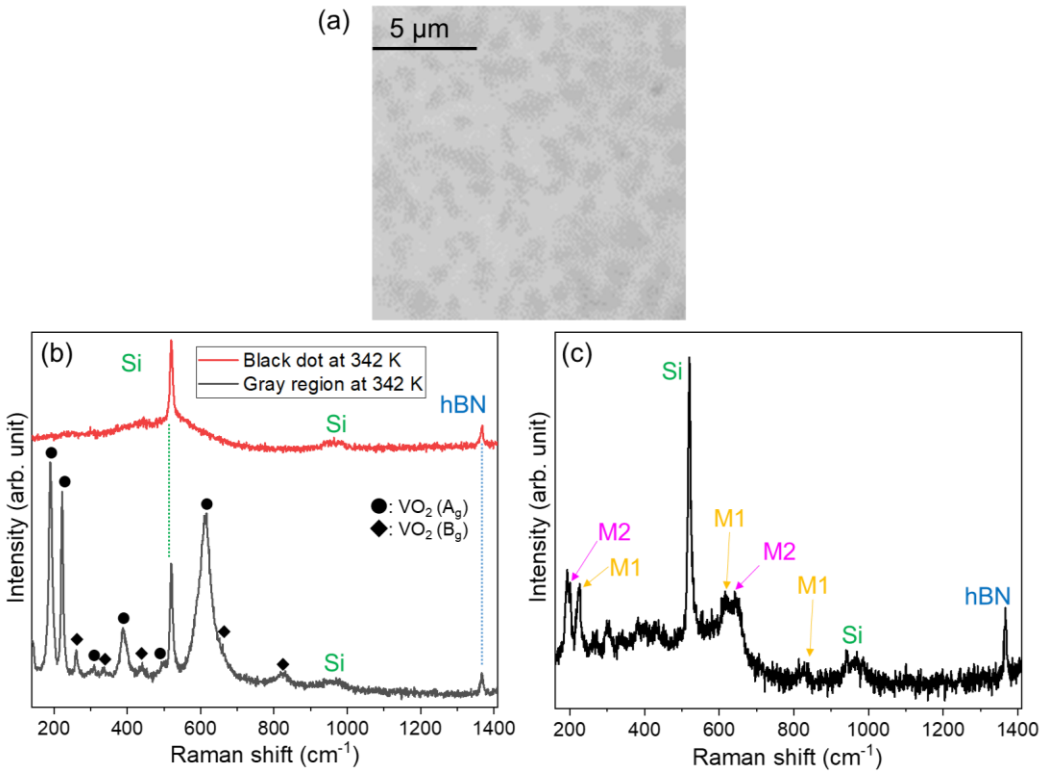

Figure 4.3.2 (a) Magnified monochrome optical microscopy image of the VO_2/hBN flake at 342 K composed of black dots and gray region. (b) Raman spectra of the VO_2/hBN flake at the gray region and a black dot at 342 K. The green and blue dotted lines inducate the Raman peaks of Si and hBN, respectively. (c) Raman spectrum of the VO_2/hBN flake at 342 K. Yellow and pink arrows indicate Raman peaks attributable to the M1 and M2 phases of VO_2.

4.4 Statistical observation of the metallic domains

To determine the metallic domain size, temperature-dependent optical microscopy images were obtained. Figure 4.4.1(a) shows the magnified temperature-dependent optical microscopy images of the flake in the same region. Upon heating to 360 K, the metallic domains, which correspond to dark blue dots, appeared and a clear change in the color contrast was observed. The color contrast was found to return to the initial one after cooling to 300 K. Figure 4.4.1(b) shows the temperature-dependent cover ratio of the metallic domains over the entire area of the optical microscopy images. Note that the

cover ratio was defined to be 0% at 300 K and 100% at 360 K, respectively since the entire area of the images was covered by the insulator and the metallic domains at each temperature. The temperature-dependent cover ratio exhibited hysteresis characteristics with a sharp increase above 340 K during the heating process. The increase in the cover ratio of the metallic domains is consistent with the resistance change above 340 K in the *R*–*T* curves of the VO_2/hBN microwire as shown in Fig. 3.5.1.

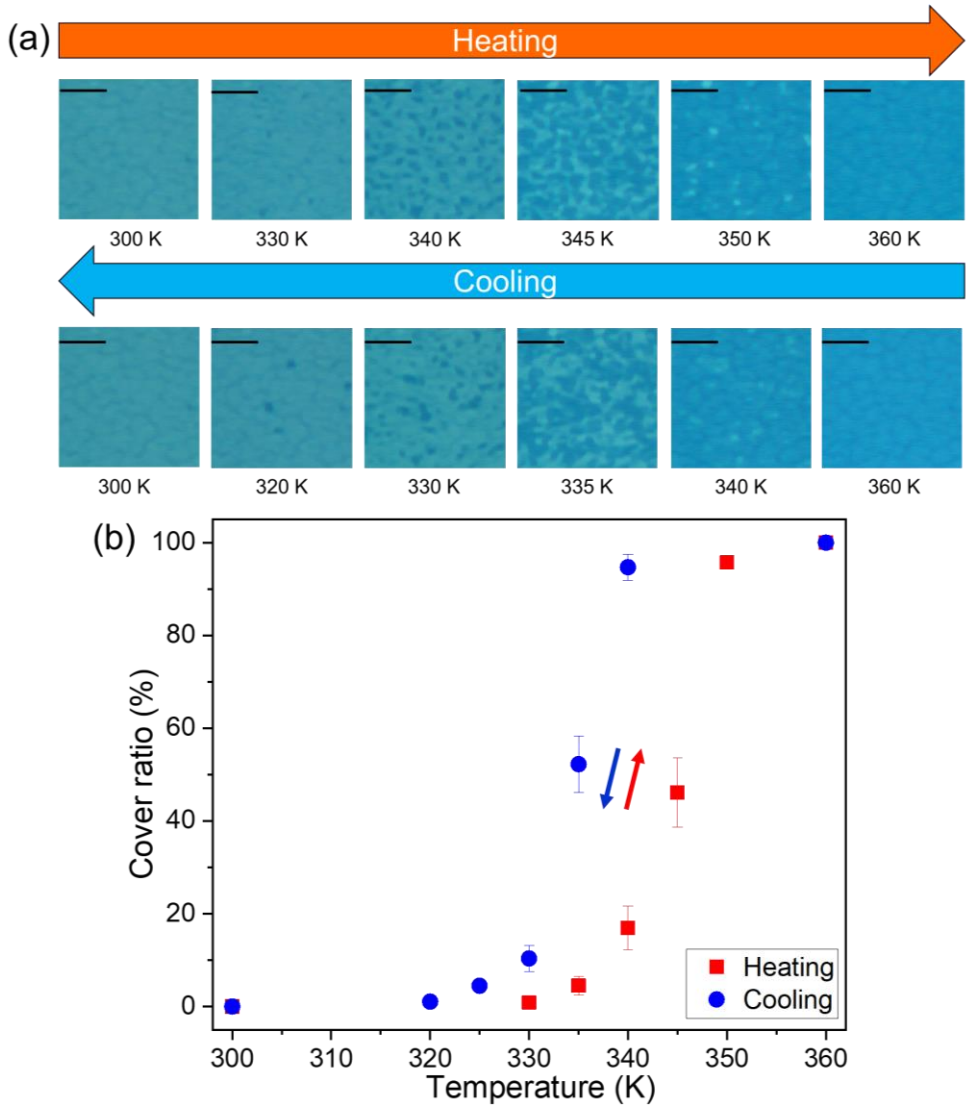

Figure 4.4.1 (a) Magnified temperature-dependent optical microscopy images of flake (1) in the same region. The scale bars are 5 μm. (b) Temperature-dependent cover ratio of metallic domains. The red and blue curves correspond to the heating and cooling processes, respectively.

Figure 4.4.2(a) shows the magnified temperature-dependent optical microscopy images of the VO_2/hBN flake at 331, 333, and 336 K. The optical microscopy images were obtained at these temperatures since the metallic domains start to appear around 330 K. Note that the images were obtained in the same region in each flake. The individual appearance of the metallic domains was confirmed at each temperature. Figure 4.4.2(b) shows the temperature-dependent metallic domain size and the number of the metallic domains in the same region. In the narrow temperature range, it was found that the metallic domains appeared discretely and the number of the metallic domains increased with the size of ~500 nm on average in length. Figure 4.4.2 (c) shows the metallic domain size distribution at 336 K. The size of the metallic domain was determined to be 539 ± 159 nm on average in length through Gaussian fitting. These results suggest that the multi-level step-like resistance changes can be observed even in micrometer scale owing to the confined metallic domains.

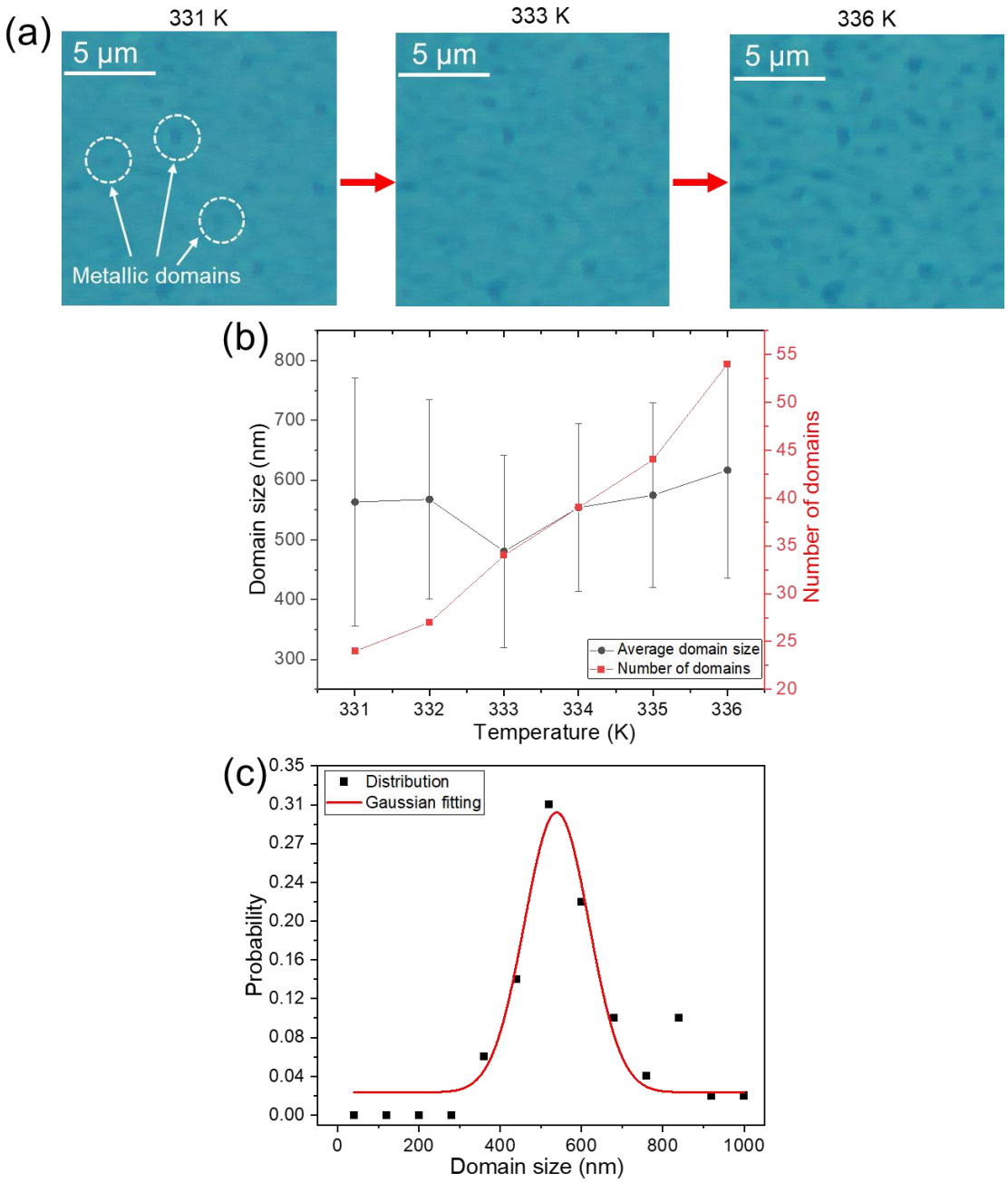

Figure 4.4.2 (a) Magnified temperature-dependent optical microscopy images of the VO_2/hBN flake in the same region. The metallic domains correspond to the dark blue and red dots in the VO_2/hBN flake. The scale bars are 5 μm. (b) Temperature dependence of the size and the number of the metallic domains in the VO_2/hBN flake. (c) Size distribution of the metallic domains at 336 K. The red curve corresponds to Gaussian fitting function.

4.5 Size-dependent MIT property of VO_2/hBN microwire

Figure 4.5.1(a) shows the *R–T* curves measured ten times consecutively for wire (1), exhibiting three orders of magnitude resistivity change at approximately 340 K in each measurement. The observed MIT property is consistent with the result of the increase in the cover ratio of the metallic domains shown in Figure 4.4.1(b). To investigate the size effect, Wire (1) was etched to fabricate wire (2) to reduce the width, as shown in the inset of Fig.4.5.1(b). Figure 4.5.1(b) shows the *R–T* curves measured ten times consecutively for wire (2), exhibiting three orders of magnitude resistivity change at approximately 340 K with different multi-level step-like resistivity changes in each measurement. The electric conduction is governed by the percolation paths [4.13] and when the size of the microwire is equal to several times of the metallic domain size, such multi-level step-like resistance changes appear owing to the confinement effect of the metallic domains [4.14]. Besides, a similar electric behavior was also reported for the *R–T* curves measured eight times consecutively for a VO_2/*r*-Al_2O_3 device [4.15]. Figure 4.5.1(c) shows the schematic of the electric conduction path in the heating process between a pair of electrodes. The possible reason for such electric behavior is the fluctuation of the transition temperature of each metallic domain, leading to different electric conduction paths. However, the magnitude order of the resistivity/resistance change is considerably different. An approximately one order of magnitude resistivity change was observed in wire (2), whereas less than one order of magnitude resistance change has been observed in the VO_2/*r*-Al_2O_3 device [4.15]. This result reflects the difference in the metallic domain size between VO_2 thin films grown on hBN and those grown on Al_2O_3.

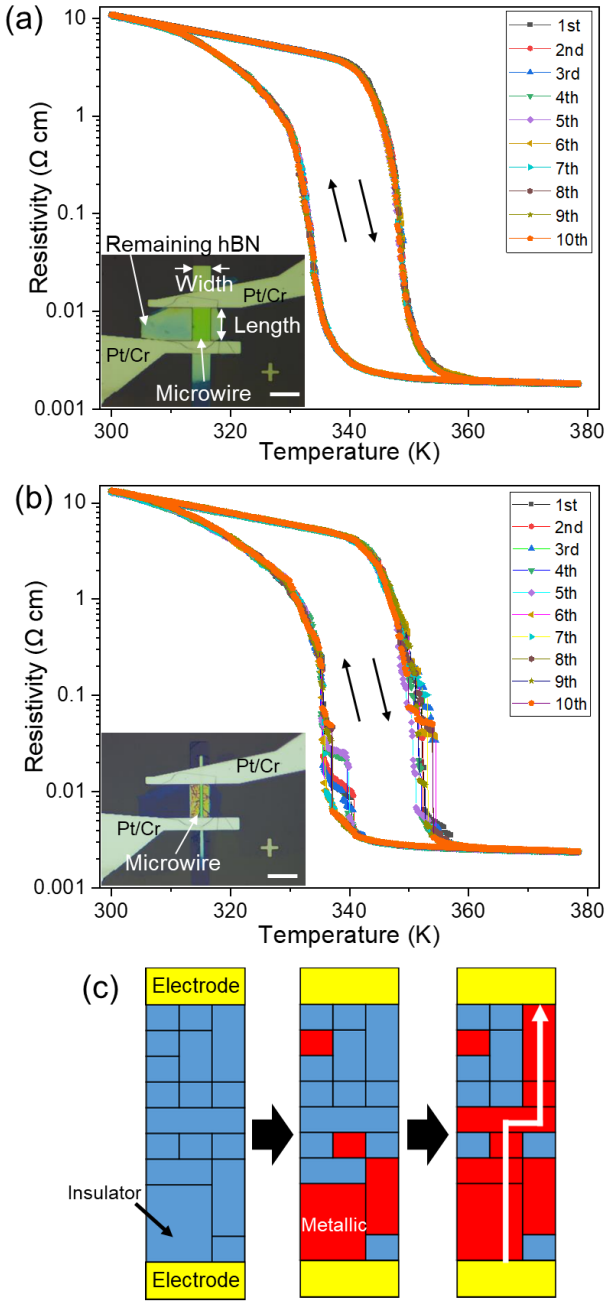

Figure 4.5.1 (a) *R*–*T* curves measured ten times consecutively for wire (1). The inset is the optical microscopy image of wire (1). The thickness of the VO_2 thin film was 52 nm. The red and blue arrows indicate the heating and cooling processes, respectively. The scale bar is 20 μm. (b) *R*–*T* curves measured ten times consecutively for wire (2). The inset indicates the optical microscopy image of wire (2). The scale bar is 20 μm. (c) Schematic of electric conduction path in the heating process between a pair of electrodes. The blue and red areas correspond to the insulator phase and metallic phase, respectively. The white arrow indicates the electric conduction path.

Next, in order to enhance the confinement effect of the metallic domains, wire (3) was prepared as shown in the inset of Fig. 4.5.2 (a). Figure 4.5.2 (a) shows *R–T* curves measured for wire (3). The order of magnitude of the multi-level step-like resistivity changes became more pronounced than that of wire (2) shown in Fig. 4.5.1 (b).

For comparison, a $VO_2/Al_2O_3(0001)$ microwire with L = 2.4 μm and W = 2.3 μm was fabricated (see the inset of Fig. 4.5.2(b)) and *R–T* curves were measured under the same experimental conditions. Figure 4.5.2(b) shows the *R–T* curves of the VO_2/Al_2O_3 microwire and no multi-level step-like resistivity changes were observed despite the comparable device sizes. This reflects the difference in the metallic domain size of VO_2 thin films on Al_2O_3 and hBN. The giant single-step resistivity change changing by two orders of magnitude in wire (3) shown in Fig.4.5.2(a) is an evidence for the effect of the confined metallic domains. Such giant single-step resistivity change is observed when the metallic domain size is comparable to the wire length [4.16, 4.17]. Considering that the length of wire (3) is 1.1 μm, the observed giant single-step resistivity change implies the presence of a metallic domain with the size comparable to 1.1 μm. This is reasonable since the optically determined metallic domain size was up to sub-micrometer scale. Therefore, the giant single-step resistivity change is attributable to the limited number of metallic domains in wire (3). It is also of great importance that such a giant single-step resistivity change was observed even in micrometer scale. These results indicate the applicability of VO_2 thin films to electrical switching devices, such as Mott transistors with the steep and large resistance change in micrometer scale.

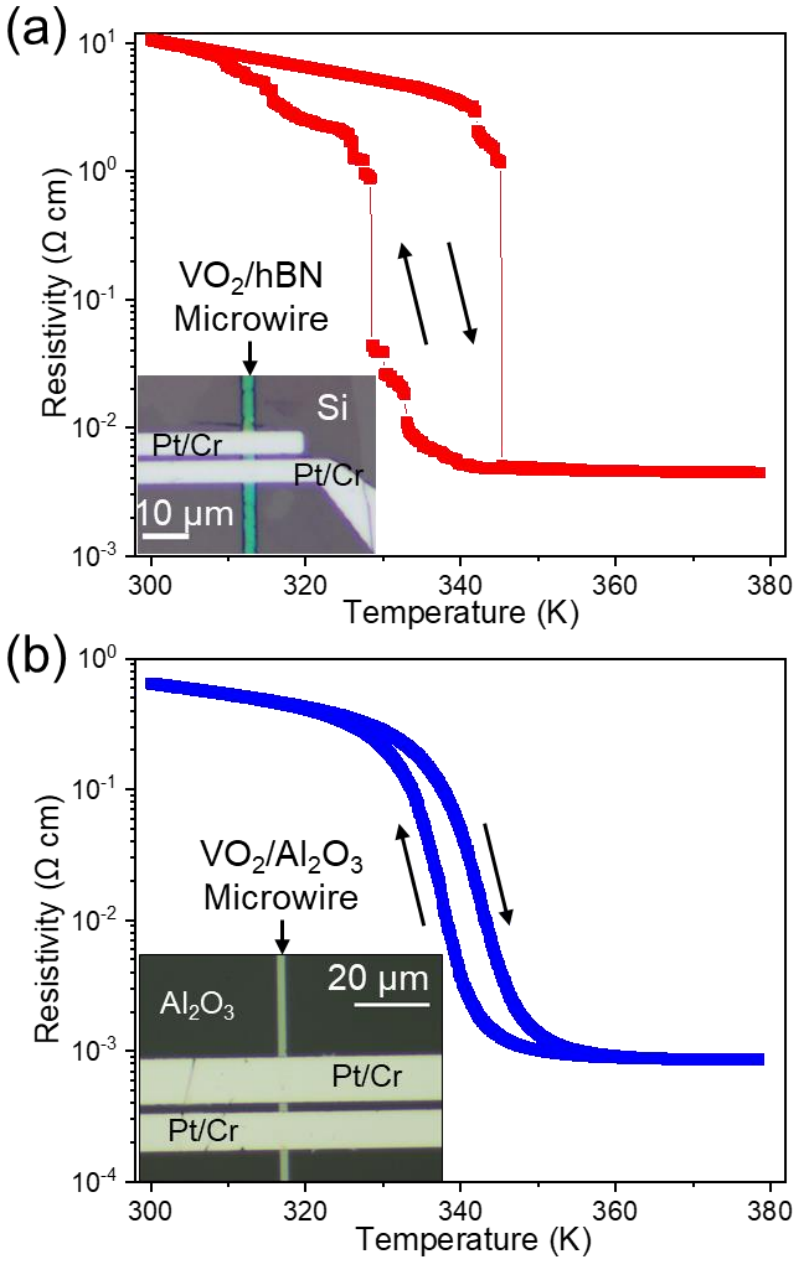

Figure 4.5.2 (a) *R–T* curves of wire (3) showing the giant single-step resistivity change changing by two orders. The inset indicates the optical microscopy image of wire (3). (b) *R–T* curves of the VO_2/Al_2O_3 microwire without multi-level step-like resistance change. The inset indicates the optical microscopy image of the VO_2/Al_2O_3 microwire.

4.6 Conclusion

In conclusion, the metallic domain size of VO_2 thin films grown on hBN is ~500 nm on average in length and up to sub-micrometer scale, as determined by temperature-dependent Raman spectroscopy and *in situ* optical observation. The multi-level step-like resistivity changes is attributable to the confinement effect of the metallic domains in micrometer scale. Importantly, the giant single-step resistivity change changing by two orders was observed, implying the presence of the metallic domain whose size is comparable to 1.1 μm. These results show the usefulness of the application of VO_2/hBN to electrical switching devices with a steep and large resistance change in micrometer scale.

4.7 References

[4.1] M. M. Qazilbash, M. Brehm, B.-G. Chae, P.-C. Ho, G. O. Andreev, B.-J. Kim, S. J. Yun, A. V. Balatsky, M. B. Maple, F. Keilmann, H.-T. Kim, D. N. Basov, Science, **318**, 1750 (2007).

[4.2] M. M. Qazilbash, M. Brehm, G. O. Andreev, A. Frenzel, P.-C. Ho, B.-G. Chae, B.-J. Kim, S. J. Yun, H.-T. Kim, A. V. Balatsky, O. G. Shpyrko, M. B. Maple, F. Keilmann, and D. N. Basov, Phys. Rev. B, **79**, 075107 (2009).

[4.3] H. Takami, T. Kanki, and H. Tanaka, Appl. Phys. Lett., **104**, 023104 (2014).

[4.4] T. Kanki, K. Kawatani, H. Takami, and H. Tanaka, Appl. Phys. Lett., **101**, 243118 (2012).

[4.5] H. Ueda, T. Kanki, and H. Tanaka, Appl. Phys. Lett., **102**, 153106 (2013).

[4.6] K. Kawatani, T. Kanki, and H. Tanaka, Phys. Rev. B, **90**, 054203 (2014).

[4.7] A. Sohn, T. Kanki, K. Sakai, H. Tanaka, and D.-W. Kim, Sci. Rep., **5**, 10417 (2015).

[4.8] A. Sohn, T. Kanki, H. Tanaka, and D.-W. Kim, Appl. Phys. Lett., **107**, 171603 (2015).

[4.9] M. Pan, J. Liu, H. Zhong, S. Wang, Z.-F. Li, X. Chen, and W. Lu, J. Cryst. Growth, **268**, 178 (2004).

[4.10] K. Okimura, N. H. Azhan, T. Hajiri, S.-I. Kimura, M. Zaghrioui, and J. Sakai, J. Appl. Phys., **115**, 153501 (2014).

[4.11] J. H. Parker, Jr., D. W. Feldman, and M. Ashkin, Phys. Rev., **155**, 712 (1967).

[4.12] R. Geick, C. H. Perry, and G. Rupprecht, Phys. Rev., **146**, 543 (1966).

[4.13] J. Rozen, R. Lopez, R. F. Haglund, Jr., and L. C. Feldman, Appl. Phys. Lett., **88**, 081902 (2006).

[4.14] H. Tanaka, H. Takami, T. Kanki, A. N. Hattori, and K. Fujiwara, Jpn. J. Appl. Phys.,

53, 05FA10 (2014).

[4.15] A. Sharoni, J. G. Ramírez, and I. K. Schuller, Phys. Rev. Lett., **101**, 026404 (2008).

[4.16] Y. Tsuji, T. Kanki, Y. Murakami, and H. Tanaka, Appl. Phys. Express, **12**, 025003 (2019).

[4.17] S. Tsubota, A. N. Hattori, T. Nakamura, Y. Azuma, Y. Majima, and H. Tanaka, Appl. Phys. Express, **10**, 115001 (2017).

Chapter 5

Electrical switching using MIT of individual metallic domains in VO_2/hBN

5.1 Introduction

Using the MIT or insulator–metal transition (IMT) property of VO_2 thin films, device application such as Mott transistor [5.1–5.3], bolometer [5.4], smart windows [5.5, 5.6] and so forth has been actively studied through the growth of VO_2 thin films since the resistance/electric current changes can be induced with tiny energy. Particularly, use of Joule heating effect by applying voltage into VO_2 thin films to induce IMT is one of the promising ways to derive the electrical switching property. Thus far, Joule heating effect has been studied through *I–V* characteristics measurements of VO_2 thin films [5.7, 5.8], channels [5.9–5.11], micro/nanowires [5.12, 5.13], and nanonets [5.14] mainly prepared on Al_2O_3 and TiO_2 substrates.

For designing an effective electrical switching device using Joule heating effect, attention should be paid to the creation of metallic domains in the VO_2 channel region. The IMT property of VO_2 thin films is generally governed by the spatial unit elements called “metallic domains”, which appear inhomogeneously during IMT. For instance, the size of the metallic domains in VO_2 thin films on Al_2O_3(0001) substrates are tens of nanometers, which is observed by scanning near-infrared microscope [5.15, 5.16]. Besides, the metallic domain size of VO_2 thin films on TiO_2(001) substrates observed through optical microscopy is ~1 μm [5.17, 5.18]. Thus, steep multi-level step-like resistance changes are observed in VO_2 thin film devices when the device sizes are comparable to individual metallic domains owing to the confinement effect of the metallic domains [5.18–5.20]. Based on these backgrounds, derivation of the utility of metallic domains for device application is attractive for designing electrical switching devices with high performance. For exploration of the effective Joule heating devices using VO_2 thin films, the use of hBN as a growth substrate of VO_2 thin film is promising. As

indicated in Chapter 3, it was discovered that hBN would be a good substrate for growth of VO_2 thin films. In addition, it was revealed that the VO_2 thin films on hBN showed a prominent IMT property and the metallic domains of these VO_2 thin films are observable by means of the optical microscopy, as indicated in Chapter 4. The domain size of the VO_2 thin films on hBN is determined to be ~500 nm on average in length, which is one order of magnitude larger than that of the VO_2 thin films on Al_2O_3(0001) [5.15, 5.16, 5.19, 5.20]. The optically visible metallic domains suggest high accessibility to the individual metallic domains in the VO_2 thin films on hBN and can enhance the presence of the individual metallic domains in device application. Owing to the large-sized metallic domains in VO_2 thin films on hBN, the real space evolution of metallic domains (operando observation) in addition to the *I–V* characteristics measurements can be performed at the same time. This leads to the direct understating a role of domain evolution for electrical functionality.

In this work, two-terminal VO_2/hBN devices were fabricated and the *in situ* observation of the metallic domains evolution was conducted to study the domain dynamics. It was observed that the emergence of the metallic domains and the step-like electric current increases owing to the IMT in the individual metallic domains by applying bias voltage. It was revealed that the electrical switching in the VO_2/hBN device was induced locally with the electric current in the order of micro ampere and individual metallic domains played a role in the electrical switching property through *in situ* optical observation. These findings contribute to the novel creation of electrical switching device using IMT in the individual metallic domains.

5.2 Sample preparation and experiments

For the fabrication of VO_2/hBN devices, hBN flakes were mechanically exfoliated from a single-crystal bulk hBN and transferred onto SiO_2/Si substrates using the Scotch tape. Oxygen annealing was conducted for the hBN flakes on SiO_2/Si substrates at 773 K for 3.5 hours to remove adhesive residue. VO_2 thin films were prepared on hBN by pulsed lased deposition under the partial oxygen pressure of 0.95 Pa and the substrate temperature of 723 K using a sintered V_2O_5 as a target and an ArF excimer laser (λ = 193 nm). The laser frequency was 2 Hz. The thickness of the VO_2 thin films was ~50 nm. The stacks of VO_2/hBN were transferred onto a SiO_2/Si substrate using transparent polymer (PF Gel-Film, Gel-Pak) after exposing polymer to water vapor. Next, a pair of electrodes composed of Pt (80 nm) and Cr (5 nm) were deposited onto the transferred VO_2/hBN stacks for the electrical transport measurements.

Figure 5.2.1 shows an optical microscopy image of a VO_2/hBN device with Pt/Cr electrodes. The electrode width was 5.8 μm and the electrode gap distance was 2.3 μm. Hereafter, the VO_2 region is defined as that surrounded between the electrodes in the VO_2/hBN device for simplicity. To investigate the IMT property in the VO_2/hBN device, the temperature-dependent electric transport property was measured using a variable temperature Peltier stage and a source meter (2634B, Keithley). The resistance–temperature (*R–T*) curves were obtained under a ramp/cooling rate of 6.0 K/min and at 0.2 K step. For the *in situ* optical observation of the electrical switching in the VO_2/hBN device, an electrical source measurement unit (SMU: B2901, Keysight) and an optical microscope (BX51M, Olympus) were used. The bias voltage were applied up to 4.00 V at 20 mV step at room temperature, while the applied duration was set to be 1 sec.

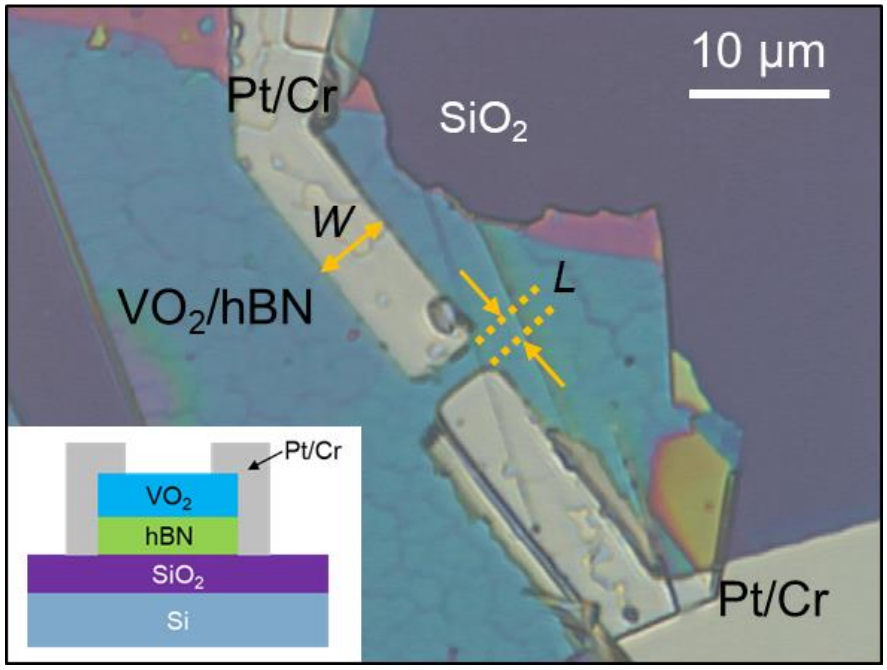

Figure 5.2.1 Optical microscopy image of a representative VO_2/hBN sample on SiO_2/Si substrate with a pair of Pt/Cr electrodes. The inset indicates the schematic of the VO_2/hBN sample.

Figure 5.2.2 shows the *R*–*T* curve of the VO_2/hBN device. The VO_2/hBN device exhibited a resistance change of three orders of magnitude at the transition temperature of ~340 K. Importantly, significant multi-level step-like resistance changes were observed in the *R*–*T* curve in Fig. 5.2.2. The clear step-like resistance changes indicate the confined domain structures in the VO_2 region between the electrodes in the micrometer size.

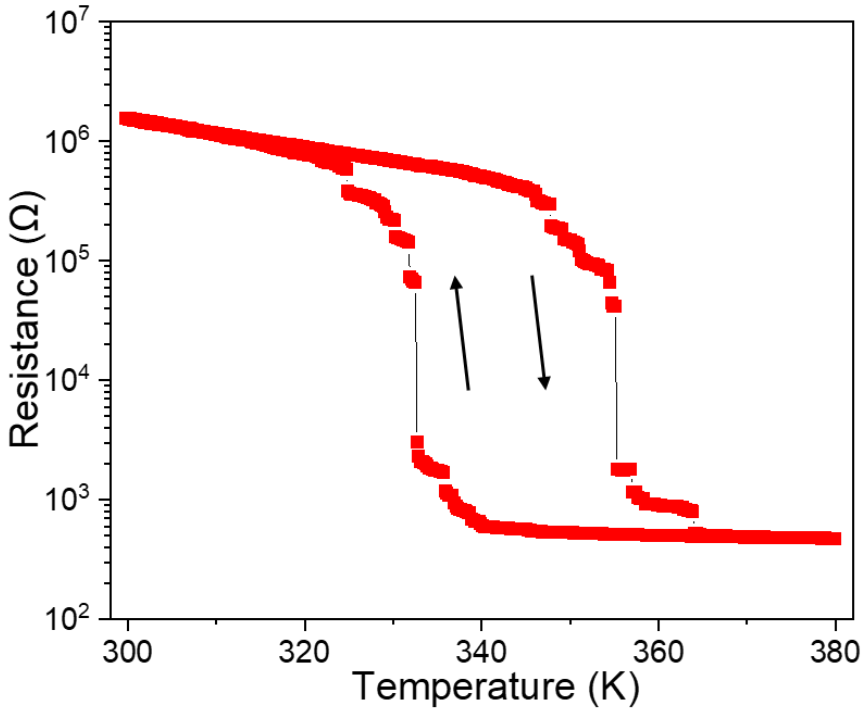

Figure 5.2.2 *R*–*T* curve of VO_2/hBN sample with L = 2.3 μm and W = 5.8 μm.

To evaluate the metallic domain contribution to the IMT property, the temperature-dependent optical microscopy observation of the VO_2/hBN sample in the heating process was conducted. Figures 5.2.3(a)–(c) show the optical microscopy images of the VO_2/hBN sample at 300, 350, and 360 K, respectively, during the heating without any bias voltage application. Note that a black dot between the electrodes in Fig. 5.2.3(a) was formed due to the contamination and not related to IMT. The color change of VO_2 with the increase in temperature shows the generation of metallic domains in the insulating VO_2, which reflects the evolution of IMT in VO_2. The light blue region at 300 K (Fig. 5.2.3(a)) corresponds to the insulating phase of VO_2 (VO_2 (i)). At 360 K, where VO_2 was almost completely transitioned to metallic, the color of VO_2 was red-purple, as shown in Fig. 5.2.3(c). The color change of VO_2 from light blue to red-purple can be explained by the

optical property change through IMT. At the intermediate temperature of 350 K, the generation of metallic domains (VO_2 (m)) in VO_2 (i) was clearly observed. In Fig. 5.2.3(b), the size of VO_2 (m) was on the several hundred nanometers to sub-micrometer scale, which is consistent with the metallic domain size in VO_2 thin film/hBN. The coincidence between the resistance change (Fig. 5.2.2) and the creation of metallic domains (Fig. 5.2.3(c)) confirms that the multiple step resistance change in Fig. 5.2.2 was caused by the generation of metallic VO_2 domains.

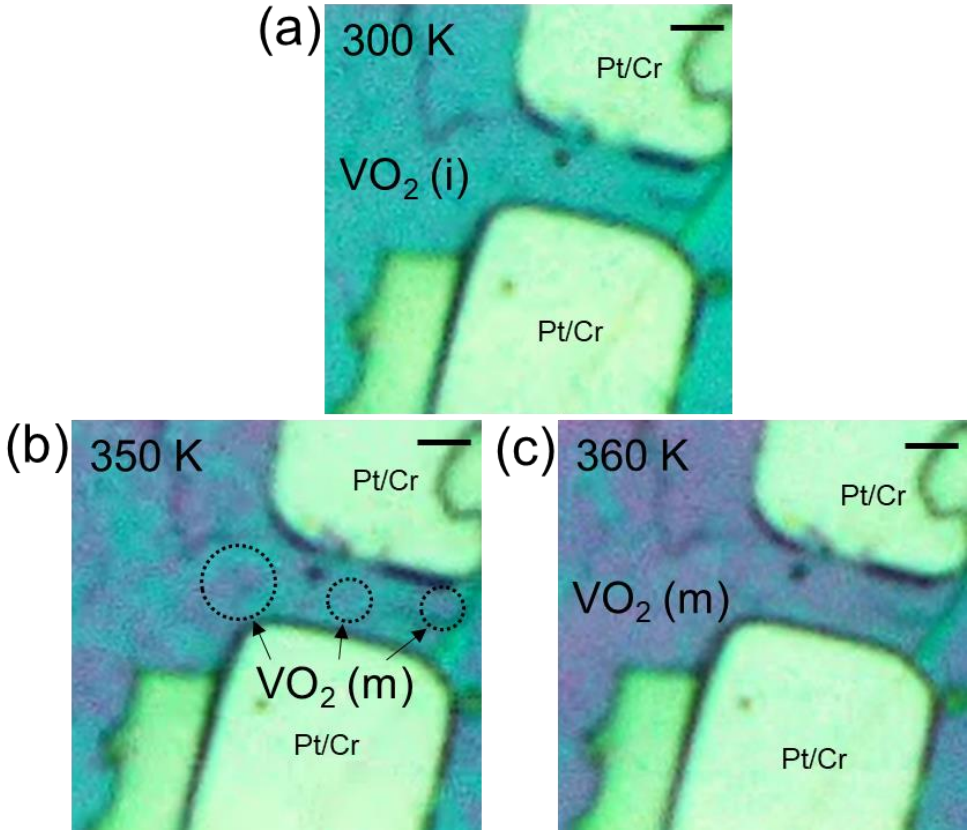

Fig. 5.2.3 Optical microscopy images of VO_2 region without applying bias voltage at (a) 300, (b) 350, and (c) 360 K in the heating process. The light blue region in (a) is the insulating phase of VO_2 (VO_2 (i)). At 350 K in (b), the red-purple regions surrounded by the dotted circles emerged partially corresponding to the metallic domains of VO_2 (VO_2 (m)). At 360 K in (c), almost the entire area changed to VO_2 (m). The scale bars are 2 μm.

5.3 Electrical switching property of VO_2/hBN sample

Next, to utilize the confined structure for device demonstration, bias voltage was applied for insulating VO_2 while monitoring the electric current and microstructure. Figure 5.3.1(a) shows the *I*–*V* characteristics of the VO_2/hBN sample at room temperature with the bias voltage increasing from $V = 0$ V to $V = 4.90$ V. Initially, the electric current monotonically increased below $V = 2.70$ V, and a sharp increase was observed at around $V = 3.40$ V. Then, the electric current dropped sharply at around $V = 3.52$ V, and again the electric current increased with the bias voltage. The abnormal electric current increase deviating from the ohmic behavior shown in Fig. 5.3.1(a) is considered to originate from the IMT of VO_2 because of the Joule heating effect upon applying bias voltage [5.7, 5.8]. Typically, the step increases in the electric current highlighted with black arrows in Fig. 5.3.1(b) should be caused by the metallic domain generation in the VO_2 region.

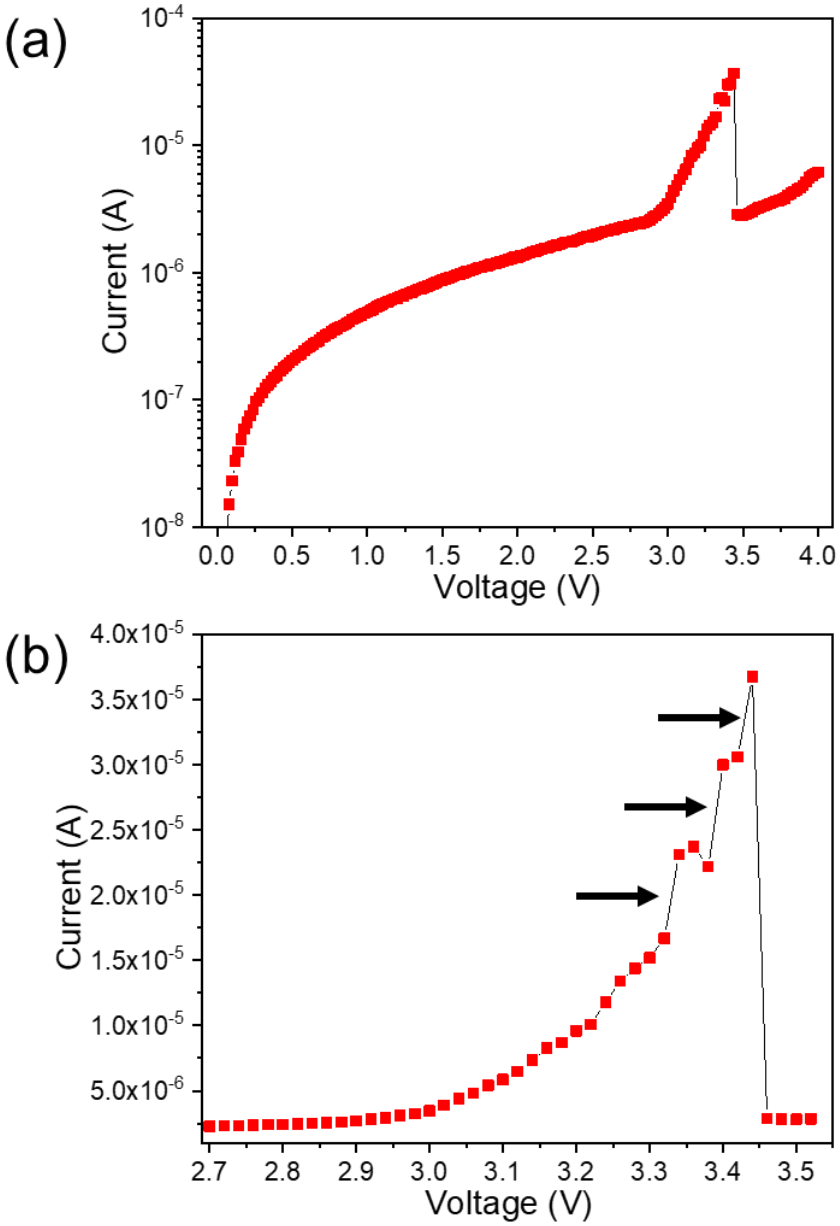

Fig. 5.3.1 (a) *I–V* characteristics of VO_2/hBN sample at room temperature. (b) Magnification of *I–V* characteristics around V = 3 V. The step current increases are indicated with black arrows.

Figures 5.3.2(a)–(c) show optical microscopy images at $V = 0$ V, $V = 3.52$ V, and $V = 3.76$ V, respectively, of the same VO_2/hBN sample showing prominent step resistance changes in Fig. 5.2.2. At $V = 0$ V (Fig. 5.3.2(a)), the entire region showed the light blue color corresponding to VO_2 (i). On the other hand, the color of the VO_2 region partially changed from light blue to red-purple at $V = 3.52$ V (Fig. 5.3.2(b)), indicating the emergence of metallic domains (VO_2 (m)). The size of the region with the color change was several hundred nanometers, which is consistent with the metallic domain size in heater-controlled IMT (Fig. 5.3.2(b)). In addition, the black region was formed at $V = 3.52$ V where the electric current sharply decreased. The simultaneous appearance of the black region and the electric current decrease indicates that a break in the electric path in VO_2, namely, VO_2 was partially degraded to become insulating. Moreover, under the additional application of bias voltage at $V = 3.76$ V (Fig. 5.3.2(c)), the red-purple region was observed clearly. Note that the degraded VO_2 region didn't return to the initial state after stopping application of the bias voltage. Since the emergence of metallic domains was synchronized with the step increase in electric current in the VO_2/hBN sample, the electric current increased reflects IMT in the individual domains, i.e., the emergence of metallic domains under bias voltage application.

Considering the locally induced IMT, i.e., the emergence of metallic domains in the VO_2/hBN sample, the electric current is expected to flow predominantly through several metallic domains induced by the applied bias voltage, where the IMT can be induced by Joule heating. This is expected to be the origin of the step electrical switching in Fig. 5.3.1(b). The concentration of the electric current led to the excess Joule heat, which resulted in the partial degradation of the VO_2 region. The size of the degraded region: ~500 nm, which is comparable to that of a single domain or a few domains, also supports

this assumption. These results confirm the inhomogeneous phenomenon in IMT in VO_2, leading to the selective local electrical switching and open a path to the creation of electrically effective switching devices with the Joule heating effect under domain confinement effect, and indicate the applicability of single metallic domains of VO_2 thin films on hBN.

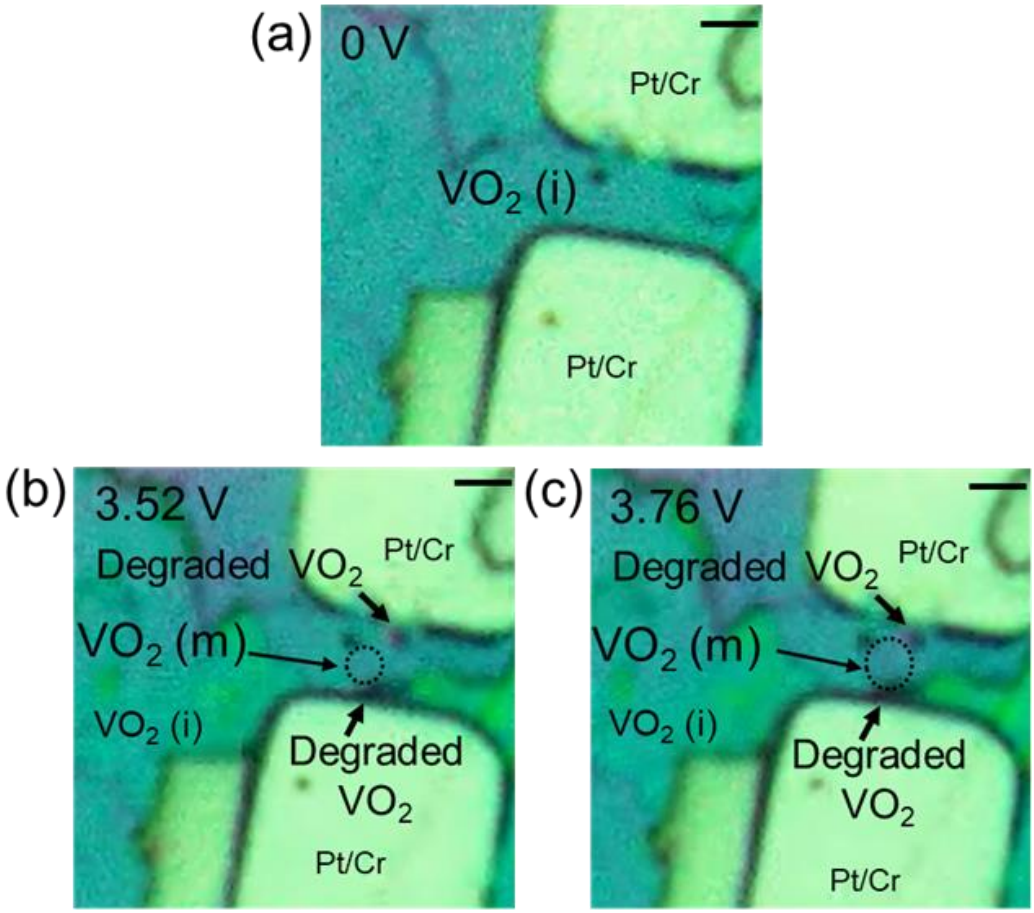

Fig. 5.3.2 Optical microscopy images in the same VO_2 regions as in Figs. 4(a)–4(c) at (a) $V = 0$ V, (b) $V = 3.52$ V, and (c) $V = 3.76$ V at room temperature. The light blue regions in (a)–(c) are the insulating phase of VO_2 (i). In the dotted area in (b) and (c), the red-purple regions corresponding to the metallic domains ((VO_2 (m)) appeared. The black regions in (b) and (c) indicate the degraded VO_2 regions. The scale bars are 2 μm.

5.4 Conclusion

The electrical switching property of the VO_2/hBN device was measured by inducing IMT through Joule heating effect and the emergence of the metallic domains was observed simultaneously at room temperature. Step electric current changes were observed corresponding to the appearance of the metallic domains through the optical microscopy images, which indicates that the individual metallic domains play a major role in the electrical switching property. In this electrical switching accompanied with IMT, the local concentration of the electric current flow is considered to happen. Importantly, it was revealed that the utility of the IMT in the individual domains was demonstrated in the VO_2/hBN. These findings can contribute to domain engineering and enhance the applicability of VO_2 thin films on hBN.

5.5 References

[5.1] S. Sengupta, K. Wang, K. Liu, A. K. Bhat, S. Dhara, J. Wu, and M. M. Deshmukh, Appl. Phys. Lett., **99**, 062114 (2011).

[5.2] H.-T. Kim, B.-G. Chae, D.-H. Youn, S.-L. Maeng, G. Kim, K.-Y. Kang, and Y.-S. Lim, New J. Phys., **6**, 52 (2004).

[5.3] T. Yajima, T. Nishimura, and A. Toriumi, Nat. Commun., **6**, 10104 (2015).

[5.4] C. Chen, X. Yi, X. Zhao, and B. Xiong, Sens. Actuators, A, **90**, 212 (2001).

[5.5] Z. Huang, S. Chen, C. Lv, Y. Huang, and J. Lai, Appl. Phys. Lett., **101**, 191905 (2012).

[5.6] R. Basu, P. Magudapathy, M. Sardar, R. Pandian, and S. Dhara, J. Phy. D: Appl. Phy., **50**, 465602 (2017).

[5.7] A. Rana, C. Li, G. Koster, and H. Hilgenkamp, Sci. Rep., **10**, 3293 (2020).

[5.8] J. Lappalainen, S. Heinilehto, H. Jantunen, and V. Lantto, J. Electroceram., **22**, 73 (2009).

[5.9] D. Li, A. A. Sharma, D. K. Gala, N. Shukla, H. Paik, S. Datta, D. G. Schlom, J. A. Bain, and M. Skowronski, ACS Appl. Mater. Interfaces, **8**, 12908 (2016).

[5.10] O. Murtagh, B. Walls, and I. V. Shvets, Appl. Phys. Lett., **117**, 063501 (2020).

[5.11] A. Crunteanu, J. Givernaud, J. Leroy, D. Mardivirin, C. Champeaux, J.-C. Orlianges, A. Catherinot, and P. Blondy, Sci. Technol. Adv. Mater., **11**, 065002 (2010).

[5.12] B.-G. Chae, H.-T. Kim, D.-H. Youn, and K.-Y. Kang, Physica B, **369**, 76 (2005).

[5.13] S.-H. Bae, S. Lee, H. Koo, L. Lin, B. H. Jo, C. Park, and Z. L. Wang, Adv. Mater., **25**, 5098 (2013).

[5.14] J. Zhang, Z. Zhao, J. Li, H. Jin, F. Rehman, P. Chen, Y. Jiang, C. Chen, M. Cao, and Y. Zhao, ACS Appl. Mater. Interfaces, **9**, 27135 (2017).

[5.15] M. M. Qazilbash, M. Brehm, B.-G. Chae, P.-C. Ho, G. O. Andreev, B.-J. Kim, S. J. Yun, A. V. Balatsky, M. B. Maple, F. Keilmann, H.-T. Kim, D. N. Basov, Science, **318**, 1750 (2007).

[5.16] M. M. Qazilbash, M. Brehm, G. O. Andreev, A. Frenzel, P.-C. Ho, B.-G. Chae, B.-J. Kim, S. J. Yun, H.-T. Kim, A. V. Balatsky, O. G. Shpyrko, M. B. Maple, F. Keilmann, and D. N. Basov, Phys. Rev. B, **79**, 075107 (2009).

[5.17] K. Kawatani, H. Takami, T. Kanki, and H. Tanaka, Appl. Phys. Lett., **100**, 173112 (2012).

[5.18] H. Ueda, T. Kanki, and H. Tanaka, Appl. Phys. Lett., **102**, 153106 (2013).

[5.19] H. Takami, T. Kanki, and H. Tanaka, Appl. Phys. Lett., **104**, 023104 (2014).

[5.20] A. N. Hattori, A. I. Osaka, K. Hattori, Y. Naitoh, H. Shima, H. Akinaga, and H. Tanaka, Crystals, **10**, 631 (2020).

Chapter 6

Application of hBN as a universal substrate for various transition metal oxide thin films

6.1 Introduction

Based on the results reported in chapters 3 and 4, hBN indicates the possibility as a universal substrate to grow transition metal oxide thin films regardless of the lattice mismatch at the interface between thin films and substrates. Therefore, the growth of other thin film materials, which has different lattice structure and lattice constants from those of VO_2, can demonstrate the functionality of hBN as a universal thin film growth substrate. Here, I focused on the growth of Fe_3O_4 and $NdNiO_3$ thin films on hBN and characterized their crystallinity and MIT properties.

Fe_3O_4 is a cubic-structured half-metallic material with the lattice constant of 8.39 Å showing MIT, which is called Verwey transition accompanied with a resistance/magnetization change of 1-several orders of magnitude [6.1–6.4]. In a bulk single crystal, the transition temperature is approximately 110 K [6.2]. Fe_3O_4 has attractive material properties in addition to MIT, namely, high Curie temperature of 850 K and high spin polarization at Fermi level [6.5]. Therefore, growth of Fe_3O_4 thin films for electronics and spintronics devices have been actively studied [6.6–6.10]. Thus far, in order to obtain high-quality thin films of Fe_3O_4, stiff single-crystal MgO substrates have been commonly utilized because single-crystal epitaxial Fe_3O_4 thin films can be obtained on MgO, whose lattice constant is 4.21 Å [6.11–6.13]. As a flexible substrate, mica has been reported to be used to grow Fe_3O_4 thin films [6.14, 6.15]. However, mica is reported to be negatively charged and relatively fragile [6.16]. In addition, especially for flexible device application in spintronics devices, Fe_3O_4 nanoparticles have been grown on two-dimensional layered materials, such as MoS_2 and graphene [6.17–6.20]. However, the clear resistance/magnetization changes owing to Verwey transition has yet to be demonstrated.

$NdNiO_3$ is a perovskite transition metal oxide material with lattice structures of orthorhombic in bulk crystals and pseudocubic in thin films exhibiting MIT around 190 K in a bulk single crystal [6.21–6.23]. With the use of MIT in $NdNiO_3$ thin films, application to electrical switching devices [6.24] and memory devices using proton doping [6.25–6.27] has been reported for realization of low-energy electrical switching. Single-crystal $NdNiO_3$ thin films have been prepared mainly on the single-crystal oxide substrates with perovskite lattice structures, such as $LaAlO_3$, $SrTiO_3$, $NdGaO_3$, $KTiO_3$ and so forth [6.28–6.31] since the interfacial lattice matching is important. Therefore, these two materials are expected to be the suitable to demonstrate the universality of hBN as a growth substrate with flexibility and transferability. In this chapter, the growth of Fe_3O_4 and $NdNiO_3$ thin films were grown on hBN and the properties of the thin films were characterized, similarly to VO_2 thin films grown on hBN.

6.2 Growth and characterization of Fe_3O_4 thin films on hBN

Figure 6.2.1 shows the schematic of the device fabrication flow of Fe_3O_4/hBN microwires with electrodes. HBN single crystal flakes were prepared by exfoliation of bulk single crystals of hBN using Scotch tapes. The flakes were transferred onto MgO(001) substrates. The Fe_3O_4 thin films were grown by PLD under the partial oxygen pressure of 1.0×10^{-4} Pa and the substrate temperature of 633 K. The thicknesses of the Fe_3O_4 thin films was controlled by the deposition time since they had a proportional relationship. The growth of Fe_3O_4 thin films was confirmed and the lattice structure was characterized using laser Raman spectroscopy, AFM, and TEM. Next, Fe_3O_4/hBN microwires were fabricated using photolithography and Ar-ion milling. Since a clear resistance change owing to the Verwey transition was observed in Fe_3O_4 nanowires

fabricated by the moderate Ar-ion etching [6.32], no vital damage was introduced into the Fe_3O_4 thin films on hBN by the etching process. For electric transport measurements to characterize the MIT property, two-terminal electrodes composed of Pt (65 nm) and Cr (5 nm) were deposited using photolithography and sputtering deposition.

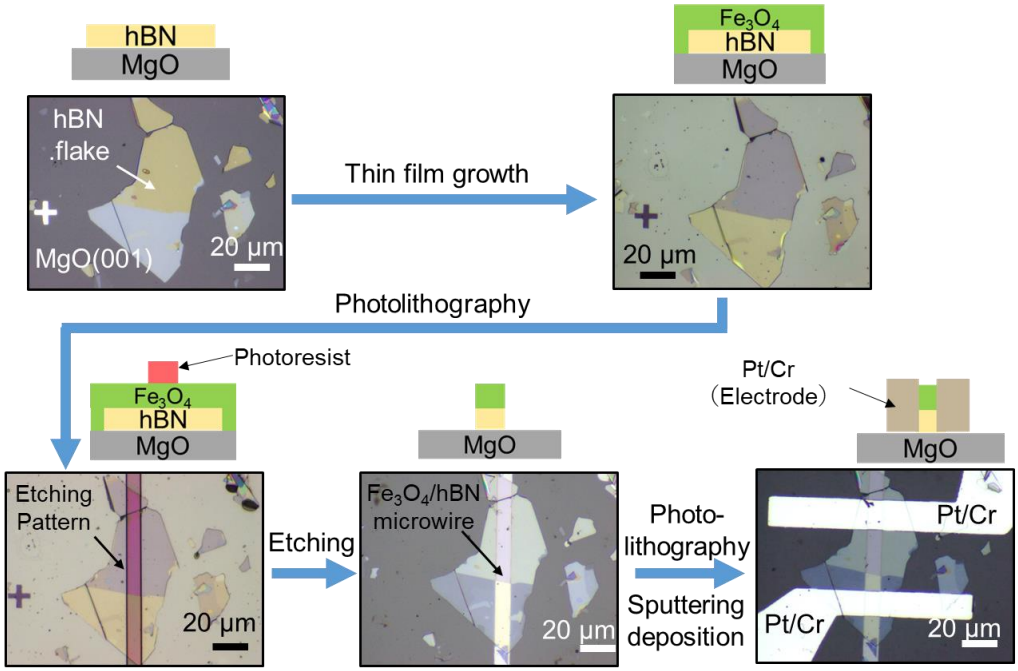

Fig. 6.2.1 Schematic of the device fabrication process flow, including exfoliation of hBN flakes, PLD, etching, and electrode deposition.

Figure 6.2.2(a) shows the optical microscopy image of the Fe_3O_4/hBN stacks on the MgO substrate. It was confirmed that the thin film was formed homogeneously. Figure 6.2.2(b) shows the Raman spectrum of the Fe_3O_4 thin film on hBN at room temperature. Clear Raman peaks observed at 307 cm^{-1}, 537 cm^{-1}, and 665 cm^{-1} were attributable to Raman active A_{1g}, $T_{2g}(2)$, and $T_{2g}(3)$ modes of Fe_3O_4 [6.33, 6.34] in addition to the peak at 1367 cm^{-1} of hBN [6.35], confirming the successful formation of the Fe_3O_4 thin films on hBN.

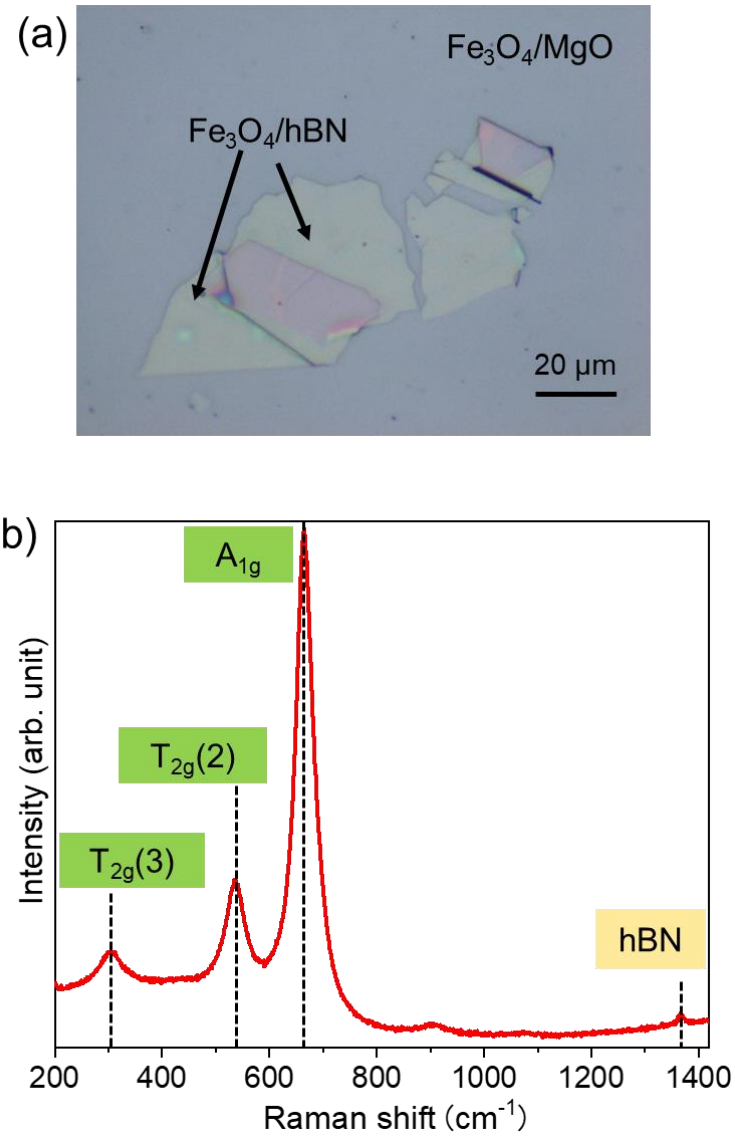

Figure 6.2.2 (a) Optical microscopy image of Fe_3O_4/hBN stacks on MgO substrate. (b) Raman spectrum of the Fe_3O_4 thin film on hBN at room temperature.

Figure 6.2.3(a) shows the surface morphology of the 200-nm thick Fe_3O_4 thin film on hBN obtained by AFM. It was discovered that the surface of the Fe_3O_4 thin film is composed of grain structures. The grain size distribution is shown in Fig. 6.2.3(b). The grain size was estimated to be 33 ± 7 nm by fitting a logarithmic-normal function.

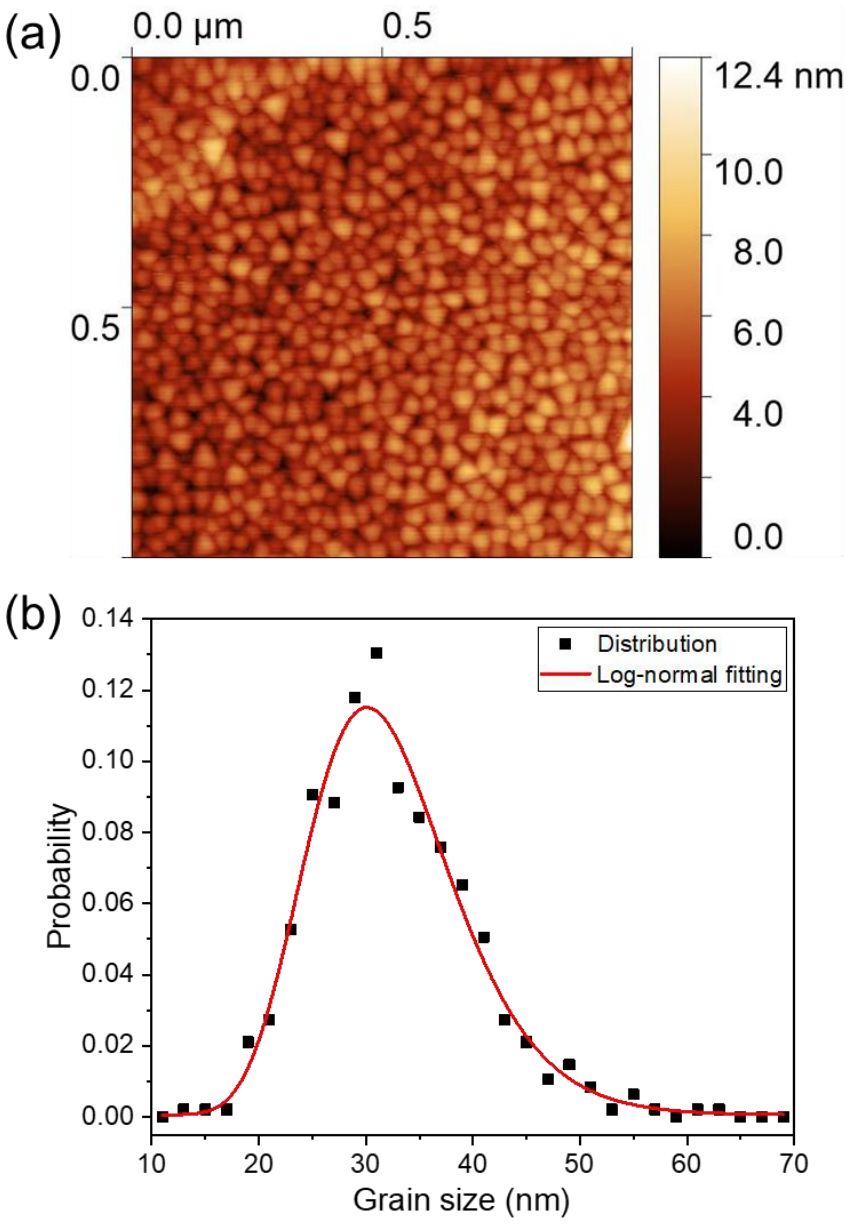

Figure 6.2.3 (a) AFM image of Fe_3O_4 thin films on hBN. (b) The grain size distribution (black plots) and the logarithmic-normal fitting function (red curve).

The cross-sectional TEM image of the Fe_3O_4/hBN stack is shown in Fig. 6.2.4(a). Atomic-scale hBN and Fe_3O_4 lattices were clearly observed at the bottom and the top of the image, respectively. Figure 6.2.4(b) shows the FFT image of the Fe_3O_4 region surrounded by the red square. It was revealed that the certain periodicities of the Fe_3O_4 lattice correspond to reflections of 111 Fe_3O_4, $2\bar{1}\bar{1}$ Fe_3O_4, and so on. These reflections indicate that the crystal relationship between Fe_3O_4 and hBN satisfies $Fe_3O_4(111)$ // hBN(001). Generally, Fe_3O_4 grows epitaxially on MgO(001) with the $Fe_3O_4(001)$ [100] || MgO(001) [100] orientation relation, which reflects the lattice parameters of Fe_3O_4 (a = 8.397 Å) and MgO (a = 4.212 Å).

Generally, the growth orientation is strongly influenced by the lattice mismatch and the connection force at the interface when the thin film is grown on single-crystal oxide substrates because of the strong ionic/covalent connection force. Using the same estimation of lattice mismatch as that in Chapter 3.4, the total lattice mismatch between $Fe_3O_4(111)$ and hBN(001) is 5%. It is interesting that the growth of Fe_3O_4 thin films was realized despite the existence of large lattice mismatch. It is notable that the shape of $Fe_3O_4(111)$ is equilateral triangle, which has a high symmetry with hexagonal lattice structure of hBN. This implies the geometrical restriction on growth of thin films on hBN, while the lattice match at the interface is ignorable.

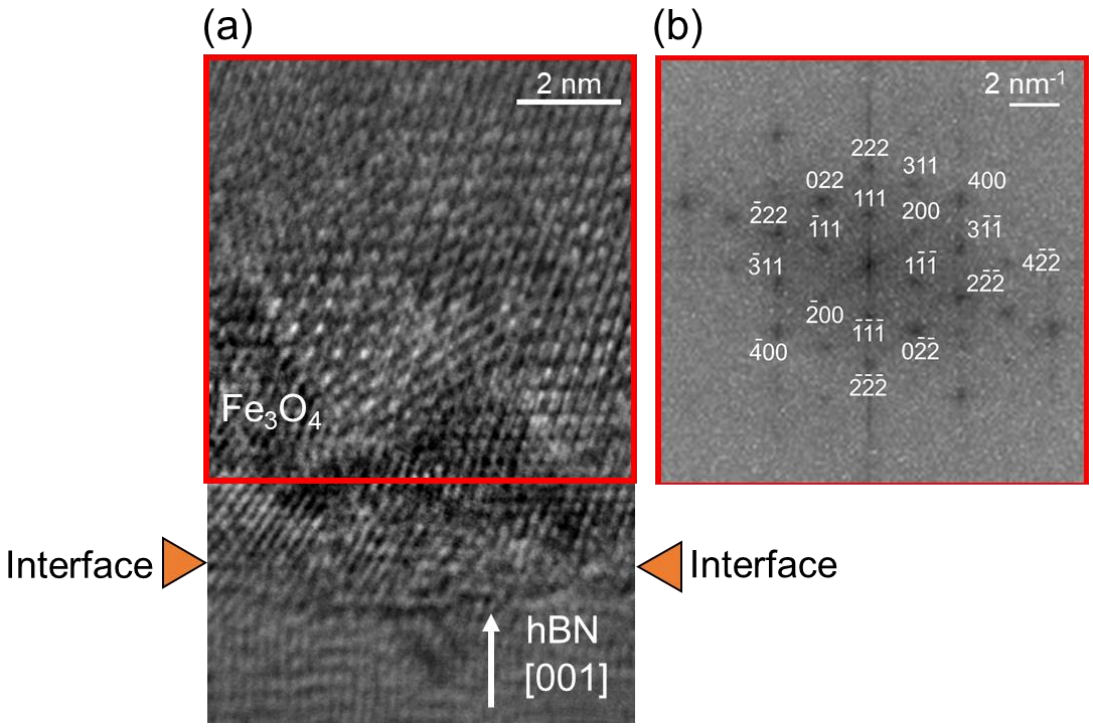

Figure 6.2.4 (a) Cross-sectional TEM image of the interface, indicated by the orange arrows, between the Fe_3O_4 thin film and the hBN flake. (b) The FFT image of Fe_3O_4 in the red square area in Fig. (a).

The structural transition accompanies Verwey transition. The temperature dependence of the Raman peak shift in the A_{1g} mode was examined since the A_{1g} mode is more sensitive to the cubic-orthorhombic structural transition in Fe_3O_4 than T_{2g} modes. The Raman shift in the peak position of the A_{1g} mode (approximately −4 cm^{-1}) has been reported to be larger than that of T_{2g} modes (approximately −2 cm^{-1}) in single crystals of Fe_3O_4 at approximately 110 K in the heating process [6.34]. Figure 6.2.5(a) shows the temperature-dependent normalized Raman peaks of the A_{1g} mode with increasing temperature from 90 to 140 K. It was observed that the peak position shifted toward smaller values in the heating process.

As shown in Figure 6.2.5(b), the peak position was observed to shift by −5 cm^{-1}

from 90 to 140 K. In the measurement range, the peak position shifted by −1.4 cm^{-1} at maximum from 105 to 110 K. This shift in the peak position is larger by one order than that owing to thermal expansion of Fe_3O_4 (thermal expansion coefficient of A_{1g} mode: 0.023 cm^{-1}/K) [6.36], implying that the Fe_3O_4 thin film on hBN underwent Verwey transition.

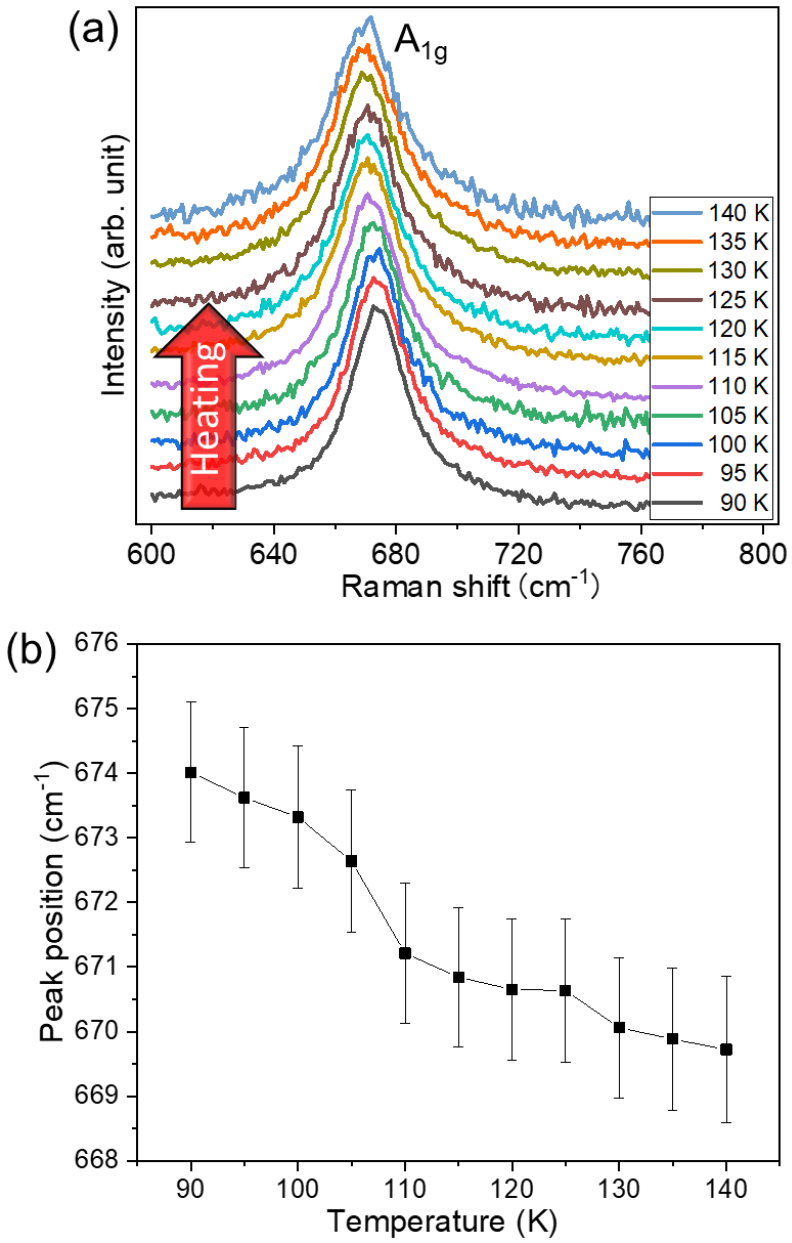

Figure 6.2.5 Temperature dependence of normalized Raman spectra of A_{1g} mode in the Fe_3O_4 thin film grown on hBN within the temperature range of 90 to 140 K in the heating process. (b) Temperature dependence of the peak position of A_{1g} mode.

The temperature-dependent electric transport properties (*R–T* curves) of Fe_3O_4/hBN microwires are shown in Fig. 6.2.6(a). The thicknesses of the Fe_3O_4 microwires were 35, 100, and 170 nm. These three samples exhibited Verwey transition at around 110–120 K. The transition temperature was defined as the point of inflection in the first derivative of logρ (Ω cm) as a function of temperature. The transition temperature of the samples with the thicknesses of Fe_3O_4 of 100 nm and 170 nm was ~115 K, whereas the transition temperature of the 35-nm-thick sample was 111 K.

Figure 6.2.6(b) shows the Fe_3O_4 thin film thickness dependence of the transition temperature and the maximum absolute value of the resistivity change ratio, which corresponds to the steepness of the *R–T* curves from 35 to 240 nm. Interestingly, the transition temperature was independent of the Fe_3O_4 thickness on hBN although it is very sensitive to film thickness for epitaxial Fe_3O_4 films grown on MgO(001) [6.3, 6.4]. The steady Verwey transition properties regardless of the Fe_3O_4 thickness on hBN mean that the Verwey transition property of the Fe_3O_4 thin film is homogeneous in the depth direction, i.e., [111] direction because of the week interaction between Fe_3O_4 film and hBN at the interface. Namely, van der Waals interactions lead to the thickness independence of the Verwey transition property. Therefore, Fe_3O_4 thin films on hBN exhibited Verwey transition regardless of the Fe_3O_4 thickness.

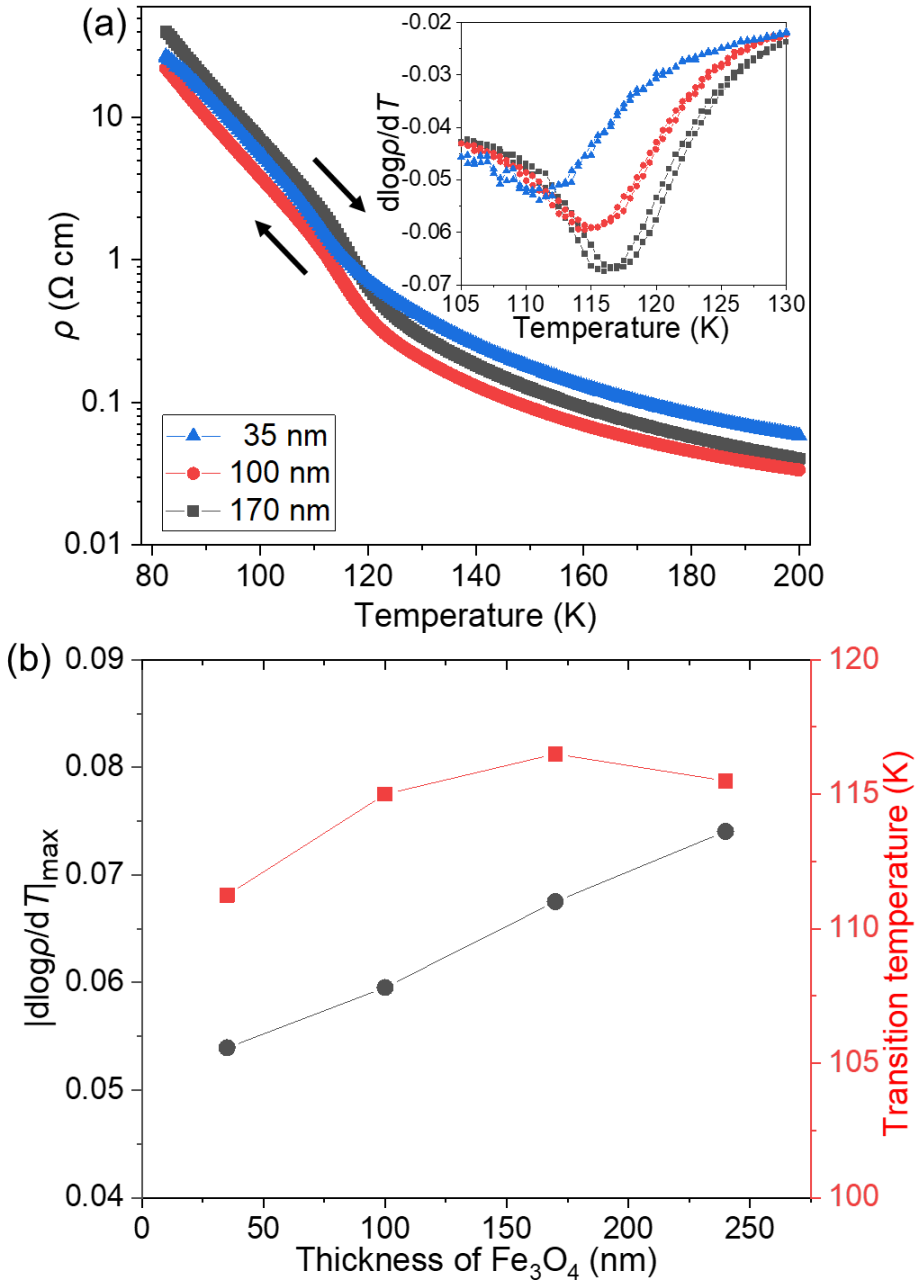

Figure 6.2.6 (a) Electric transport property of Fe_3O_4/hBN microwires in different thicknesses of Fe_3O_4 thin films. The inset indicates the first derivative of the resistivity change as a function of temperature. (b) Thickness dependence of Fe_3O_4 of the resistance change ratio and the transition temperature

The transfer of the Fe_3O_4/hBN stack from one substrate to another was demonstrated for application to transferable devices following the transfer method indicated in Chapter 2.3. Figure 6.2.7(a) shows the optical microscopy image of the Fe_3O_4/hBN stack transferred from a MgO substrate onto a SiO_2/Si substrate after the deposition of Pt/Cr electrodes. The electric transport property of the Fe_3O_4/hBN stack is shown in Fig. 6.2.7(b). The transferred Fe_3O_4 film exhibited clear Verwey transition. The transition temperature of the Fe_3O_4/hBN stack was 115 K, which is same as that of as-grown Fe_3O_4/hBN microwires. The steepness of the *R–T* curves was maintained through the transfer process. Moreover, no serious damage such as formation of cracks or wrinkles on the surface of the transferred Fe_3O_4/hBN stack found from the optical microscopy image. The maintained Verwey transition property indicates the utility of the transferable Fe_3O_4/hBN stack.

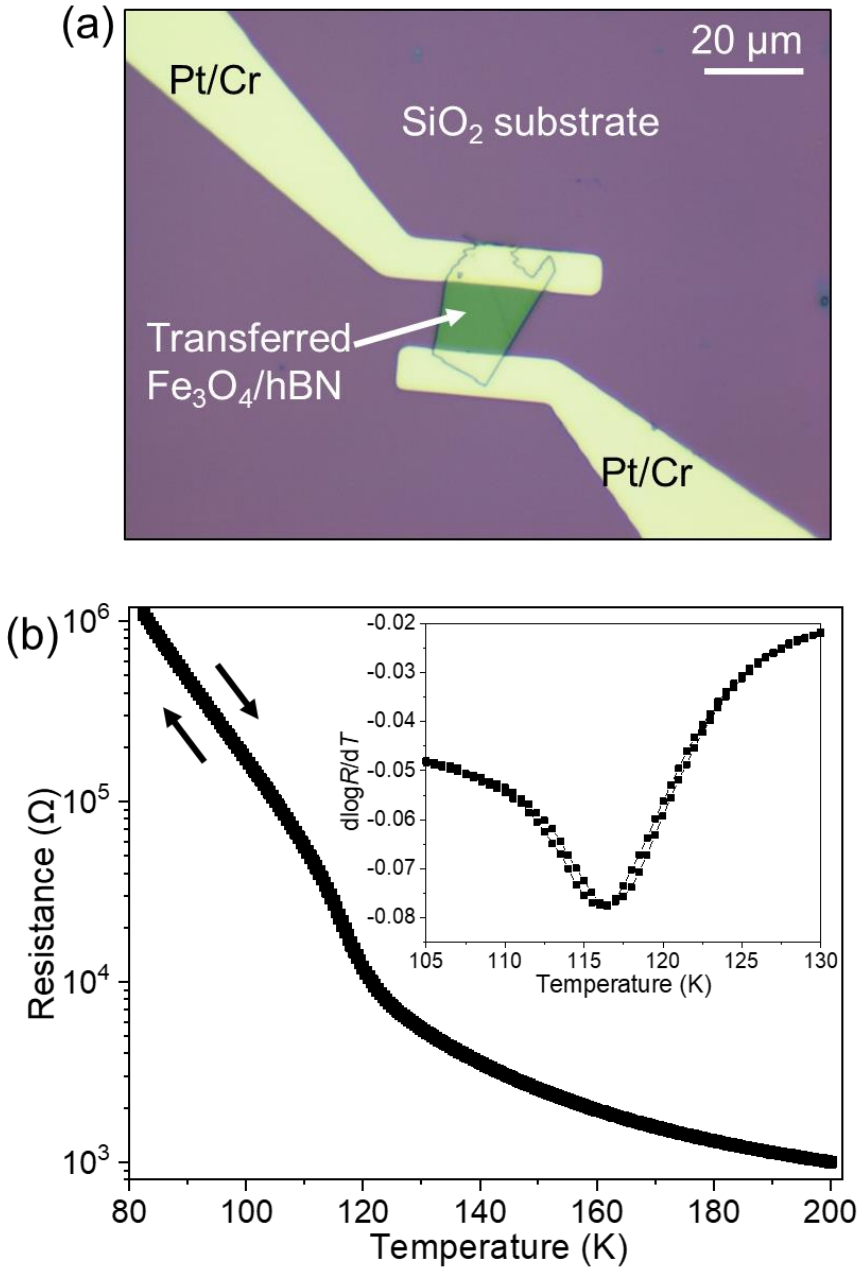

Figure 6.2.7 (a) Optical microscopy image of the Fe_3O_4/hBN stack transferred onto SiO_2/Si substrate with a pair of electrodes. (b) Electric transport property of the transferred Fe_3O_4/hBN stack. The inset indicates the first derivative of the resistivity change as a function of temperature.

6.3 Growth and characterization of $NdNiO_3$ thin films on hBN

The hBN flakes were mechanically exfoliated with the Scotch tape and transferred onto $SrTiO_3$ substrates. The hBN flakes were annealed in an air ambient at 773 K to remove adhesice residue. $NdNiO_3$ thin films were deposited using PLD method under the partial oxygen pressure of 30 Pa and the substrate temperature of 884 K using the sintered target with the chemical composition. The target was a buk crystal of $NdNi_{1.5}O_3$ [6.37, 6.38]. The laser frequency was 3 Hz. The thickness of the $NdNiO_3$ thin film was 100 nm. The confirmation of the growth of $NdNiO_3$ thin films on hBN was conducted using Raman spectroscopy at room temperature with the grating size of 1200 lines/mm and the laser power of 1 mW. AFM and TEM measurements were utilized to identify the surface structure of $NdNiO_3$ and the growth direction. The MIT property was measured after transfer of a $NdNiO_3$/hBN stack onto a SiO_2/Si substrate and electrode deposition.

Figure 6.3.1(a) shows the optical microscopy image of the hBN flakes on $SrTiO_3$(001) substrate after the growth of $NdNiO_3$ thin films. It was confirmed that the thin film was deposited homogeneously in the entire area. Figure 6.3.2(b) shows the Raman spectrum of the $NdNiO_3$ thin film on hBN. The observed Raman peaks are attributable to the Raman active oscillation modes of $NdNiO_3$ lattices, such as 250 (A_{1g}), 302 (B_{1g}), 347 (B_{1g}), and 427 (B_{2g}) cm^{-1} [6.39, 6.40] in addition to the Raman peak of hBN at 1368 cm^{-1} [6.35]. This means successful formation of the $NdNiO_3$ thin film on hBN.

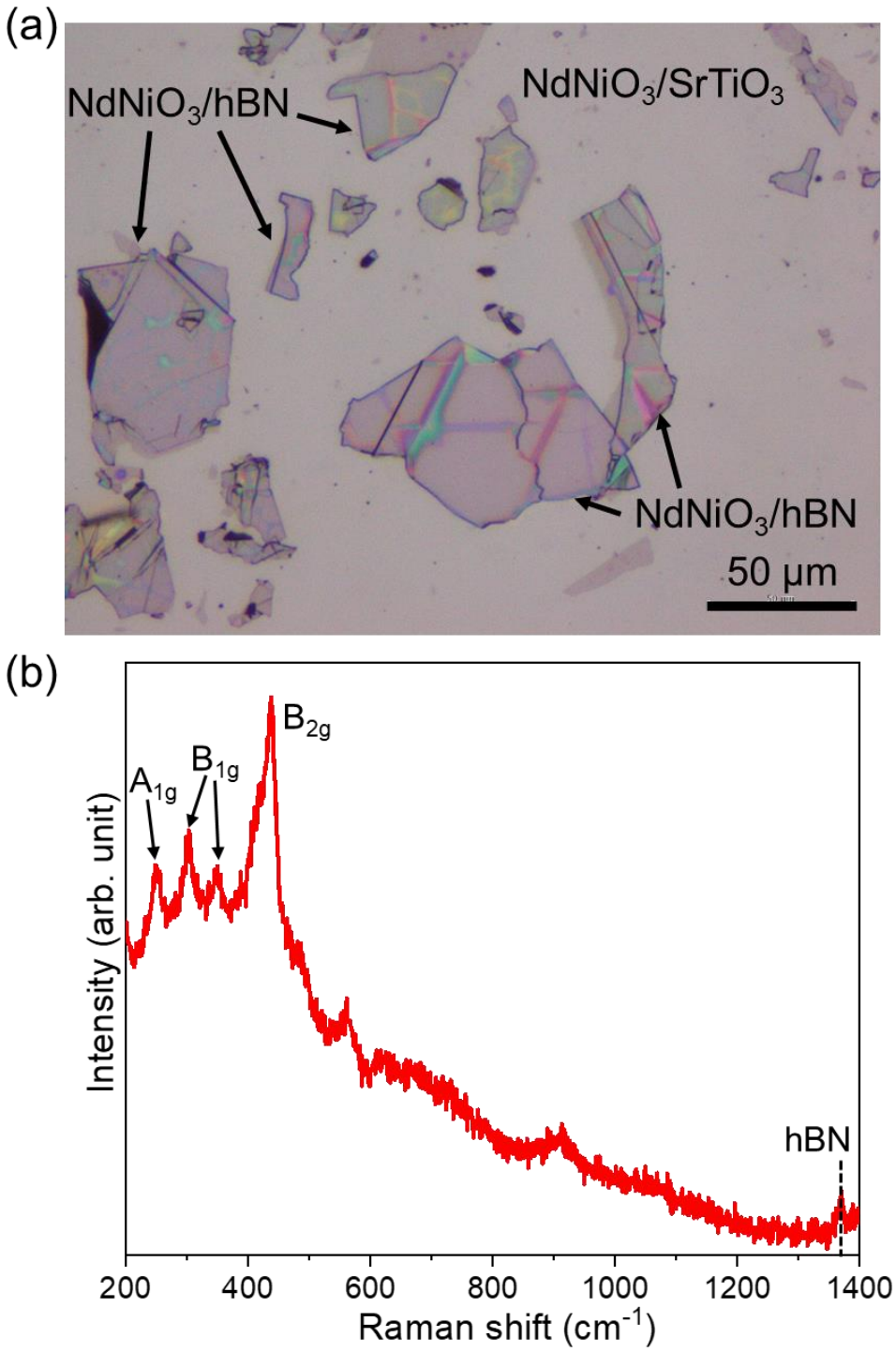

Figure 6.3.1 (a) Optical microscopy image of the hBN flakes on the $SrTiO_3$ substrate after the growth of $NdNiO_3$ thin film. (b) Raman spectrum of the $NdNiO_3$ thin film on hBN at room temperature.

After confirmation of the growth of $NdNiO_3$ thin films on hBN, the surface and cross-sectional structures were characterized using AFM and TEM. Figure 6.3.2(a) shows the AFM image of the $NdNiO_3$ thin film on hBN. The formation of grain structures with the size of tens of nanometers was clearly observed.

Next, Figure 6.3.2(b) shows the cross-sectional TEM image of the $NdNiO_3$/hBN stack including the interface. The parallel arrangement of $NdNiO_3$ and hBN lattices were clear observed at the bottom and the top of the image, respectively. Figure 6.3.2(d) shows the fast Fourier transformation (FFT) image of the $NdNiO_3$ region surrounded by the red square. The FFT spots were assigned using orthorhombic-$NdNiO_3$ for simplicity. It was revealed that the certain periodicities of the orthohombic-$NdNiO_3$ lattice corresponding to reflections 111, 101, and so forth. These reflections indicate that the crystal relationship between $NdNiO_3$ and hBN satisfies orthorhombic-$NdNiO_3$(111) // hBN(001). Generally, $NdNiO_3$ grows epitaxially on $SrTiO_3$(001) and $LaAlO_3$(001) with pseudocubic-$NdNiO_3$(001) [010] || $SrTiO_3$(001) [010] and pseudocubic-$NdNiO_3$(001) [010] || $LaAlO_3$(001) [010] orientation relations, reflecting the lattice parameters of $NdNiO_3$ and $SrTiO_3$ or $LaAlO_3$ [6.28, 6.30]. Considering the out-of-plane lattice constant in $NdNiO_3$, the growth plane of $NdNiO_3$ on hBN is estimated to correspond to pseudocubic-$NdNiO_3$(120) plane. Using the same estimation of lattice mismatch as that in Chapters 3.4 and 6.2, the total lattice mismatch between pseudocubic-$NdNiO_3$(120) and hBN(001) is estimated to be 7%. Despite the existence of such a large lattice mismatch, successful growth of $NdNiO_3$ thin films attest to weak van der Waals interactions.

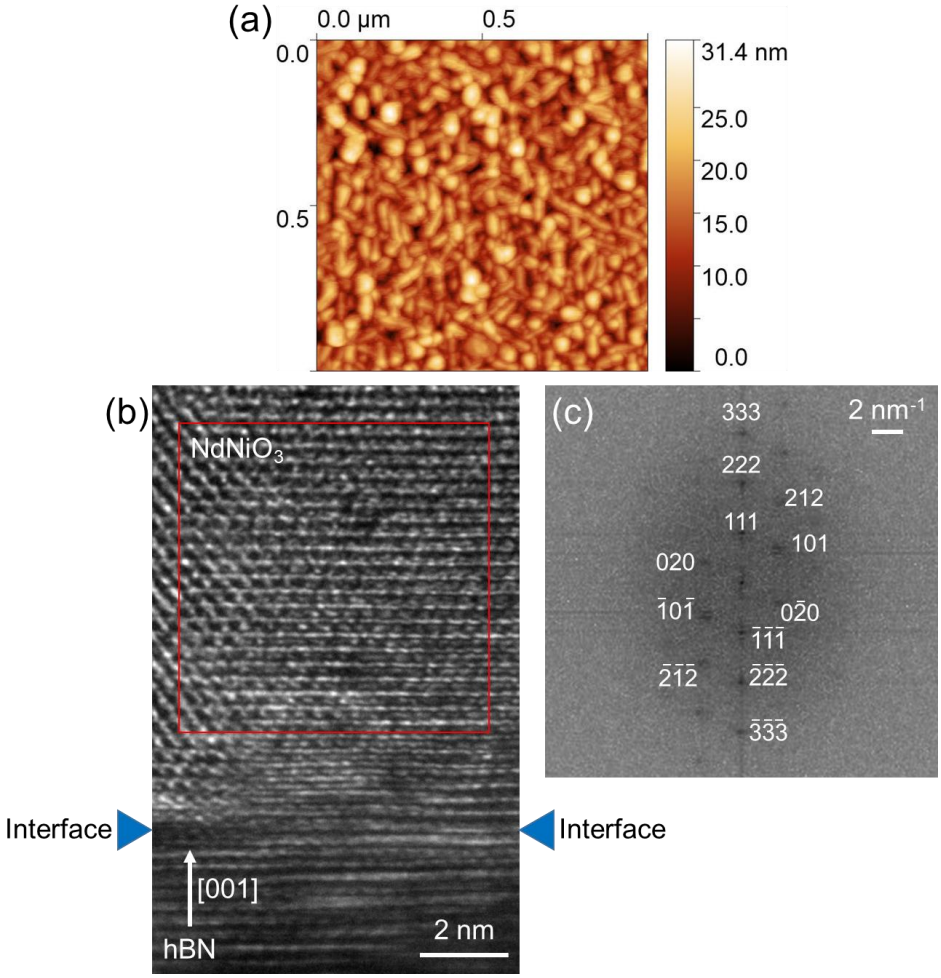

Figure 6.3.2 (a) AFM image of the $NdNiO_3$ thin film on hBN. (b) Cross-sectional TEM image of $NdNiO_3$ and hBN with the interface. The red square area is the $NdNiO_3$ region. (c) FFT image of the $NdNiO_3$ region.

Figure 6.3.3(a) shows the optical microscopy image of the transferred $NdNiO_3$/hBN stack on SiO_2 substrate after the electrode deposition. Figure 6.3.3(b) shows the *R*–*T* curve of the $NdNiO_3$/hBN stack in Fig. 6.3.3(a). In the measurement temperature region from 10 to 300 K, a resistance change of two orders of magnitude was observed with hysteresis property. This indicates that $NdNiO_3$ on hBN exhibited a resistance change owing to MIT. The transition temperature of $NdNiO_3$ was defined as the point of inflection defined as $\log|dR/dT|$. The first derivative of resistance as a function of

temperature is shown in the inset of Fig. 6.3.3(b). The transition temperature of $NdNiO_3$/hBN was determined to be 189 K. Since the transition temperature of bulk crystals of $NdNiO_3$ is 192 K [6.22], it was indicated that the $NdNiO_3$ film received few strain from at the interface of the $NdNiO_3$ thin film and the hBN, similarly to VO_2 and Fe_3O_4 thin films on hBN.

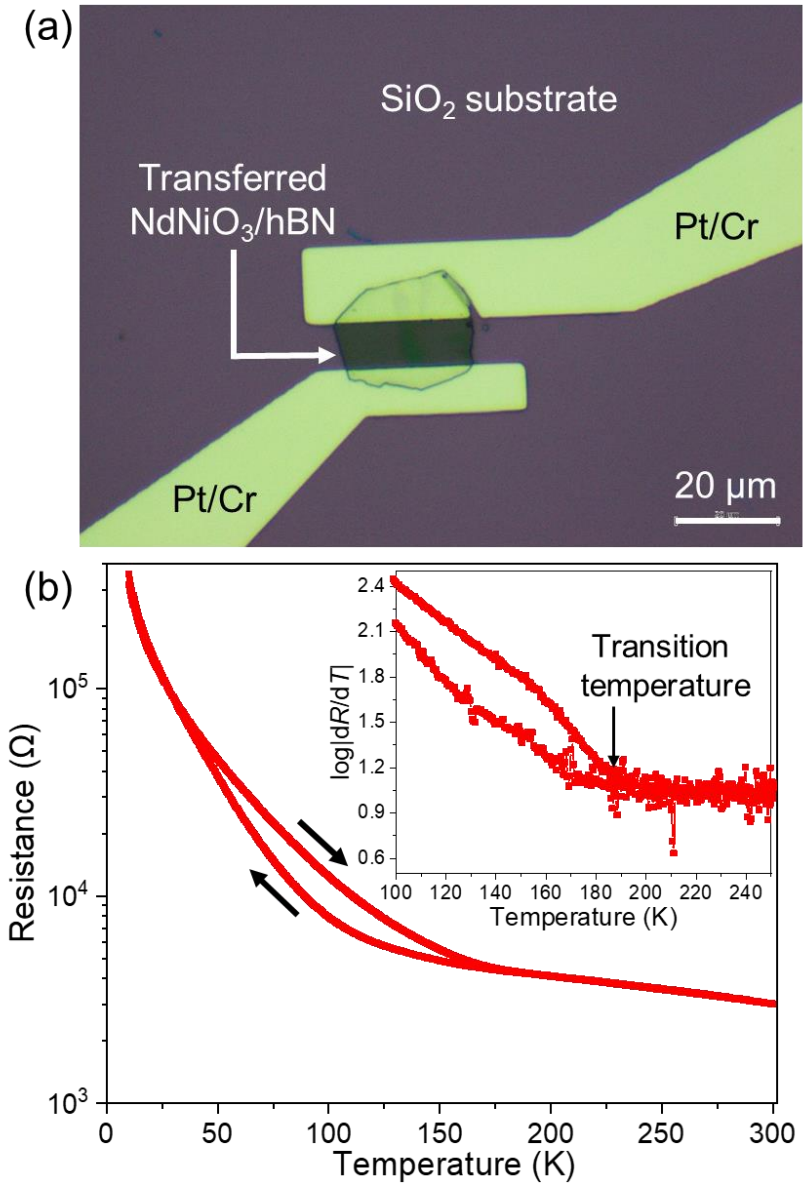

Figure 6.3.3 (a) Optical microscopy image of the transferred $NdNiO_3$/hBN stack on SiO_2 substrate with a pair of electrodes.

6.4 Summary of growth of transition metal oxide thin films on hBN

At last, the characteristics of thin films of VO_2, Fe_3O_4, and $NdNiO_3$ grown on hBN is summarized (Table 6.4.1). These transition metal oxide thin films have different lattice structures and lattice constants from those of hBN. The discrepancy would result in the big mismatch between transition metal oxides films and hBN.

It is notable that growth of VO_2, Fe_3O_4, and $NdNiO_3$ thin films was realized on hBN despite the bad matching of the lattice structures with the lattice mismatch of 13% (VO_2), 5% (Fe_3O_4), and 7% ($NdNiO_3$). Although growth of the triangle-shaped lattice planes on hexagonal lattices in Fe_3O_4/hBN implies geometric restrictions, the growth of the rectangle-shaped lattice planes on hexagonal lattices in VO_2/hBN and $NdNiO_3$/hBN is the significant characteristics of the growth of transition metal oxide thin films regardless of the lattice matching of thin films and substrates, which corresponds to the universality of hBN as a growth substrate.

Most importantly, the MIT properties accompanied with bulk like transition temperature were observed in all of VO_2, Fe_3O_4, and $NdNiO_3$ thin films on hBN, which is comparable to those grown on common single-crystal oxide substrates. Since the transition temperature is sensitive to the lattice strain in case of $NdNiO_3$ thin films, this results also support the relaxation of the lattice strain, which is consistent with the STEM images. The prominent MIT properties guarantee the formation of well-crystallized thin films, and I can declare that hBN has a high utility as a universal growth substrate for various transition metal oxide thin films showing clear MIT property.

Table 6.4.1 Summary of growth of transition metal oxide thin films on hBN

	VO_2/hBN	Fe_3O_4/hBN	$NdNiO_3$/hBN
Lattice structure of substrate	Hexagonal	Hexagonal	Hexagonal
Lattice constant of substrate	$a = b = 2.502$ Å $c = 3.331$ Å	$a = b = 2.502$ Å $c = 3.331$ Å	$a = b = 2.502$ Å $c = 3.331$ Å
Lattice structure of thin films	Tetragonal (Rutile)	Cubic (Spinel)	Orthorhombic (Perovskite)
Lattice constant of thin films	$a = b = 4.554$ Å, $c = 2.856$ Å	$a = b = c = 8.387$ Å	$a = 5.379$ Å, $b = 5.385$ Å, $c = 7.600$ Å
Growth planes on hBN (Structural matching)	VO_2(110)/hBN(001) (Rectangle/Hexagonal)	Fe_3O_4(111)/hBN(001) (Triangle/Hexagonal)	Otrhohombic-$NdNiO_3$(111)/hBN(001) (Triangle/Hexagonal)
Surface structure of thin films	Grain structures	Grain structures	Grain structures
Expected lattice mismatch	13%	5%	7%
MIT property (Log R_I/R_M, T_{IM})	3 orders of magnitude, 340 K	1 order of magnitude, 116 K	3 orders of magnitude, 189 K

6.5 Conclusion

In this chapter, the applicability of hBN as a universal growth substrate was investigated through growth of cubic-Fe_3O_4 and orthohombic-$NdNiO_3$ thin films on hBN and characterization of the crystal structures and MIT properties. Both of Fe_3O_4 and $NdNiO_3$ thin films were successfully grown on hBN. It was revealed that each of cubic-Fe_3O_4(111) and orthohombic-$NdNiO_3$(111) planes were observed to grow on hBN(001) planes through the cross-sectional STEM images. The shape of cubic-Fe_3O_4(111) plane satisfies the geometric symmetry of triangle and hexagonal structures. In the $NdNiO_3$ thin film on hBN, the pseudocubic-$NdNiO_3$(120) plane corresponding to orthohombic-$NdNiO_3$(111) plane is rectangle and has bad geometric matching with hBN. Despite the existence of the lattice mismatch of 5% (Fe_3O_4) and 7% ($NdNiO_3$) on hBN, the growth of Fe_3O_4 and $NdNiO_3$ thin films on hBN are the additional cases for the universal growth

of transition metal oxide thin films. Moreover, the prominent MIT properties of Fe_3O_4 and $NdNiO_3$ thin films on hBN were observed at the transition temperature of 116 K and 189 K, respectively. These transition temperatures are comparable to those of bulk crystals of Fe_3O_4 and $NdNiO_3$, respectively. Furthermore, the transfer of Fe_3O_4/hBN stacks without causing serious damage to the stacks was successfully demonstrated.

Judging from these results, the function of hBN as a universal growth substrate for transition metal oxide thin films was indicated. These results open a way for growth of various transition metal oxide thin films using hBN with the negligible interfacial lattice mismatch.

6.6 References

[6.1] E. J. W. Verwey, Nature, **144**, 327 (1939).

[6.2] M. Wakihara, Y. Shimizu, and T. Katsura, J. Solid State Chem., **3**, 478 (1971).

[6.3] X. W. Li, A. Gupta, G. Xiao, and G. Q. Gong, J. Appl. Phys., **83**, 7049 (1998).

[6.4] X. H. Liu, A. D. Rata, C. F. Chang, A. C. Komarek, and L. H. Tjeng, Phys. Rev. B, **90**, 125142 (2014).

[6.5] J. Noh, O. I. Osman, S. G. Aziz, P. Winget, and J.-L. Bredas, Chem. Matter., **27**, 5856 (2015).

[6.6] S. B. Ogale, K. Ghosh, R. P. Sharma, R. L. Greene, R. Ramesh, and T. Venkatesan, Phys. Rev. B, **57**, 7823 (1998).

[6.7] S. Tiwari, R. Prakash, R. J. Choudhary, and D. M. Phase, J. Phys. D: Appl. Phys., **40**, 4943 (2007).

[6.8] E. J. Preisler, J. Brooke, N. C. Oldham, and T. C. McGill, J. Vac. Sci. Technol. B, **21**, 1745 (2003).

[6.9] R. Prakash, R.J. Choudhary, L.S.S. Chandra, N. Lakshmi, and D.M. Phase J. Phys. Condens. Matter, **19**, 486212 (2007)

[6.10] S. Jain, A. O. Adeyeye, and C. B. Boothroyd, J. Appl. Phys., **97**, 093713 (2005).

[6.11] X. Liu, C.-F. Chang, A. D. Rata, A. C. Komarek, and L. H. Tjeng, NPJ Quantum Mater., **1**, 16027 (2016).

[6.12] J. M. De Teresa, A. Fernández-Pacheco, L. Morellón, J. Orna, J. A. Pard, D. Serrate, P. A. Algarabel, and M. R. Ibarra, Microelectron. Eng., **84**, 1660 (2007).

[6.13] D. M. Phase, S. Tiwari, R. Prakash, A. Dubey, and V. G. Sathe, J. Appl. Phys., **100**, 123703 (2006).

[6.14] P.-C. Wu, P.-F. Chen, T. H. Do, Y.-H. Hsieh, C.-H. Ma, T. D. Ha, K.-H. Wu, Y.-J.

Wang, H.-B. Li, Y.-C. Chen, J.-Y. Juang, P. Yu, L. M. Eng, C.-F. Chang, P.-W. Chiu, L. H. Tjeng, and Y.-H. Chu, ACS Appl. Mater. Interfaces, **8**, 33794 (2016).

[6.15] W. Hou, Z. Zhou, L. Zhang, S. Zhao, B. Peng, Z. Hu, W. Ren, Z.-G. Ye, Z.-D. Jiang, and M. Liu, ACS Appl. Mater. Interfaces, **11**, 21727 (2019).

[6.16] H. K. Christenson and N. H. Thomson, Surf. Sci. Rep., **71**, 367 (2016).

[6.17] Y. Lin, H. Y. Xu, Z. Q. Wang, T. Cong, W. Z. Liu, H. L. Ma, and Y. C. Liu, Appl. Phys. Lett., **110**, 193503 (2017).

[6.18] L. Pan, X. Zhu, X. Xie, and Y. Liu, Adv. Funct. Mater., **25**, 3341 (2015).

[6.19] L. Pan, X. D. Zhu, X. M. Xie, and Y. T. Liu, J. Mater. Chem. A, **3**, 2726 (2015).

[6.20] Z.-Q. Duan, Y.-T. Liu, X.-M. Xie, X.-Y. Ye, and X.-D. Zhu, Chem.–Asian J., **11**, 828 (2016).

[6.21] I. V. Nikulin, M. A. Novojilov, A. R. Kaul, S. N. Mudretsova, and S. V. Kondrashov, Mater. Res. Bull., **39**, 775 (2004).

[6.22] M. K. Hooda and C. S. Yadav, Phys. B: Condens. Matter, **491**, 31 (2016).

[6.23] J. Liu, M. Kargarian, M. Kareev, B. Gray, P. J. Ryan, A. Cruz, N. Tahir, Y.-D. Chuang, J. Guo, J. M. Rondinelli, J. W. Freeland, G. A. Fiete, and J. Chakhalian, Nat. Commun., **4**, 2714 (2013).

[6.24] W. L. Lim, E. J. Moon, J. W. Freeland, D. J. Meyers, M. Kareev, J. Chakhalian, and S. Urazhdin, Appl. Phys. Lett., **101**, 143111 (2012).

[6.25] C. Oh, S. Heo, H. M. Jang, and J. Son, Appl. Phys. Lett., **108**, 122106 (2016).

[6.26] U. Sidik, A. N. Hattori, R. Rakshit, S. Ramanathan, and H. Tanaka, ACS Appl. Mater. Interfaces, **12**, 54955 (2020).

[6.27] U. Sidik, A. N. Hattori, K. Hattori, M. Alaydrus, I. Hamada, L. N. Pamasi, and H. Tanaka, ACS Appl. Electron. Mater., **4**, 4849 (2022)

[6.28] Y. Kumar, R. J. Choudhary, S. K. Sharma, M. Knobel, and R. Kumar, Appl. Phys. Lett., **101**, 132101 (2012).

[6.29] R. Scherwitzl, P. Zubko, I. G. Lezama, S. Ono, A. F. Morpurgo, G. Catalan, and J. M. Triscone, Adv. Mater., **22**, 5517 (2010).

[6.30] G. Catalan, R. M. Bowman, and J. M. Gregg, Phys. Rev. B, **62**, 7892 (2000).

[6.31] A. Tiwari, C. Jin, and J. Narayan, Appl. Phys. Lett., **80**, 4039 (2002).

[6.32] R. Rakshit, A. N. Hattori, Y. Naitoh, H. Shima, H. Akinaga, and H. Tanaka, Nano Lett., **19**, 5003 (2019).

[6.33] J. L. Verble, Phys. Rev. B, **9**, 5236 (1974).

[6.34] L. V. Gasparov, D. B. Tanner, D. B. Romero, H. Berger, G. Margaritondo, and L. Forró, Phys. Rev. B, **62**, 7939 (2000).

[6.35] R. Geick, C. H. Perry, and G. Rupprecht, Phys. Rev., **146**, 543 (1966).

[6.36] O. N. Shebanova and P. Lazor, J. Raman Spectrosc., **34**, 845 (2003).

[6.37] T. Yamanaka, A. N. Hattori, L. N. Pamasi, S. Takemoto, K. Hattori, H. Daimon, K. Sato, H. Tanaka, ACS Appl. Electron. Mater., **1**, 2678 (2019).

[6.38] H. Ren, A. I. Osaka, A. N. Hattori, B. Yu, M. Nagai, M. Ashida, B. Li, C. Zou, and H. Tanaka, ACS Appl. Electron. Mater., **4**, 3495 (2022).

[6.39] Y. Kumar, R. J. Choudhary, and R. Kumar, J. Appl. Phys., **120**, 115306 (2016).

[6.40] K. Soni, S. Harisankar, M. Prajapat, K. R. Mavani Appl. Phys. A, **125**, 561 (2019).

Chapter 7

General conclusion

In this dissertation, the functionality of hBN as a universal growth substrate for various transition metal oxide thin films and identification of the size of metallic domains, which are the spatial elements to determine the MIT property, and electrical switching application of VO_2/hBN microstructures were studied.

In Chapter 3, growth of VO_2 thin films on hBN was attempted and the lattice structure was characterized using Raman spectroscopy, AFM, and STEM. It was revealed that and the rutile-VO_2(110) planes, whose surface energy is theoretically favorable, were observed to grow on hBN(001) planes despite the expected existence of interfacial lattice mismatch of 13%. Moreover, the VO_2 thin films on hBN have grain structures on the surface with the size of ~300 nm on average in length, which is one order of magnitude larger than that of VO_2 thin films on Al_2O_3(0001). The MIT properties of VO_2 thin films were investigated through electric transport measurements. A resistance change of three orders of magnitude was observed in the VO_2 thin films on hBN, which guarantees the prominent MIT property.

In Chapter 4, the size of metallic domains, which are the spatial elements to determine the MIT property, were investigated using temperature-dependent Raman spectroscopy and optical microscopy. The size of the metallic domains was determined to be ~500 nm on average in length, which is one order of magnitude larger than that of VO_2 thin films on Al_2O_3 substrates. Owing to the large-sized metallic domains, it was discovered that the confinement effect of the metallic domains occurs even in the micrometer scale and a single-resistance jump changing by one or two orders of magnitude was observed with the device size of ~2 μm in length.

In Chapter 5, micro-structured VO_2/hBN was fabricated with the size of ~2 μm in length for electrical switching using confined metallic domains. It was discovered that

step electric current increase was observed owing to the emergence of the metallic domains confined in the micrometer scale. The emergence of the metallic domains was also confirmed by the simultaneous operando observation. These results open a way for application in domain engineering.

In Chapter 6, the applicability of hBN as a universal growth substrate was studied through growth of Fe_3O_4 and $NdNiO_3$ thin films on hBN. The structural characterization revealed that these thin films have grain structures on the surfaces and cubic-Fe_3O_4(111) and orthohombic-$NdNiO_3$(111) planes were grown on hBN(001), respectively. Similarly to VO_2 thin films on hBN, Fe_3O_4 and $NdNiO_3$ thin films exhibited clear MIT properties at the transition temperature of 116 K and 189 K, respectively accompanied with a resistance change of one order of magnitude. The transition temperatures were comparable to those of bulk crystals.

In summary, these results indicate the negligible interfacial lattice strain and the functionality of hBN as a growth substrate regardless of lattice structures and lattice constants of transition metal oxide thin films. In addition, the device application of VO_2/hBN structures was demonstrated with the confinement effect of the metallic domains.

Appendix

A1. Bubble-free transfer method

As reported in Chapter 2, thin film/hBN stacks can be transferred using transparent polymer exposed to water vapor. This transfer method is very easy to utilize since the polymer can be easily attached onto and removed from the target substrates, similarly to the Scotch tape method. However, the transfer of thin film/hBN stacks onto a certain area, for example on an electrode, TMDC materials and so forth with high accuracy in the position alignment is still challenging just using polymer. In addition, the efficiency in the pickup of the thin film/hBN stacks is still low due to the low adhesive force at the interface of the thin film and polymer. Thus, to broaden fabrication of various heterostructures using two-dimensional layered materials, the establishment of a new method to transfer these materials should be established. In 2020, Iwasaki et al. have reported a unique transfer method called "Bubble-free transfer method" [A1]. In this method, various kinds of polymers are spin-coated layer by layer on a transparent polymer to make transfer stamps. The bubble-free transfer method utilizes the difference in the stiffness of the polymer by changing the temperature of the stamp.

Figure A1(a) shows the overview of the transfer machine composed of optical microscopy, stamp manipulator, rubber heater, and temperature controller for bubble-free transfer method. Figure A1(b) shows the schematic of the fabrication of transfer stamps. First, 3 mm square transparent polymer was attached onto a slide glass. Then, PDMS polymer (Silicon potting gel) was spin-coated on the polymer. The stamp was baked on a hot plate at 343 K overnight. Next, O_2 plasma was irradiated to the stamp using RIE method. Finally, a solution with the anisole propylene carbonate (PPC) was spin-coated on the stamp and baked at 383 K for 5 minutes. Figure A1(c) shows the schematic of the transfer process. First, the stamp was attached to the target sample at room temperature.

Next, the temperature was raised up to 328 K to soften the polymer on the stamp. Next, the temperature of the sample stage was decreased to 313 K to make the polymer stiff. Confirming the stabilization of the temperature of the sample stage, the stamp was brought up to pick up the thin film/hBN stacks. After that, the stacks of thin film/hBN were transferred onto another substrate with the stage temperature of 383 K.

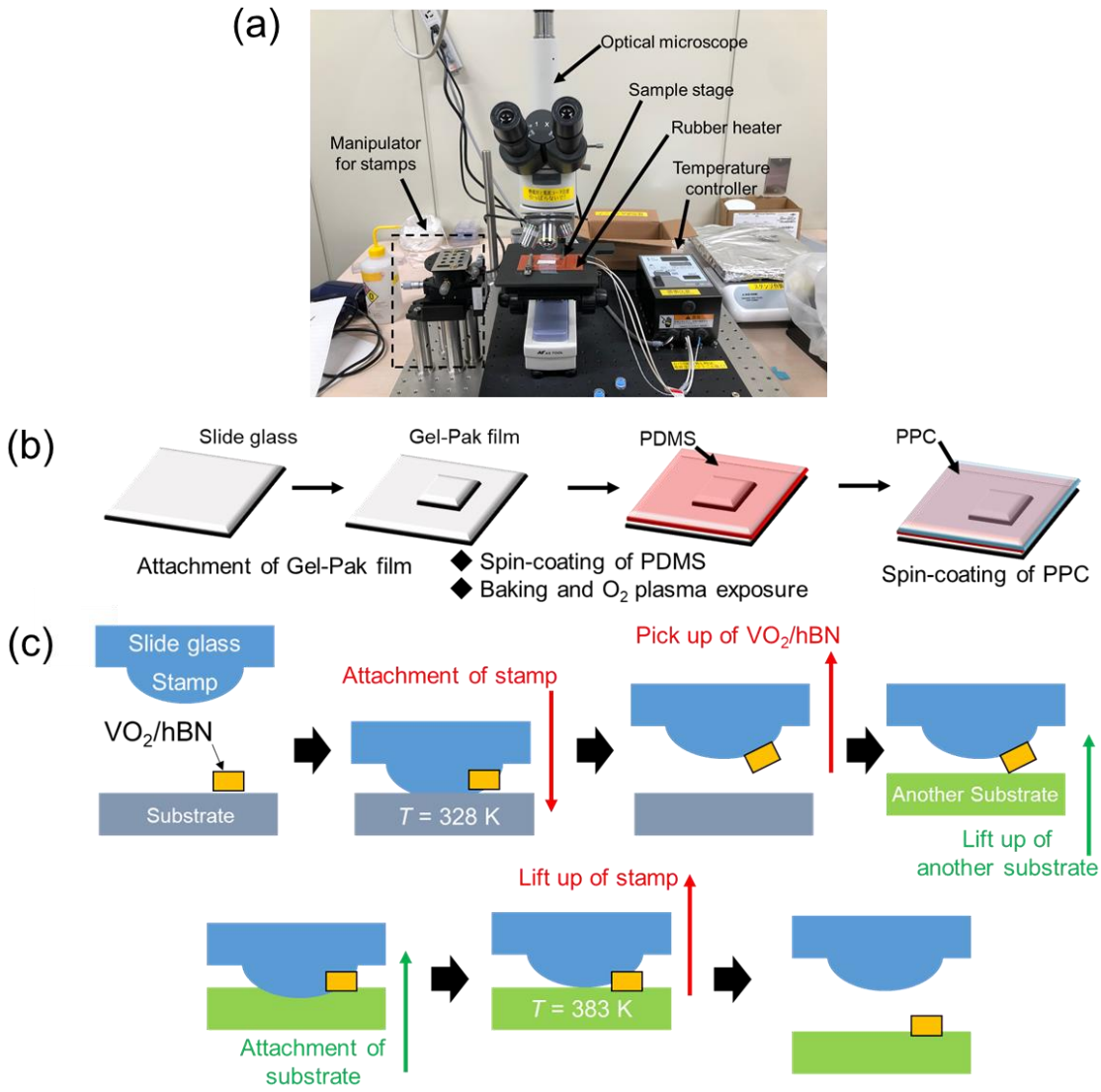

Figure A1 (a) Overview of the transfer machine for the bubble-free transfer method. (b) Schematic of fabrication of transfer stamps. (c) Schematic of the transfer process using transfer stamps.

Figure A2 shows the optical microscopy images of a VO_2/hBN stack before and after the bubble-free transfer method. The VO_2/hBN stack was transferred from a SiO_2 substrate onto Au/Cr electrodes on another SiO_2 substrate. It is notable that the VO_2/hBN stack was transferred with high accuracy in the position alignment. Moreover, other VO_2/hBN stacks around the target VO_2/hBN stack were simultaneously transferred because of the high efficiency in the transfer of the VO_2/hBN stacks. These results indicate the usage of the bubble-free transfer method for fabrication of heterostructures using two-dimensional layered materials.

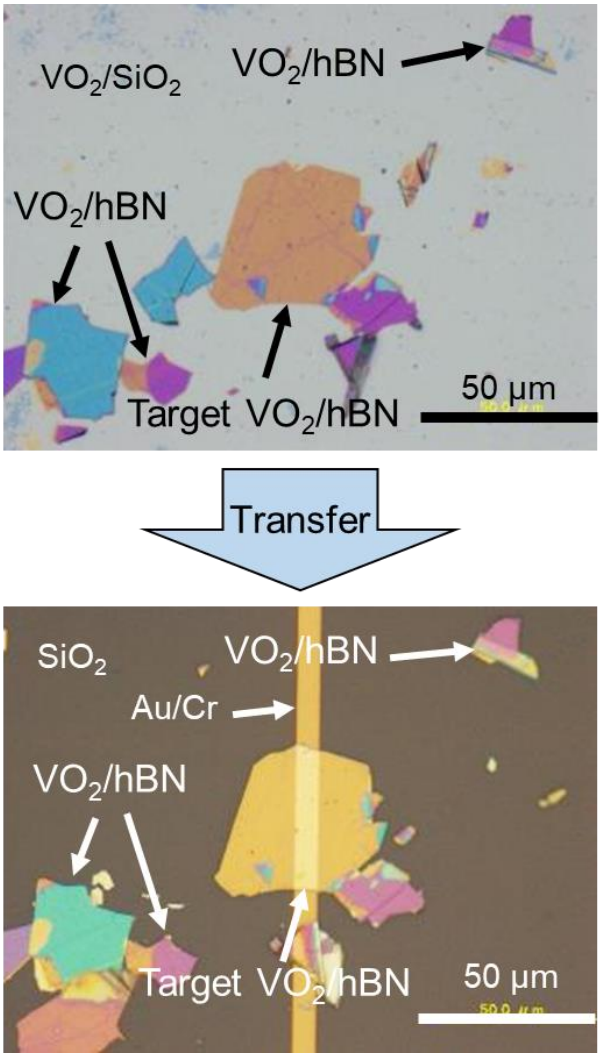

Fig. A2 Optical microscopy images of a VO_2/hBN stacks before transfer and after transfer onto Au/Cr electrode.

A2. Growth of VO_2 thin films on chemical vapor deposition-grown hBN sheets

High-quality hBN flakes have been obtained from bulk hBN crystals. As indicated in Chapters 3 and 6, hBN has a possibility of a universal substrate for growing various transition metal oxide thin films regardless of the interfacial lattice matching. However, there exists some difficulty in handling hBN flakes. For example, transfer of hBN flakes with high accuracy in position alignments and avoiding cracks or wrinkles during transfer process hinders the smooth fabrication of devices. In addition, the size of the hBN flakes are up to approximately 100 μm. Thus, fabrication and integration of numerous devices using transition metal oxide thin films on hBN is still challenging.

Recently, Professor Ago Group in Kyushu University reported growth of hBN sheets using chemical vapor deposition (CVD) method [A2–A4]. Impressively, the size of the CVD-hBN sheets is up to centimeter scale [A2–A4]. Their CVD-hBN sheets have been studied for flexible devices, such as transistors combined with graphene and other two-dimensional layered materials [A5]. Such a large-scaled hBN sheets are attractive for integration of devices and fabrication of flexible devices using transition metal oxide thin films. Moreover, crystallinity of transition metal oxide thin films on hBN could be studied various methods, such as X-ray diffraction (XRD), X-ray photoelectron spectroscopy, and so forth. Therefore, use of CVD-hBN sheets could contribute to fabrication of novel devices and investigation on the material properties of transition metal oxide thin films on hBN.

Figure A3(a) shows schematic of the synthesis process of hBN sheets through the CVD method. First, Ni and Fe catalysts are prepared on single-crystal substrates, such as Al_2O_3 substrates. Then, in the annealing process of the sample with hydrogen, the Ni and Fe catalysts become chemical compounds of Ni and Fe. With supply of borazine, boron

and nitrogen atoms are dissolved on the surface of the catalysts. With decreasing temperature of the sample slowly, the hBN sheets can be obtained on the catalysts. Figure A3(b) shows the SEM image of the synthesized hBN sheets on Ni-Fe catalysts. Clear layer-by-layer structure of hBN was observed with the distance between each plane of 0.35 nm. This distance is almost same as that of single-crystal bulk crystals of hBN and the formation of hBN sheets is guaranteed. Finally, the hBN sheets on the catalysts are transferred onto arbitrary substrates, such as SiO_2/Si substrates.

In my experiments, VO_2 thin films were grown on CVD-hBN sheets on SiO_2/Si substrates. VO_2 thin films were formed using PLD with ArF excimer laser (λ = 193 nm) and the partial oxygen pressure of 0.95 Pa and the substrate temperature of 723 K. The laser frequency was 2 Hz. Formation of VO_2 thin films on hBN was confirmed using out-of-plane X-ray diffraction (XRD, Ultima4, Rigaku) with the Cu Kα line (λ = 1.5405 Å). The beam spot size was 2 mm. For investigation on the MIT property of VO_2 thin films on CVD-hBN sheets, electrodes composed of Pt (40 nm) and Cr (5 nm) were deposited using sputtering deposition. The size of the electrodes is 200 μm in length and width. For investigation on the size-dependent MIT property, the electrodes were arranged with constant distances in the entire region of VO_2 thin film. The MIT property was investigated though electric transport measurements with the ramping rate of 6 K/min and 0.2 K step.

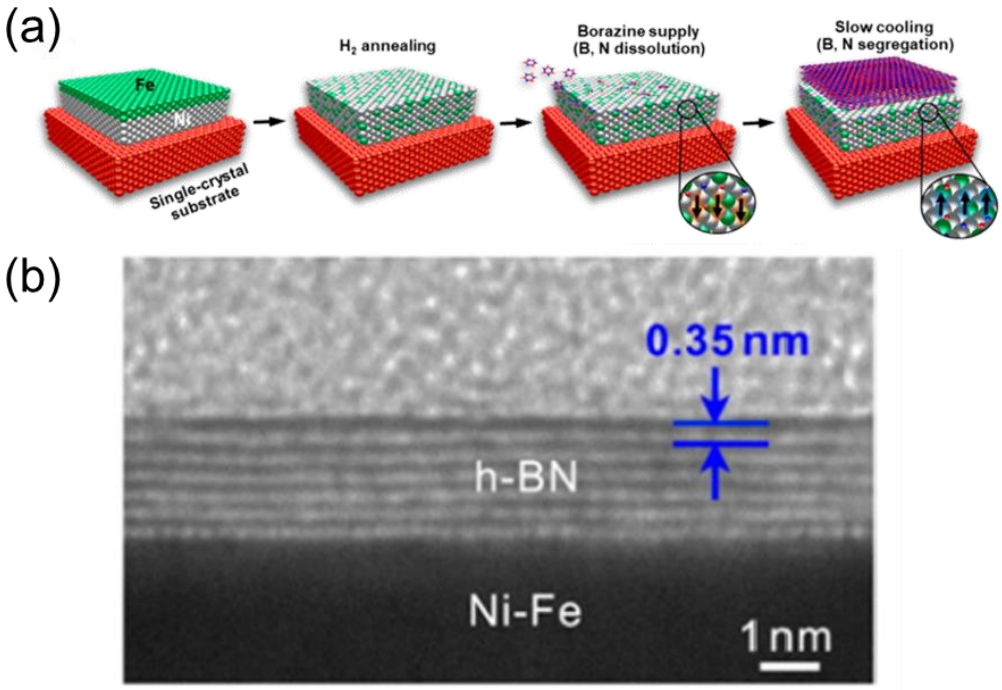

Fig. A3 (a) Schematic of the synthesis process of CVD-hBN sheets using Fe-Ni catalysts [A2]. (b) Cross-sectional SEM image of CVD-hBN sheet on Ni-Fe catalyst [A2].

Figure A4(a) shows an optical microscopy image of VO_2 thin films grown on the CVD-hBN sheet. It was confirmed that the VO_2 thin films were formed homogeneously in the entire sample of the CVD-hBN sheet. Figure A4(b) shows out-of-plane XRD spectrum of the VO_2 thin film on the CVD-hBN sheet prepared on a SiO_2/Si substrate. In addition to the strong peaks of (002) and (004) planes of Si at 2θ = 31.00° and 67.19°, respectively [A6], the peaks attributable to hBN (002) and (004) planes were observed at 2θ =26.00° and 55.00°, respectively [A7]. This guarantees the existence of hBN sheets oriented along [001] direction on SiO_2/Si substrate. Importantly, the peaks attributable to (110), (020), (220) and (040) planes of rutile-phase VO_2 were observed at 2θ = 27.00°, 40.00°, 57.00°, 86.00°, respectively [A8–A12]. The result of the growth of (110) planes of rutile-phase VO_2 on hBN(001) is consistent with that discovered with STEM images indicated in Chapter 3.4. However, the growth of (020) and (040) planes of rutile-phase

VO_2 on hBN(001) was discovered for the first time. It should be noted that the sample region in the STEM measurement and XRD measurement is considerably different. The STEM measurement was conducted for atomically local cross-sectional regions of VO_2 lattices, while the XRD measurement was conducted for the 5 mm square-sized VO_2 sample. Therefore, it may be natural that VO_2 thin films have two growth direction along [110] and [020] axis on hBN(001) in the macro-scale entire region of the sample.

Although the rutile-VO_2(110) planes are the most energetically favorable among VO_2 lattice planes, rutile-VO_2(110) planes have a lattice mismatch of 13% with hBN(001) planes. In contrast, the rutile-VO_2(020) plane has the small lattice mismatch of 9% with hBN(001) planes, although rutile-VO_2(020) plane is not energetically favorable [A13]. These results imply the existence of the epitaxial relationship between VO_2 lattices and hBN(001) in some area. Still, the growth of the energetically favorable planes on hBN is partially true even in CVD-hBN sheets, considering the thin film growth without the effect of lattice mismatch, which is the characteristic of growth of transition metal oxide thin films contributed by weak van der Waals interactions. Further experiments, such as in-plane XRD and in-plane STEM observations, are needed for uncovering the epitaxial relationship between VO_2 and hBN.

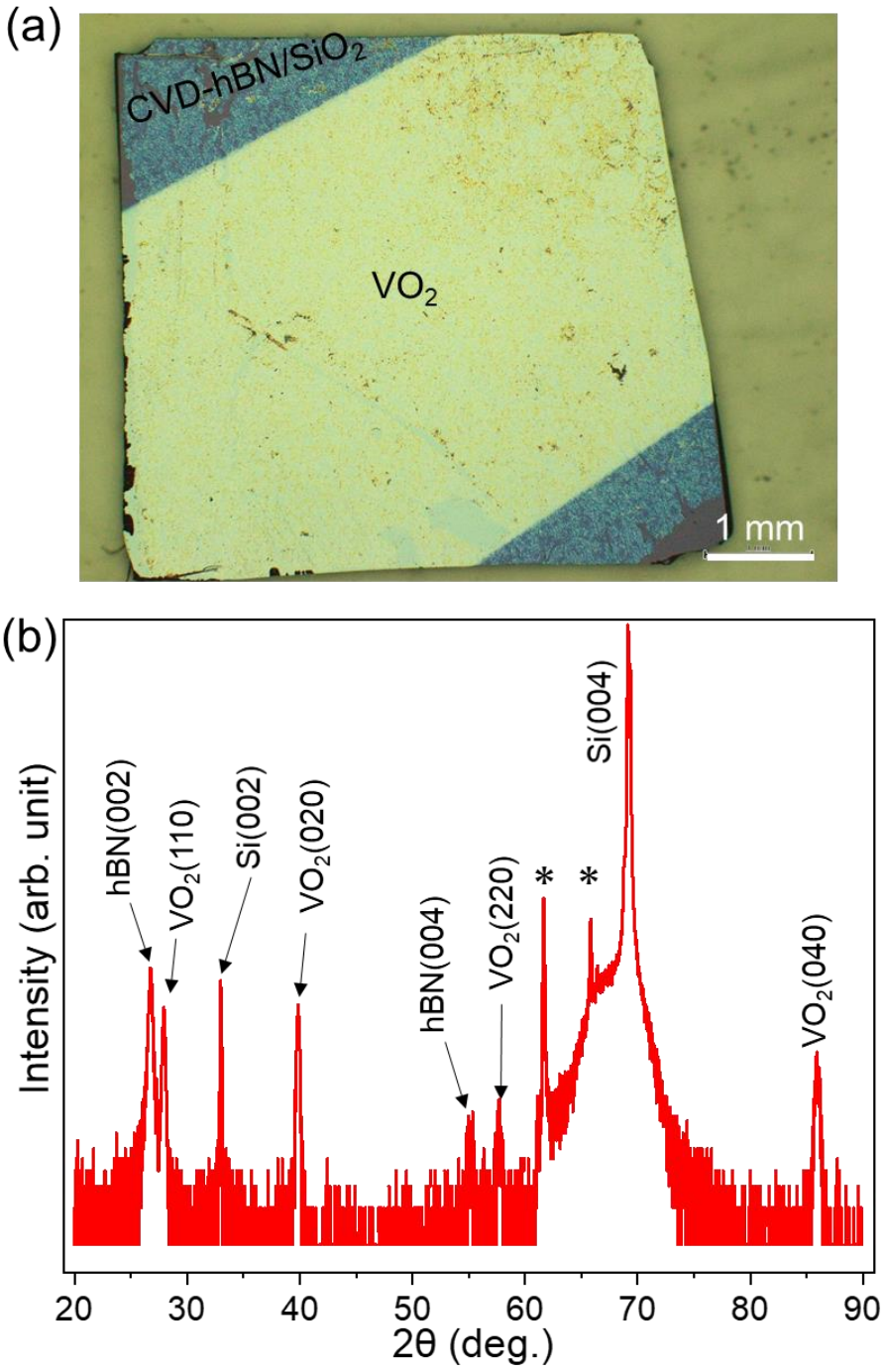

Fig. A4 (a) Optical microscopy image of VO_2 thin film grown on CVD-hBN sheet on SiO_2 substrate with the size of 5 mm square. (b) Out-of-plane XRD spectrum of VO_2 thin film on CVD-hBN sheet. The peaks with * marks are attributable to characteristic X-ray.

Next, Pt/Cr electrodes were deposited on the VO_2 thin film on CVD-hBN sheet for electrical transport measurements. Figure A5(a) shows the optical microscopy image of the VO_2 thin film on CVD-hBN sheet with Pt/Cr electrodes. The electrode gap distances were from 5 to 500 μm. Figure A5(b) shows the *R–T* curves of VO_2 thin film on CVD-hBN sheet with different electrode gap distances. Clear resistance changes of three orders of magnitude at approximately 340 K were observed regardless of the electrode gap distance. Importantly, the MIT property of the VO_2 thin film on CVD-hBN sheet is maintained for the 500 nm-sized electrode gap distance. It is notable that the MIT property of the VO_2/CVD-hBN sheet was observed for the first time even in hundreds of nanometer scale since the sizes of single-crystal hBN flakes are up to ~100 μm. These results indicate the utility of the large-sized CVD-hBN sheets.

These results indicate the applicability of CVD-hBN sheet as a large-scaled universal growth substrate for transition metal oxide thin films and an intriguing platform for integration of devices using transition metal oxide thin films. Further research would contribute to the exploration of growth of transition metal oxide thin films showing novel material properties and their device application.

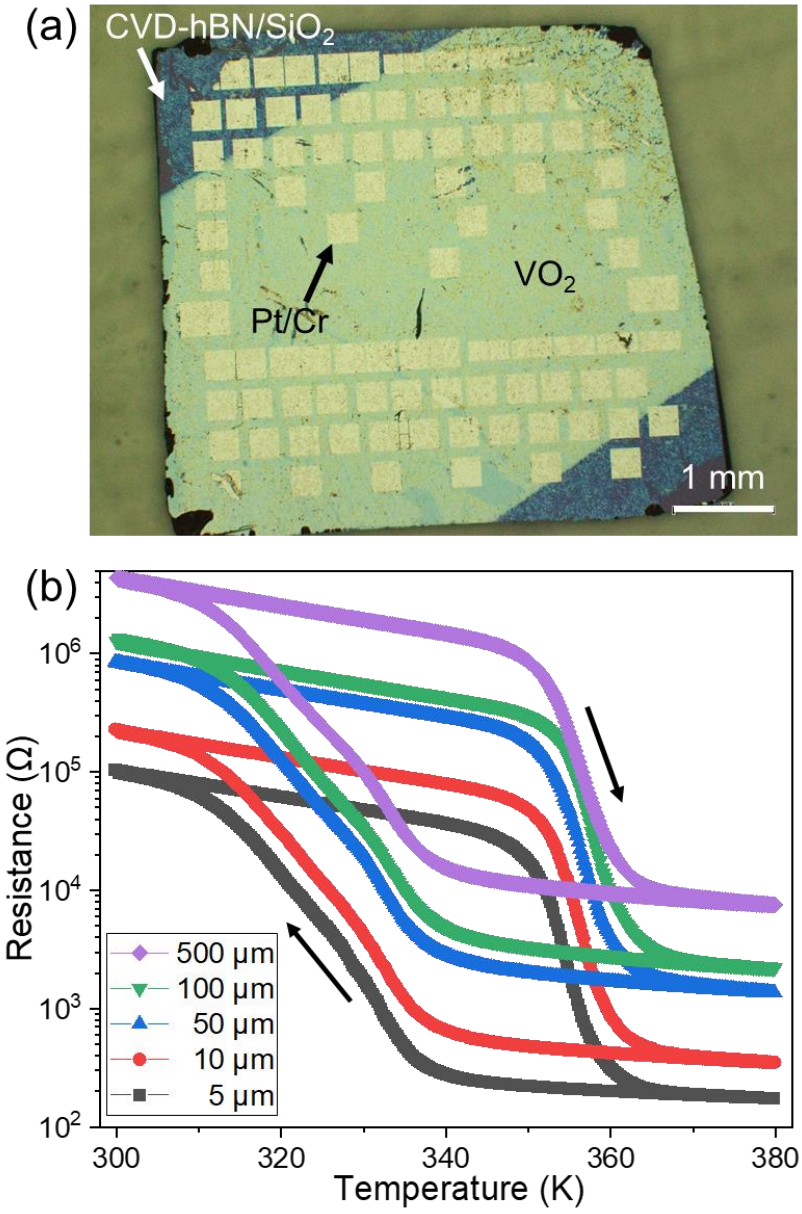

Fig. A5 (a) Optical microscopy image of VO_2 thin film grown on CVD-hBN sheet on SiO_2 substrate after Pt/Cr electrode deposition. (b) *R–T* curves of VO_2 thin film on CVD-hBN sheet with different electrode gap distances.

A3. Conclusion of Appendix

In Appendix, a new transfer technique of “bubble-free transfer method” was demonstrated for VO_2/hBN stacks onto other materials with high efficiency and high position alignment. A VO_2/hBN stack was successfully transferred onto Au/Cr electrodes without causing serious damage, such as formation of cracks or wrinkles using the transfer stamps composed of spin-coated polymer. Compared with the conventional transfer technique using PDMS sheet, this bubble-free transfer method is promising for fabrication of cross-sectional heterostructures by accumulating the stacks of thin films/hBN and two-dimensional layered materials.

Next, using the large-sized hBN sheets synthesized by CVD method, growth of VO_2 thin films was attempted on CVD-hBN sheets. The out-of-plane XRD spectrum of VO_2 was observed in addition to the peak of Si and hBN. Although the growth plane of rutile-VO_2(110) is consistent with the result of the STEM measurement in Fig. 3.4.2, another growth plane of rutile-VO_2(020) was observed, which means that VO_2 thin films are polycrystalline on hBN. However, it is notable that MIT property was homogeneously observed in the VO_2 areas with the electrode gap distance ranging from 5 to 500 μm. These results open a way for growth of various transition metal oxide thin films in a large scale and contributes to the fabrication of large-sized flexible/transferable devices.

A4. References

[A1] T. Iwasaki, K. Endo, E. Watanabe, D. Tsuya, Y. Morita, S. Nakaharai, Y. Noguchi, Y. Wakayama, K. Watanabe, T. Taniguchi, and S. Moriyama, ACS Appl. Mater. Interfaces, **12**, 8533 (2020).

[A2] Y. Uchida, S. Nakandakari, K. Kawahara, S. Yamasaki, M. Mitsuhara, and H. Ago, ACS Nano, **12**, 6236 (2018).

[A3] Y. Uchida, K. Kawahara, S. Fukamachi, and H. Ago, ACS Appl. Electron. Mater., **2**, 3270 (2020).

[A4] A. B. Taslim, H. Nakajima, Y.-C. Lin, Y. Uchida, K. Kawahara, T. Okazaki, K. Suenaga, H. Hibino, and H. Ago, Nanoscale, **11**, 14668 (2019).

[A5] A. S. Aji, P. Solís-Fernández, H. G. Ji, K. Fukuda, and H. Ago, Adv. Funct. Mater., **27**, 1703448 (2017).

[A6] M. D. McDaniel, A. Posadas, T. Q. Ngo, A. Dhamdhere, D. J. Smith, A. A. Demkov, and J. G. Ekerdt, J. Vac. Sci. Technol. A, **31**, 01A136 (2013).

[A7] S. Yuan, B. Toury, C. Journet, and A. Brioude, Nanoscale, **6**, 7838 (2014).

[A8] W.-J. Lee and Y.-H. Chang, Coatings, **8**, 431 (2018).

[A9] Y. Muraoka and Z. Hiroi, Appl. Phys. Lett., **80**, 583 (2002).

[A10] M. Kumar, S. Rani, H. H. Lee, J. Korean Phys. Soc., **75**, 519 (2019).

[A11] K. G. West, J. W. Lu, L. He, D. Kirkwood, W. Chen, T. P. Adl, M. S. Osofsky, S. B. Qadri, R. Hull, and S. A. Wolf, J. Supercond. Novel Magn., **21**, 87 (2008).

[A12] K. Okimura, Y. Sasakawa, and Y. Nihei, Jpn. J. Appl. Phys., **45**, 9200 (2006).

[A13] T. A. Mellan and R. Grau-Crespo, J. Chem. Phys., **137**, 154706 (2012).

List of Publications

Scientific Journal as first author

[1] “Growth of vanadium dioxide thin films on hexagonal boron nitride flakes as transferrable substrates”

Shingo Genchi, Mahito Yamamoto, Koji Shigematsu, Shodai Aritomi, Ryo Nouchi, Teruo Kanki, Kenji Watanabe, Takashi Taniguchi, Yasukazu Murakami, and Hidekazu Tanaka

Sci. Rep., **9**, 2857 (2019).

[2] “Prominent Verway Transition of Fe_3O_4 Thin Films Grown on Transferable Hexagonal Boron Nitride”

Shingo Genchi, Ai I. Osaka, Azusa N. Hattori, Kenji Watanabe, Takashi Taniguchi, and Hidekazu Tanaka

ACS Appl. Electron. Mater., **3**, 5031 (2021).

[3] “Step-like resistance changes in VO_2 thin films grown on hexagonal boron nitride with *in situ* optically observable metallic domains”

Shingo Genchi, Mahito Yamamoto, Takuya Iwasaki, Shu Nakaharai, Kenji Watanabe, Takashi Taniguchi, Yutaka Wakayama, and Hidekazu Tanaka

Appl. Phys. Lett., **120**, 053104 (2022).

[4] “Step electrical switching in VO_2 on hexagonal boron nitride using confined individual metallic domains”

Shingo Genchi, Shu Nakaharai, Takuya Iwasaki, Kenji Watanabe, Takashi Taniguchi, Yutaka Wakayama, Azusa N. Hattori, and Hidekazu Tanaka

Jpn. J. Appl. Phys., **62**, SG1008 (2023).

Scientific Journal as co-author

[1] “Broad range thickness identification of hexagonal boron nitride by colors”

Yuto Anzai, Mahito Yamamoto, **Shingo Genchi**, Kenji Watanabe, Takashi Taniguchi, Shuhei Ichikawa, Yasufumi Fujiwara, and Hidekazu Tanaka

Appl. Phys. Express, **12**, 055007 (2019).

[2] “Crystal orientation dependence of metal–insulator transition for VO_2 microwires fabricated on TiO_2(110) substrates with step and terrace structures”

Kyungmin Kim, **Shingo Genchi**, Shiro Yamazaki, Hidekazu Tanaka, and Masayuki Abe

Appl. Phys. Express, **15**, 045503 (2022).

[3] “Noncontact evaluation of the interface potential in VO_2/Si heterojunctions across metal-insulator phase transition”

Dongxun Yang, Fumikazu Murakami, **Shingo Genchi**, Hidekazu Tanaka, and Masayoshi Tonouchi.

Appl. Phys. Lett., **122**, 041601 (2023).

Review Article

“六方晶窒化ホウ素を用いた自由自在な機能性酸化物薄膜成長と素子応用展開への可能性”

玄地　真悟、田中　秀和

生産技術振興協会　季刊誌『生産と技術』　第 74 巻　第 3 号　p59–62　(2022)

Press Release

[1] “阪大　様々な材料に貼り付け可能な層状物質上で機能性酸化物の成長に成功”

日本経済新聞電子版　2018 年 12 月 19 日

[2] “二酸化バナジウム薄膜　あらゆる基板上に搭載　阪大が手法開発”

日刊工業新聞　2018 年 12 月 25 日

[3]“どこにでも貼り付けられる機能性酸化物薄膜 –万能成長基板を用いた新たな薄膜成長と素子応用展開–”

Research at Osaka University (ResOU)　2021 年 12 月 7 日

[4] “阪大　六方晶窒化ホウ素上でマグネタイト薄膜作製　他材料に貼り付け実証”

日刊工業新聞　2021 年 12 月 9 日

[5] “Stable and moveable; is hexagonal boron nitride the universal foundation?”

EurekAlert!　2021 年 12 月 2 日

International Conference

[1] “Growth and characterization of VO_2 on hexagonal boron nitride”

Shingo Genchi , Mahito Yamamoto, Teruo Kanki, Kenji Watanabe, Takashi Taniguchi and Hidekazu Tanaka

21st SANKEN International Symposium 2018, Osaka University, Ibaraki, Japan (January 16, 2018).

[2] “Growth and characterization of VO_2 on hexagonal boron nitride”

Shingo Genchi, Koji Shigematsu, Shodai Aritomi, Mahito Yamamoto, Teruo Kanki, Kenji Watanabe, Takashi Taniguchi, Yasukazu Murakami and Hidekazu Tanaka

The International Symposium for Materials Scientists “Inspiration for Innovation by Interaction” (ISMS III), Osaka University, Toyonaka, Japan (December 3, 2018).

[3] “Growth and characterization of VO_2 on hexagonal boron nitride”

Shingo Genchi, Koji Shigematsu, Shodai Aritomi, Mahito Yamamoto, Teruo Kanki, Kenji Watanabe, Takashi Taniguchi, Yasukazu Murakami and Hidekazu Tanaka

22nd SANKEN International Symposium 2019, Osaka University, Ibaraki, Japan (January 15, 2019).

[4] “Growth and characterization of VO_2 on hexagonal boron nitride”

Shingo Genchi, Koji Shigematsu, Shodai Aritomi, Mahito Yamamoto, Teruo Kanki, Kenji Watanabe, Takashi Taniguchi, Yasukazu Murakami and Hidekazu Tanaka

Handai-Kandai-GiessenDai Joint Seminar on Materials Science and Engineering, Osaka University, Toyonaka, Japan (March 26, 2019).

[5] “Growth and characterization of VO_2 thin films on hexagonal boron nitride”

Shingo Genchi, Koji Shigematsu, Shodai Aritomi, Mahito Yamamoto, Teruo Kanki, Kenji Watanabe, Takashi Taniguchi, Yasukazu Murakami and Hidekazu Tanaka

iWOE26 international Workshop on Oxide Electronics, Kyoto University, Uji, Japan (October 2, 2019).

[6] “Growth and characterization of VO_2 thin films on hexagonal boron nitride”

Shingo Genchi, Koji Shigematsu, Shodai Aritomi, Mahito Yamamoto, Teruo Kanki, Kenji Watanabe, Takashi Taniguchi, Yasukazu Murakami and Hidekazu Tanaka

2nd Workshop on MICROACTUATORS, Osaka University, Ibaraki, Japan (October 4, 2019).

[7] “Scaling effects in the resistance-temperature characteristic of VO_2 on hBN”

Shingo Genchi, Mahito Yamamoto, Teruo Kanki, Kenji Watanabe, Takashi Taniguchi and Hidekazu Tanaka

The International Symposium for Nano Science (ISNS), Osaka University, Toyonaka, Japan (November 28, 2019).

[8] “Scaling effects in the resistance-temperature characteristic of VO_2 on hBN”

Shingo Genchi, Mahito Yamamoto, Teruo Kanki, Kenji Watanabe, Takashi Taniguchi and Hidekazu Tanaka

Materials Research Society, Hynes Convention Center, Boston, USA (December 5, 2019).

[9] “Characterization of the phase transition property of VO_2 grown on hBN”

Shingo Genchi, Mahito Yamamoto, Kenji Watanabe, Takashi Taniguchi, Hidekazu Tanaka

Phase Change Oriented Science (PCOS) 2020, online (November 19, 2020).

[10] “Characterization of Verway transition property in Fe_3O_4 thin films growth on transferable hBN substrate”

Shingo Genchi, Ai I. Osaka, Azusa N. Hattori, Kenji Watanabe, Takashi Taniguchi, Hidekazu Tanaka

International Workshop on Oxide Electronics (iWOE27), online (October 14th, 2021).

[11] “Growth of Fe_3O_4 thin films on hBN showing prominent Verway transition”

Shingo Genchi, Ai I. Osaka, Azusa N. Hattori, Kenji Watanabe, Takashi Taniguchi, Hidekazu Tanaka

Materials Research Meeting 2021, Pacifico Yokohama, Yokohama, Japan (December 16th, 2021).

[12] “Step-like electric current switching in VO_2/hBN device using individual metallic domains”

Shingo Genchi, Shu Nakaharai, Kenji Watanabe, Takashi Taniguchi, Yutaka Wakayama, and Hidekazu Tanaka

35th International Microprocesses and Nanotechnology Conference (MNC 2022), JR Hotel Clement Tokushima, Tokushima, Japan (November 10th, 2022).

Domestic Conference

[1] “六方晶窒化ホウ素上での VO_2 の薄膜成長と評価”

玄地　真悟、山本　真人、神吉　輝夫、渡邊　賢司、谷口　尚、田中　秀和

第 65 回応用物理学会春季学術講演会、早稲田大学、東京、2018 年 3 月 20 日

[2] “六方晶窒化ホウ素上における VO_2 の薄膜成長と評価（Ⅱ）”

玄地　真悟、重松　晃次、有冨　翔大、山本　真人、神吉　輝夫、渡邊　賢司、谷口　尚、田中　秀和

第 79 回応用物理学会秋季学術講演会、名古屋国際会議場、愛知、2018 年 9 月 18 日

[3] “六方晶窒化ホウ素上 VO_2 の金属絶縁体相転移に伴う抵抗変化の素子サイズ依存性”

玄地　真悟、山本　真人、神吉　輝夫、渡邊　賢司、谷口　尚、田中　秀和

第 66 回応用物理学会春季学術講演会、東京工業大学、東京、2019 年 3 月 10 日

[4] “六方晶窒化ホウ素上 VO_2 における抵抗跳躍の電極間距離依存性”

玄地　真悟、山本　真人、神吉　輝夫、渡邊　賢司、谷口　尚、田中　秀和

第 80 回応用物理学会秋季学術講演会、北海道大学、札幌、2019 年 9 月 18 日

[5] “六方晶窒化ホウ素上における Fe_3O_4 薄膜の成長と評価”

玄地　真悟、大坂　藍、服部　梓、渡邊　賢司、谷口　尚、田中　秀和

第 68 回応用物理学会春季学術講演会、オンライン、2021 年 3 月 16 日

[6] “転写可能 hBN 剥片上での Fe_3O_4 薄膜成長の実現”

玄地　真悟、大坂　藍、服部　梓、渡邊　賢司、谷口　尚、田中　秀和

日本金属学会 2021 年秋期第 169 回公演大会、オンライン、2021 年 9 月 15 日

[7] “CVD 成長大面積 hBN シートへの遷移金属酸化物薄膜結晶の成長”

玄地　真悟、深町　悟、大坂　藍、服部　梓、吾郷　浩樹、田中　秀和

第 69 回応用物理学会春季学術講演会、青山学院大学、相模原、2022 年 3 月 23 日

Award

[1] 生産技術振興協会 海外論文発表奨励賞（令和元年度・下期）

[2] Best Poster Presentation Award, The International Symposium for Nano Science (ISNS), Osaka, Japan (November 28, 2019)

Grant

[1] 財団法人　NEC C&C 財団　国際会議発表助成 (October, 2019)

[2] 日本学術振興会　科学研究費助成事業　特別研究員奨励費

研究課題名 : 遷移金属酸化物/2 次元層状物質ファンデルワールス構造・機能インテグレーション（Grant No. 20J21010）

期間：2020 年 4 月–2023 年 3 月

Acknowledgement

I wish to express the sincerest gratitude and appreciation to Professor Hidekazu Tanaka of SANKEN (The Institute of Scientific and Industrial Research), Osaka University. Without his continuous encouragement, kind support and active discussion, I would have never made progress in my research. He has made me what I am as a scientist through my master and doctoral courses.

I'd like to express my sincere gratitude to Associate Professor Azusa N. Hattori of SANKEN for her many supports, technique of presentation and writing papers and helpful discussion.

I'd like to express my gratitude to Assistant Professor Hao-bo Li of SANKEN for the kind support of my experiments, useful comments toward my research progress.

I appreciate Specially Appointed Assistant Professor Ai I. Osaka of SANKEN for warm support of my work and discussion and my press release.

I'd like to express my thanks to Associate Professor Mahito Yamamoto of Kansai University for his kind help in my master course.

I'd like to thank the supervisors of my doctoral thesis: Professor Masaaki Ashida and Professor Hajime Ishihara of Graduate School of Engineering Science, Osaka University for their useful comments and suggestions to my study.

I appreciate all the staffs of the Graduate School Leading Cadet Program in Institute for Transdisciplinary Graduate Degree Programs, Osaka University. I thank Professor Kenji Iijima and Mr. Yoichiro Yokotani for their support of my precious experiences in the Cadet Program. I appreciate Dr. Motoaki Bamba, Dr. Hidetomo Usui, and Dr. Harushige Nakao for mentoring my activity in the Cadet Program. I thank Ms. Yasuko Ueda, Ms. Miwa Shimizu, and Ms. Aki Okubo of the Cadet Program for their kind office procedure. Every time I faced difficulty in my study, I was encouraged by their warm

support.

I was supported by many co-researchers during my master and doctoral courses. I thank Professor Yasukazu Murakami, Dr. Koji Shigematsu, and Mr. Shodai Aritomi of Kyushu University for the STEM measurement. I thank Professor Hiroki Ago and Mr. Satoru Fukamachi of Kyushu University for the supply of high-quality CVD-hBN sheets. On the analysis of the crystallinity of the thin films on CVD-hBN sheets, I received a kind assistance by Associate Professor Ken Hattori of Nara Institute of Science and Technology.

I thank Dr. Takashi Taniguchi and Dr. Kenji Watanabe of National Institute for Materials Science (NIMS) for the synthesis of high-quality bulk single crystals of hBN. I thank the members of Quantum Device Engineering Group in International Center for Materials Nanoarchitectonics (MANA) of NIMS: Dr. Yutaka Wakayama (Deputy Director of MANA and Group Leader), Dr. Shu Nakaharai (Principal Researcher), Dr. Takuya Iwasaki (Independent Scientist), Dr. Yoshitaka Shingaya (Senior Researcher), and Ms. Remi Minoshima for their kind support during the domestic internship for three months in the Cadet Program. I'd also like to acknowledge the technical staffs, especially Dr. Eiichiro Watanabe in NIMS Nanofabrication Open Facility for the technical instruction. The domestic internship in Tsukuba was a priceless opportunity to conduct research in a different environment. I learned the most important motto as a researcher during the internship: "The fruits of your research are proportional to the number of your conversations with others."

I thank Professor Wen-Hao Chang of National Yang Ming Chiao Tung University, Taiwan for supervising the online overseas cooperative research as an international internship in the Cadet Program.

I appreciate Professor Yasufumi Fujiwara, Associate Professor Jun Tatebayashi, and Assistant Professor Shuhei Ichikawa of Graduate school of Engineering, Osaka University to support my research during “laboratory rotation” in the Cadet Program in my master course. It was a precious opportunity for me to characterize the optical property of rare-earth ion doped gallium nitride. The laboratory rotation was an excellent experience for me to get interested in the integration of physics and chemistry.

I’d like to express my gratitude to Professor Masayuki Abe and Mr. Kyungmin Kim of Graduate School of Engineering Science, Osaka University, Professor Masayoshi Tonouchi, Mr. Dongxun Yang of Institute of Laser Engineering, Osaka University, and Assistant Professor Shiro Yamazaki of Department of Physics, Tokyo Institute of Technology for collaborative research and active discussion in “laboratory rotation” in the Cadet Program. When they conducted their external study in Tanaka laboratory for three months, I had an opportunity to support their whole study, including operation of the experimental facilities, analysis of the data, preparation of oral presentation and writing papers and so forth. I was able to become confident as a researcher and an instructor through this precious experience.

I’d like to tell my gratitude to all the technical staffs, especially Dr. Akira Kitajima, Ms. Yukiko Watsuji of Advanced Research Infrastructure for Materials and Nanotechnology in Japan (ARIM) in Osaka University for giving me a useful experimental support in my daily research.

I’m really thankful to all the members in Tanaka Laboratory: Mr. Boyuan Yu, Mr. Sharad Sunil Mane, Mr. Rui Li, Mr. Yuki Taniguchi, Mr. Ryota Koizumi, Mr. Keito Umesaki, Mr. Kohei Shimoyama, Mr. Yuki Tomita, Mr. Umar Sidik, Dr. Hui Ren, Mr. Fumiya Endo, Mr. Takashi Yamanaka, Mr. Jun Takigawa, Mr. Shin Nonaka, Mr. Toshiya

Suzuki, Mr. Akira Namba, Mr. Akira Hirao, Mr. Taisei Kasamatsu, Mr. Koki Tanohata, Mr. Yuto Anzai, Mr. Daiki Kawamoto, Mr. Yoshihide Tsuji, Mr. Keita Muraoka, Mr. Yoshiyuki Higuchi, Mr. Keiichiro Hayashi, Mr. Kotaro Sakai, Mr. Toshiki Tanimura, Dr. Alexis Borowiak, Dr. Rupali Rakshit, and Dr. Shohei Takemoto for their assistance, comfort and encouragement in my life in Tanaka laboratory. I would like to thank Ms. Tomoko Okumoto and Ms. Saeko Takahata for their attentive assistance in my office procedure. The experimental work was kindly assisted by excellent technical staffs: Dr. Shoichi Sakakihara, Ms. Michiko Sakuma, Ms. Saeko Tonda, Mr. Takeshi Ishibashi, and Ms. Shoko Wakisaka.

I'd like to express the deepest appreciation to Dr. Osamu Nakagawara and Mr. Masaki Tsutsumi of Murata Manufacturing Co., Ltd. for their encouragement.

I also express my gratitude to Invited Professor Shigemasa Suga and Invited Professor Koun Shirai for their continuous warm encouragement in the last year of my doctoral course. Now I can enjoy myself in table tennis more than ever.

Finally, I would like to thank my family for encouraging my dream of becoming a scientist from my childhood and supporting my life. This dissertation is dedicated to my family: Manabu Genchi, Noriko Genchi, Mako Genchi, my Pekingese, and my beloved wife Yukari N. Genchi.

March 2023

Shingo Genchi